HRSC: High Resolution Stereo Camera

G. Neukum[1], R. Jaumann[2,1], A.T. Basilevsky[3], A. Dumke[1], S. van Gasselt[1], B. Giese[2], E. Hauber[2], J.W. Head, III[4], C. Heipke[5], N. Hoekzema[6], H. Hoffmann[2], R. Greeley[7], K. Gwinner[2], R. Kirk[8], W. Markiewicz[6], T.B. McCord[9], G. Michael[1], J.-P. Muller[10], J. B. Murray[11], J. Oberst[12,2], P. Pinet[13], R. Pischel[14], T. Roatsch[2], F. Scholten[2], K. Willner[2], the HRSC Co-Investigator Team[15] and HRSC Associates

[1] *Freie Universität Berlin (FUB), Institute of Geosciences, Planetology and Remote Sensing, Berlin, Germany*
[2] *German Aerospace Center (DLR) Berlin, Institute of Planetary Research, Berlin, Germany*
[3] *Vernadsky Institute of Geochemistry and Analytical Chemistry, Russian Academy of Science, Moscow, Russia*
[4] *Brown University, Department of Geological Sciences, Providence, RI, USA*
[5] *Universität Hannover, Institut für Photogrammetrie und GeoInformation (IPI), Hannover, Germany*
[6] *Max Planck Institute for Solar System Research (MPS), Katlenburg-Lindau, Germany*
[7] *Arizona State University (ASU), School of Earth and Space Exploration (SESE), Tempe, AZ, USA*
[8] *US Geological Survey (USGS), Astrogeology Program, Flagstaff, AZ, USA*
[9] *Bear Fight Center, Space Science Institute, Winthrop, WA, USA*
[10] *UCL Mullard Space Science Laboratory, MSSL, Space and Climate Physics, Dorking, Surrey, UK*
[11] *The Open University, Department of Earth Sciences, Milton Keynes, UK*
[12] *Technical University of Berlin, Geodesy and Geoinformation Science, Planetary Geodesy, Berlin, Germany*
[13] *Laboratoire dynamique terrestre et planetaire de l'Observatoire de Midi-Pyrenees, Toulouse, France*
[14] *ESA Moscow, Moscow, Russia*
[15] *See Table 7*

The High Resolution Stereo Camera (HRSC) on Mars Express has delivered a wealth of image data, amounting to over 2.5 TB from the start of the mapping phase in January 2004 to September 2008. In that time, more than a third of Mars was covered at a resolution of 10–20 m/pixel in stereo and colour. After five years in orbit, HRSC is still in excellent shape, and it could continue to operate for many more years. HRSC has proven its ability to close the gap between the low-resolution Viking image data and the high-resolution Mars Orbiter Camera images, leading to a global picture of the geological evolution of Mars that is now much clearer than ever before. Derived highest-resolution terrain model data have closed major gaps and provided an unprecedented insight into the shape of the surface, which is paramount not only for surface analysis and geological interpretation, but also for combination with and analysis of data from other instruments, as well as in planning for future missions.

This chapter presents the scientific output from data analysis and high-level data processing, complemented by a summary of how the experiment is conducted by the HRSC team members working in geoscience, atmospheric science, photogrammetry and spectrophotometry. Many of these contributions have been or will be published in peer-reviewed journals and special issues. They form a cross-section of the scientific output, either by summarising the new geoscientific picture of Mars provided by HRSC or by detailing some of the topics of data analysis concerning photogrammetry, cartography and spectral data analysis.

1. Introduction

The HRSC experiment on Mars Express has delivered a wealth of data since the start of its orbital mapping phase in January 2004. At the time of writing, the goal of global coverage had been partially achieved, with 35% coverage at a resolution of 10–20 m/pixel in stereo and colour, and it is expected that ~60% coverage will have been achieved by the end of the present mission extension period (May 2009). Unfortunately, we will then still be some way from the primary goal of the HRSC to achieve 100% coverage at 10–20 m/pixel, but this is due to the much more limited operational performance of the spacecraft in terms of data acquisition and downlink capabilities than was envisaged in the original plans before launch. Nevertheless, the original coverage goal could be achieved with an appropriate further extension of the mission and the full operation of the HRSC.

Technically, there does not appear to be a problem with the HRSC; the instrument is in very good shape, and it could continue to operate for many more years. The scientific output from the analysis of the imagery over 3.5 years of operation is remarkable. The HRSC team has been slightly modified to include new scientists working in areas where it was realised that sufficient experience in data analysis was lacking in the original team, and it consists of 44 individual co-investigators from 26 institutions and 10 countries (Fig. 1). By 2009 several co-investigators will join or will have left the team (see Table 7). The team's outputs so far include 60 refereed papers published in professional journals, as well as 120 extended abstracts (citable short papers) and 350 conference abstracts and related talks or posters. Also, seven young scientists associated with the team members have completed doctoral and diploma/master theses. Among the publications are landmark papers in prestigious journals such as *Nature* (Neukum et al., 2004a; Hauber et al., 2005a; Head et al., 2005a; Murray et al., 2005).

This chapter represents the first attempt to provide a comprehensive summary of the most important results of the HRSC CoI team as a 'team effort' covering all scientific areas relevant in the data analysis directly related and close in time to the data flow from the mission. These include results from the geosciences, atmospheric, photogrammetry and cartography, and spectrophotometry working groups. It should be noted that the HRSC dataset has to undergo a complicated data processing effort by a number of groups of the team, in particular the DLR group in Berlin and the other groups that handle the production of Digital Terrain Models (DTMs). At present, a new effort is under way to produce high-resolution archive-quality DTMs, financed by the DLR agency and concentrated at DLR Berlin and FU Berlin. This will significantly enhance the usability of the stereo data, and will probably have a very positive effect in the area of data analysis offline.

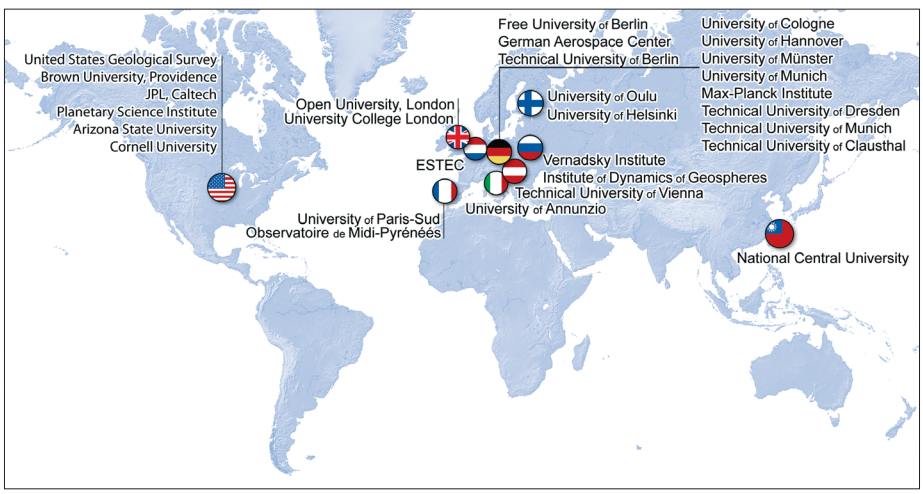

Fig. 1. The HRSC team.

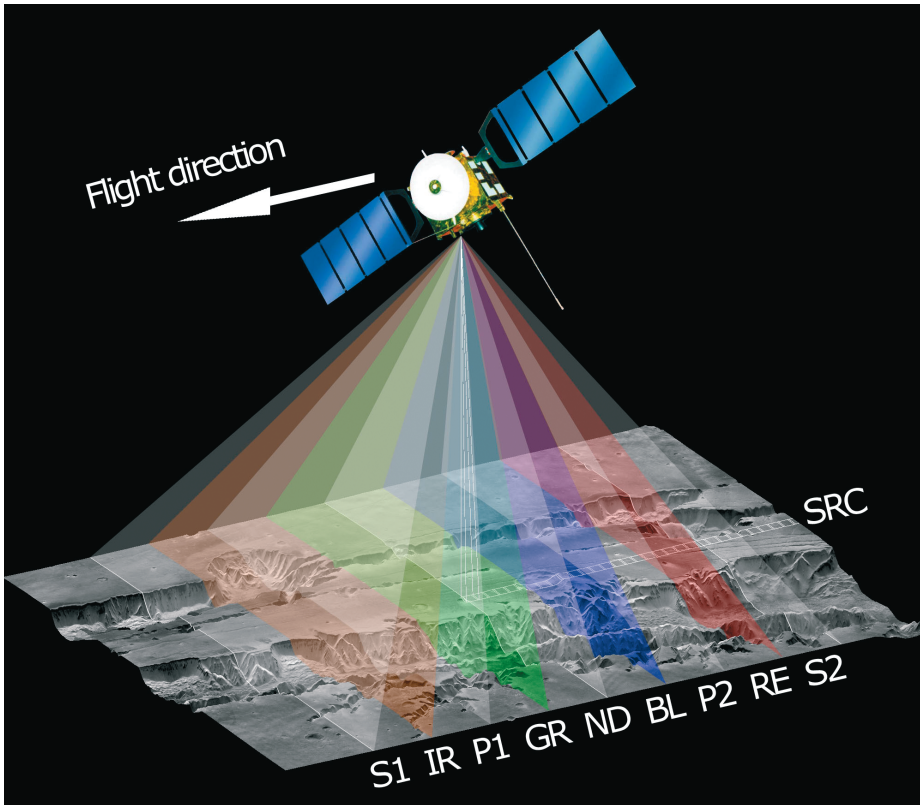

Fig. 2. Operating principle and viewing geometry of the individual CCD sensors: ND, nadir channel; S1, S2, stereo 1 and stereo 2 (±18.9°); P1 and P2, photometry 1 and photometry 2 (±12.8°); IR, near-infrared channel (+15.9°); GR, green channel (+3.3°); BL, blue channel (–3.3°); RE, red channel (–15.9°). All nine lines sensors have a cross track field of view of ±6°. SRC, Super-Resolution Channel (panchromatic).

For readers who are familiar with the history of the exploration of Mars, the previously (before HRSC) available large-area coverage imagery and the previous interpretation of the geological evolution and history of Mars, this chapter will demonstrate that the HRSC experiment has opened up new domains of in-depth scientific interpretation, and is already is beginning to change our view of Mars considerably. To give just a few examples: the idea that Mars was wet and warm, with a thick atmosphere, early on, possibly lasting long into mid-martian history, is now questioned. Whether there was a global ocean for a long period of time early on seems rather unlikely on the basis of the analysis of the HRSC data (and OMEGA data). It is now becoming clear that the evolution of the martian surface was probably not steady over time but episodic. All of these questions will be addressed further in the course of the mission with additional HRSC data, and there may be many surprises in the future.

2. HRSC Experiment and Achievements

The HRSC (Fig. 2) represents a multi-sensor push-broom instrument comprising nine CCD line sensors mounted in parallel for simultaneous high-resolution stereo, multicolour and multi-phase imaging by delivering nine superimposed image swaths (Jaumann et al., 2007). The HRSC is designed to perform stereo imaging with triple to quintuple panchromatic along-track stereo, including a nadir-directed, forward and aft-looking (±18.9°), and two inner (±12.8°) stereo line sensors. Their spectral range covers 675 ± 90 nm (width at half-maximum). Multispectral imaging is realised by four line sensors in the blue, green, red and near-infrared colour ranges (440 ± 45, 530 ± 45, 750 ± 20 and 970 ± 45 nm). All nine line sensors have a cross-track field of view of ±6°. They are mounted behind one single transmission optics with a focal length of 175 mm and an aperture of $f = 5.6$. Each of the nine Thomson THX 7808B linear CCD arrays has 5184 active pixels 7 × 7 µm in size. An additional Super-Resolution Channel (SRC) provides frame images embedded in the basic HRSC swath at five times higher

Table 1. Baseline performance of the High Resolution Stereo Camera (HRSC) with the Super-Resolution Channel (SRC).

Parameter	*HRSC*	*SRC*	*Comments*
	Mechanical and electrical parameters		
Camera unit envelope	510 × 289 × 273 mm		length × width × height
Digital unit envelope	232 × 282 × 212 mm		DU used for HRSC and SRC
Mass	20.4 kg		
Power consumption	43.4 W during imaging	5.3 W during imaging	Joint ops: 48.7 W
	Electro-optical performance		
Detector type	THX 7808B	Kodak KAI 1001	
Sensor pixel size	7 × 7 µm	9 × 9 µm	
Pixel size on ground	10 × 10 m	2.3 × 2.3 m	at 250 km altitude
Field of view per pixel	8.25 arcsec	2 arcsec	
Active pixels per sensor	9 sensors of 5184	1008 × 1018	
Image size on ground	52.2 km swath × [time]	2.35 × 2.35 km	at 250 km altitude
Radiometric resolution	8 bit before compress.	14 bit or 8 bit, selectable	
Sensor full well capacity	420,000 e^-	48,000 e^-	
Signal chain noise	<42 e^- (rms)	< 52 e^- (rms) readout noise	
Gain attenuation range	3.5–2528	–	corresp. to 10.5–62 dB (SRC gain 5.34e/DN)
Spectral filters	5 panchromatic, 4 colour	panchromatic	
Nadir, 2 stereo, 2 photo.	675 ± 90 nm	–	nadir 0°, stereo ±18.9°, photometry ±12.8°
Blue, green, red, near-infrared	440 ± 40 nm, 540 ± 45 nm 750 ± 25 nm, 955 ± 40 nm	–	blue –3.3°, green +3.3°, red –15.9°, near infrared +15.9°
Centre pixel MTF*	0.40 at 50 lp/mm	–0.28 at 56 lp/mm	
20° off nadir MTF	0.33 at 50 lp/mm		
SNR for panchromatic Lines	>>100 (no macro pixel)	>70	30° solar elevation, dark region
SNR for colour lines	>80, blue >40	–	for 2 × 2 macro pixel
	Digital features		
Online compression	yes		DCT: table controlled JPEG
Compression rate	2–20; bypass possible		
Max. Output data rate	25 Mbit/s after compression (only at pericentre)		decreases at higher altitudes
	Operations		
Pixel exposure time	2.24–54.5 ms	0.5 ms to 50 sec	
Pixel summation formats	1 × 1, 2 × 2, 4 × 4, 8 × 8	–	
Compression rates	nominal: 6 ... 10		
Typical image size	53 × 330 km	2.4 × 2.4 km	at 250 km altitude
Typical data volume per image	230 Mbit	8 or 14 Mbit	
Duty cycle	every orbit; several times/orbit		depends on memory budget
Internal data buffer	No	4 images at 14 bit resolution	
Typical operation duration	3–40 min		command dependent
Expected coverage	≥50% at about 15 m/pixel	>1% at about 2–3 m/pixel	
Moving parts	none	none	
Operational lifetime	>4 years		

* MTF modulation transfer function

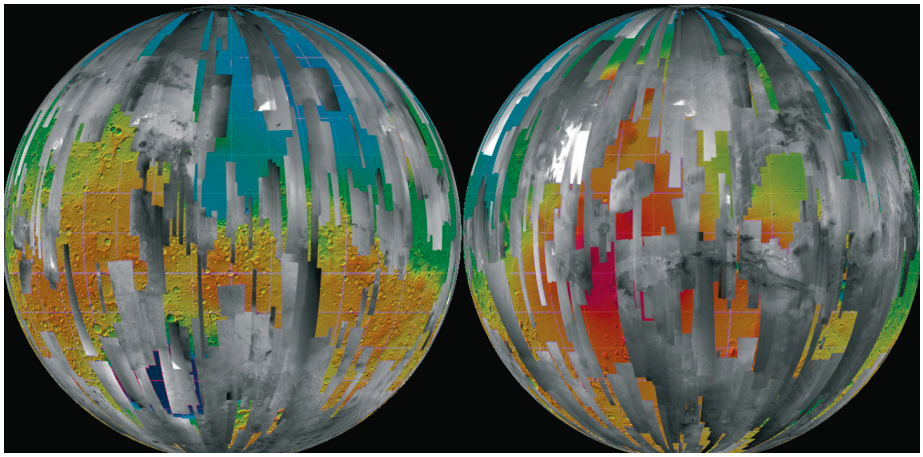

Fig. 3. Mapping coverage of HRSC (in grey) up to orbit 3358, draped over a colour-coded MOLA DTM.

resolution. The SRC comprises a 1024 × 1024 CCD array and lightweight mirror optics with its optical axis parallel to that of the HRSC camera head. The total mass of the HRSC, including the SRC, is 20.4 kg. During imaging the total power consumption is 48.7 W. The focal plane temperature is kept within the range +7 to +17°C by camera internal heaters. The characteristic parameters of the instrument are given in Table 1.

HRSC maps the martian surface in stereo and colour with a resolution better than 20 m (Fig. 3). These data have been the basis for a series of scientific investigations to determine the age of Mars and to provide quantitative estimates of surface processes. In addition, the instrument provides the topographic reference for larger areas of Mars such as Tharsis, Valles Marineris, Xanthe Terra, Chryse Planitia and the polar regions. The generation of high-resolution local grids of topography, slopes and surface roughness will also assist in identifying and assessing potential future landing sites and roving areas.

The observation conditions for HRSC are determined mainly by the Mars Express orbit:

— The orbit is highly elliptical, nearly polar orbit with an average pericentre altitude of 287 km and an orbital period of 6.72 h. The HRSC image acquisition with nadir pointing of the Mars Express spacecraft is driven by the target position with respect to this elliptical orbit. HRSC can achieve its best resolution of better than 20 m per line sensor pixel within a window of about 15 min around pericentre when the spacecraft is below 500 km altitude. The average imaging duration is 6 min due to data volume and illumination constraints. Not all pericentre windows in a certain period are available for HRSC observations because, on average, one out of four pericentres cannot be used for scientific observation while the fixed-mounted spacecraft antenna is pointed towards Earth. The sub-pericentre points for such a period are grouped into 11 clusters with a 3:11 resonant pattern: for each construction site a new adjacent track is added after 11 orbits or three days. This Mars Express orbit feature was particularly designed for HRSC in order to enable the acquisition of image mosaics with little time variations between adjacent image strips.

— The illumination conditions for the pericentre window vary over the mission. During the nominal mission three dayside periods of 4–5 months each were separated by two nightside periods of four months each. The latitude of the sub-spacecraft point at pericentre covered all latitudes twice during the nominal mission and will cover it twice during the extended mission. Thus targets at the same latitude can be observed during different seasons. The orbit position of the spacecraft is measured with an average accuracy of better than 200 m. The average difference between the position predicted one week in advance and the real position is 2 km, where the main component of the error is along the orbit trajectory, and corresponds to about 0.5–1 s. The accuracy of the spacecraft attitude information is 0.01°.

Table 2. HRSC mapping coverage of the martian surface until orbit 3358.

Spatial resolution (m/pixel)	*Mapping coverage (% of martian surface)*	*Mapped area (million km²)*
≤20	31.0%	44.9
≤30	44.6%	64.7
≤40	53.9%	78.1
≤50	59.9%	86.9
≤60	63.9%	92.7
≤100	68.0%	98.5

The numbers do not take into account the image quality, which varies due to the variable atmospheric seeing conditions.

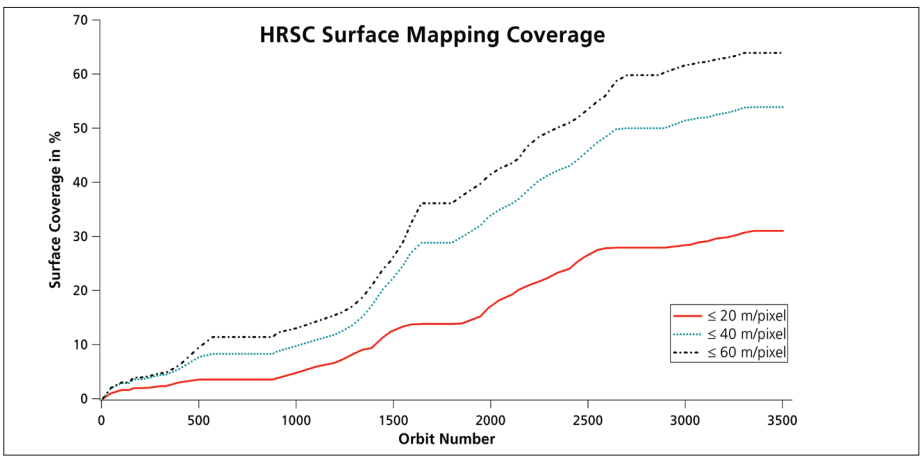

Fig. 4. HRSC surface mapping coverage up to orbit 3358 at spatial resolutions of ≤20, ≤40 and ≤60 m/pixel.

2.1 Mapping and Statistics

After orbit insertion on 25 December 2003, HRSC made its first image in orbit 8, on 9 January 2004. Since then, HRSC acquired data during 1198 orbits and performed 1489 image observations until the Mars Express science operations had to stop for more than two months after orbit 3358, in mid-August 2006, due to the long duration of solar eclipses and the subsequent solar conjunction. HRSC collected a total of 817 GB of uncompressed data, which contributed to meeting the prime objective of HRSC to image and map the martian surface (Fig. 3).

With a total of 1258 surface observations, HRSC has so far covered about 64% of the martian surface at spatial resolutions ≤60 m/pixel, and 31% at ≤20 m/pixel (Table 2). These numbers refer to the mapping coverage, taking into account any overlap between adjacent image strips. A standard HRSC image comprises imaging with all nine channels, thus providing high-resolution, stereo and colour imagery at the same time. Along one orbit, the image length is restricted only by the available data storage and downlink capacities. Thus, HRSC images are several hundred to several thousand kilometres long. To obtain contiguous image coverage also in a cross-track direction at similar spatial resolution and observation conditions (i.e. atmospheric seeing and illumination), HRSC is aiming to operate in consecutive orbits for mosaicking image strips with an overlap of about 10%. The Mars Express orbit was optimised for this purpose in its longitudinal periapsis walk, which reaches the same area on Mars after 11 orbit revolutions and three days with a slight westward shift. Owing to technical constraints, however, such as Earth contact or spacecraft resources, as well as the

necessary sharing of resources among the different experiments on Mars Express with their specific needs for pointing at periapsis, only three to five orbits out of nine can be used for short-term mosaicking within a planning cycle of 100 orbits.

The development of the HRSC mapping coverage over the mission until August 2006 reflects the effect of the Mars Express data transfer capacity, which is determined by the distance between Mars and Earth and the availability of ground stations (Fig. 4). Major breaks in surface mapping are related to night-time periods, solar conjunction, and long solar eclipses. The periapsis went three times into the dark. At the beginning and end of such a period, however, HRSC still encounters acceptable observation conditions at higher altitudes, and the mapping coverage at lower spatial resolutions increases considerably compared with the high-resolution coverage of ≤20 m/pixel.

The secondary objectives of HRSC comprise observations for atmospheric sciences and of the martian moons. For studying atmospheric phenomena, HRSC has performed 70 limb soundings and 72 observations of the terminator and from high altitudes. Phobos has been imaged successfully 44 times and Deimos 18 times. HRSC has also succeeded in capturing the shadow of Phobos on the martian surface seven times. Finally, 28 data takes were conducted for in-flight calibration and testing, and during spot pointing.

2.2 HRSC in the Context of other Camera Experiments

Imaging is a major source of information for increasing our understanding of the evolution of the martian geology and climate. Consequently, since the beginning of exploration of the Red Planet, all Mars missions have been equipped with a camera instrument and have sent back a wealth of information. The basis for the ongoing Mars exploration effort was laid in the late 1970s by the Viking missions, which achieved a near-global coverage of the martian surface (95%) at 200 m/pixel, 28% coverage at ≤100 m/pixel, and 0.3% at ≤20 m/pixel (e.g. Neukum & Hoffmann, 2000). At present there are four missions operating in orbit around Mars, each of which carries a camera instrument and delivers imaging data back to Earth. The value of HRSC can only be assessed by putting it in context with the other imaging devices.

The Mars Observer Camera (MOC) on the Mars Global Surveyor (MGS) comprises two instruments. The wide-angle camera has covered the entire martian surface at 240 m/pixel and in two colours. It also monitors the martian weather at resolutions of a few kilometres. The narrow-angle camera has a spatial resolution of up to 1.4 m/pixel (Malin & Edgett, 2001) and has so far covered about 3% of the martian surface. By applying a slew manoeuvre of the spacecraft during imaging, the along-track pixel resolution could be improved to <1 m for selected observations. The small image size of a few kilometres causes problems in analysing the data in their broader geological context. Stereo observations are obtained for specific targets by pointing the spacecraft towards the same area in different orbits.

The Thermal Emission Imaging System (THEMIS) instrument on Mars Odyssey (MO) provides a spatial resolution of up to 18 m/pixel in the VIS (Christensen et al., 2004) and has covered 20% of the martian surface at ≤20 m/pixel and 35% at ≤50 m/pixel. The pointing capability of the spacecraft is limited and does not allow stereo observations. The camera has five colours but only very limited colour coverage. The typical image size is about 20 × 100 km.

The Mars Reconnaissance Orbiter (MRO) has just started its science operations and carries three camera experiments. Daily weather monitoring in the kilometre range is the task of the Mars Color Imager (MARCI), which has five colour filters in the VIS and two filters in the UV (*www.msss.com/mro/marci/index.html*). The High Resolution Imaging Science Experiment (HiRISE) has a maximum spatial resolution of 0.3 m/pixel and is equipped with three colours (McEwen et al., 2007). During normal operations, the highest resolution will be achieved for the central part of the image swath, while a 4 × 4 pixel binning on the sides yields a spatial resolution of 1.2 m/pixel. It is planned to cover ~1% of the martian surface at ≤1.2 m/pixel, ~0.1% at 0.3 m/pixel, and ~0.1% in all three colours during the nominal mission. Each HiRISE image will be accompanied by an image of the Context Imager (CTX),

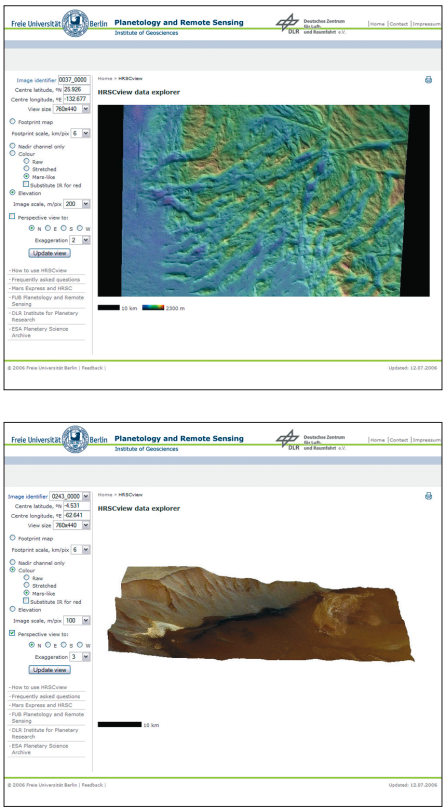

Fig. 5. Screenshots from the HRSCview web interface showing (top) a nadir elevation composite from orbit 37, Lycus Sulci region, and (bottom) a nadir colour composite perspective view of the layered deposits in Juventae Chasma.

which obtains black-and-white images at a spatial resolution of 6 m/pixel (*www.msss.com/mro/ctx/index.html*). CTX is aiming to cover 15% of the martian surface. Stereo observations are envisaged by HiRISE for ~0.1% of the surface.

In comparison with the other camera instruments, the HRSC experiment has a number of unique features, including:

— Its unprecedented capability to provide wide-area contiguous coverage in colour at relatively high spatial resolution fills the gap between Viking, Mars Global Surveyor MOC and HiRISE on MRO, as well as relatively high-resolution global coverage.
— Its capability to produce stereo images in colour for geological interpretation in 3D, and for the derivation of high-resolution digital terrain models (DTMs). HRSC is the only dedicated stereo camera recording stereo information routinely for each observation nearly simultaneously and under the same observation conditions (atmospheric seeing, illumination).
— Its multiple-line concept with different viewing angles yields intrinsic geometric stability compared with the single-line imaging concept of the other cameras.
— The peculiar orbit of Mars Express and its pointing capabilities enable imaging at all times of day, whereas MGS, MO and MRO have Sun-synchronous, circular orbits, allowing imaging at fixed local times in the afternoon (15:00 and 14:00 h, respectively). HRSC is also the only instrument that can observe Phobos at high resolution due to the elliptical orbit.

In conclusion, the different camera experiments operating in orbit around Mars are highly complementary.

2.3 Data Distribution and Availability

2.3.1 Data distribution via the ESA PSA and NASA PDS

The data acquired by the HRSC instrument have been released every six months to the ESA Planetary Science Archive. All the science data from the first 4479 orbits are available for public access.

Initially, the data were provided as radiometrically calibrated products (Level-2). Since 4 April 2006, they have also been made available as Level-3 (map-projected, ortho-rectified using the MOLA DTM). The data are validated, mainly by visual inspection, by the Co-I team, led by G. Neukum (FUB), H. Hoffmann (DLR), R. Greeley (ASU) and G. Ori (IRSPS). To date, a total of 1.4 Terabytes of radiometrically calibrated data have been released. The map-projected data volume is approximately the same. All products are formatted in accordance with PDS standards. Software for both the visualisation and the generation of map-projected data are provided together with the data release (xvd and hrortho/frameortho).

Detailed specifications of the archived HRSC data products are given in the instrument's Experiment to Archive Interface Control Document (EAICD) (Roatsch, 2005), which is also available in the archive.

2.3.2 HRSCview: a web-based data exploration system

To increase the usability and accessibility of the very large HRSC dataset to the science community we have implemented a system for exploring the data online, with a capability for providing linked access to archived full science data products (e.g. Michael, 2006). The system can be accessed using a normal browser from a joint website of the Free University of Berlin and the German Aerospace Centre (DLR).

HRSCview (Fig. 5) permits exploration within the images by carrying out on-the-fly data-subsetting, sub-sampling, stretching and compositing and, in the case of perspective views, projection. This means that regions of interest can be explored at full resolution without the need to download the full data product sets. It is possible to view colour and elevation composites with nadir images (via HSV transformation) and select different colour stretches or infrared channel substitution. It offers perspective views with a choice of viewpoint and exaggeration. The data are explored using Mars

surface coordinates, making it a simple matter to move between multiple images of the same location, and also to move from a global image footprint map directly into an HRSC image at a position of interest. The map scale of the view can be selected using the distance and elevation scale bars provided. Images can be accessed by orbit/image number as well as via the footprint map. In either case, a link is provided to a data product page, where header items describing the full map-projected science data product are displayed, and a link to the archived data products can be provided. HRSCview is currently being tested by the Co-I team, and will shortly be opened for public access. At present, the elevation composites are derived from the HRSC preliminary 200 m DTMs generated at DLR, which will not be available as separately downloadable data products. These DTMs will be progressively superseded by higher-resolution archival DTMs, also from DLR, which will be made available for download.

The service is distinct from that provided by the ESA PSA in that it provides a means to explore inside the individual (but very large) images, and to carry out a preliminary on-the-fly processing of the data. A more powerful version of the software, including tools for quantitative DTM analysis and intended for working with locally hosted HRSC data products, will be made available for work with the archived DTMs.

3. Scientific Achievements

3.1 Photogrammetry

3.1.1 Stereophotogrammetric Processing of HRSC data

The multi-stereo and multi-spectral capabilities of HRSC enable high-resolution photogrammetric stereo analysis as well as orthoimage generation to derive valuable base products for a variety of geoscientific investigations. The methods employed are similar to those developed and applied within various airborne DLR projects in recent years (Neukum, 1999; Wewel et al., 2000; Gwinner et al., 2000).

DLR's photogrammetric processing system, comprising digital terrain model (DTM) generation based multi-image matching, ortho-rectification and image mosaicking, represents the major aspect of the photogrammetric and cartographic activities and makes it possible to provide photogrammetric data products to the team. The operational and standardised generation of products is intended to improve the availability of higher-level data products (orthoimages and 3D surface descriptions are available within days; Scholten et al., 2005), to ensure the full exploitation of the entire HRSC potential (multi-stereo capability for reliable 3D modelling, as well as precise high-resolution and multi-spectral orthoimage generation), and comprises a high degree of automation. The preliminary products currently include HRSC DTMs on 200 m grids and orthoimages at resolutions of 12.5, 25.0 or 50.0 m/pixel of all sensors, derived using the corresponding HRSC DTM. Based on predicted pointing and reconstructed orbit data, the accuracies of these products are a few hundred metres for planimetry, and better than 100 m for height measurements.

Figure 6 indicates the quality of HRSC preliminary products compared with the topography described by the Mars Orbiter Laser Altimeter (MOLA). Besides the production of additional, more elaborate high-level data (Gwinner et al., 2005), adapting processing parameters to specific data characteristics), the described standardised processing also provides inputs to other photogrammetric investigations (Albertz et al., 2005). Finally, this system is designed to integrate the results of these investigations for the derivation of enhanced data products, such as high-quality regional or global image and DTM mosaics.

3.1.1.1 An Alternative Approach to Stereo Photogrammetric Processing of HRSC Data Based on ISIS and SOCET SET

Although the primary role of the US Geological Survey, Flagstaff, USA, in the HRSC experiment is advisory rather than operational, this group has developed and demonstrated its own capability for stereo processing. The approach chosen was to integrate Level-2 (radiometrically calibrated, geometrically raw) HRSC and SRC images into the USGS planetary cartography software system ISIS (Torson & Becker,

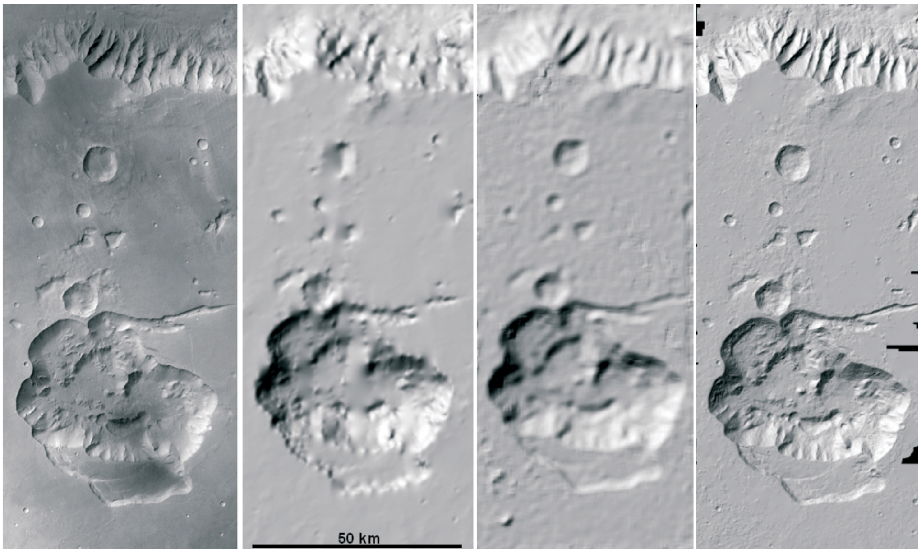

Fig. 6. Subset of the Mars Express orbit 1070 (~7°S, 298°E). From left to right: standardised HRSC orthoimage 12.5 m/pixel, gridded MOLA DTM (Smith et al., 2003); preliminary HRSC 200 m DTM (Scholten et al., 2005); and high-resolution HRSC DTM, 50 m grid (Gwinner et al., 2005).

1997; Eliason, 1997; Eliason et al., 1997; Gaddis et al., 1997) and from there into the commercial photogrammetric software SOCET SET (*www.baesystems.com*; Miller & Walker, 1993). In addition, it was necessary to develop sensor models for the two cameras in the ISIS system; in SOCET SET, available 'generic' models could be used.

The benefits of this work include preparing the USGS to undertake systematic mapping if directed by NASA, providing capabilities for cartographic processing of HRSC data to the many researchers who use ISIS rather than VICAR, and bringing to bear on the images the largely unique ISIS capabilities for photometric function modelling, photometric correction of images and mosaics (Kirk et al., 2001), and topographic modelling by photoclinometry/shape-from-shading (Kirk et al., 2003).

Initial work (Kirk et al., 2004) has demonstrated the production of high-resolution DTMs from stereo pairs made up of HRSC-SRC and MGS MOC-NA images, by exploiting the multi-sensor capabilities of SOCET SET. Subsequent work (Kirk et al., 2006) undertaken as part of the HRSC DTM test (Heipke et al., 2006) has shown that DTMs can be produced from HRSC scanner data and can be used to do useful spectrophotometric processing. The quality of stereo DTMs is intermediate compared with the results obtained by other processing approaches, but refinement by photoclinometry can dramatically improve the geological detail at the limit of resolution while preserving absolute accuracy, even in areas of highly variable albedo.

3.1.1.2 Improving Position and Attitude of the HRSC camera

The 3D orbit position and attitude of the HRSC are given by nominal values, which in the case of the orbit position are refined by Doppler shift measurements. For highly accurate photogrammetric applications, these values are often not accurate enough. Therefore, a photogrammetric approach to compute orbit and attitude improvements has been developed in close cooperation between the Leibniz University Hannover, the Technical University of Munich and DLR.

The approach consists of two independent steps. First, a large number of tie points between the multiple stereo strips is extracted by digital image matching (Heipke et al., 2004). Subsequently, a least-squares bundle-block adjustment (BBA) is performed to improve the exterior orientation (EO), using the generated tie points as direct observations for the unknown EO parameters. By introducing only a bias and a drift value for each orientation parameter per orbit, the BBA preserves the high relative accuracy of the available information, corrects for camera/spacecraft misalignment and improves the absolute accuracy significantly. In order to fit the matched HRSC

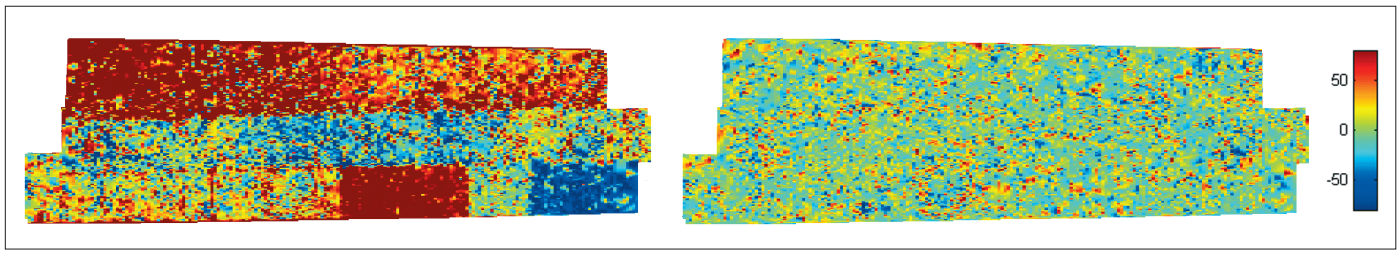

Fig. 7. Differences between HRSC and MOLA points before (*left*) and after (*right*) BBA (in metres).

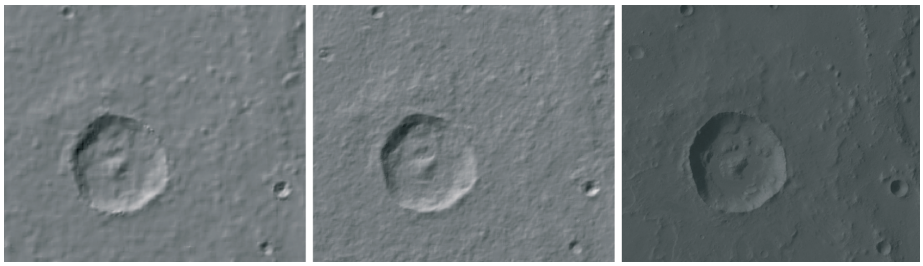

Fig 8. Test area (orbit 18). *Left*: shading based on the original point cloud; *centre*: shading based on the accepted point cloud; *right*: HRSC ortho-image.

points to the existing MOLA DTM (Smith et al., 2003; Neumann et al., 2003), which can be considered as a reference for Mars, further constraints are added to the BBA (Ebner et al., 2004).

For more than 68% of the images (903 orbits) a successful BBA was achieved, and the remaining imagery was processed successfully to improve poor image quality. For reasons of brevity, we report here only results for a selected block comprising the orbits 894, 905 and 927 with a ground pixel size of approximately 15 m in the nadir channel. First, the EO was improved by BBA without taking into account the MOLA DTM. The theoretical standard deviations of the object points after BBA were improved by factors of 2 to 3, and lay in the range of about 5–7 m in the *X* (flight direction) and *Y* (across track) directions. The *Z* (height) accuracies of all orbits were about 11–16 m.

Next, the HRSC object points were tied to the MOLA DTM, resulting in statistically highly significant improvements for position and attitude. In addition, the root-mean-square (rms) differences between HRSC and MOLA DTM could be reduced by a factor of 3. Hence, we have reached a high consistency between HRSC points and the MOLA reference. This is clearly visible in Fig. 7, which compares the *Z*-differences before and after the BBA. With the resulting adjusted EO, high-quality products such as DTMs, orthoimages and shaded reliefs can be derived from the imagery.

3.1.1.3 Quality Assessment of HRSC Object Points and Improved DTM Generation

The point cloud resulting from the standardised stereo-photogrammetric VICAR processing is dependent on albedo features. Generally, in rugged areas (e.g. craters, valleys, chaotic terrains) many high-quality points can be determined, whereas smooth areas are poorly described, with a high measurement noise and data gaps.

A point classification method developed by the group at the Vienna University of Technology has been applied iteratively to reduce the measurement noise (Attwenger & Neukum, 2005). The basic idea is to start from a coarse DTM and improve it from one iteration step to the next. HRSC points are either accepted or rejected depending on their distance from the intermediate DTM until a stable condition is reached. The initial DTM may be derived from a reduced HRSC data set or from MOLA data. The latter can also bridge large gaps in regions without points.

The results show the elimination of gross errors and a reduction of the mean measurement noise. Thus, features are better discernible in DTMs derived from the accepted points, and smaller grid widths can be used for DTM generation (Fig. 8). It should be noted that all employed points are original measurements. Thus, any

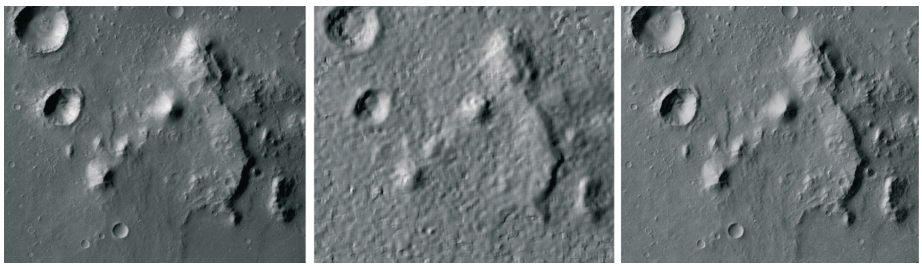

Fig. 9. A 495 × 565 subsection from HRSC orbit 927 with 50 m ground pixel size (scene size 25 × 28 km). (a) Photometrically corrected irradiance of the original orthoimage derived from the corresponding HRSC nadir image and a standard Level-4 DTM. (b) The modelled scene radiance of this obviously relatively crude DTM. (c) The modelled scene radiance of the SFS-refined DTM. The fact that (c) is almost indistinguishable from (a) demonstrates the potential of SFS.

interpolation algorithm (e.g. linear prediction with the capability for further noise filtering) can be applied to derive a regular, grid-based DTM from these points.

3.1.2 Improvement of Spatial Data by Shape from Shading

Besides the USGS (see above) the Munich UniBw group has also refined the standard Level-4 digital elevation models (DEM) by means of shape-from-shading (SFS). Surface inclinations and elevations are derived from illumination-induced shading information in the HRSC images. SFS, although dependent on spatial and physical factors such as reflectance, surface albedo, shadows, light source distribution, image resolution, etc., is in principle not only capable of realistic interpolation into a coarse elevation grid but also guarantees conformity with photometric image information. This is prerequisite for subsequent modifications of image shades towards rigorous homogenisation and optimisation of relief shading in the final orthoimage maps (Dorrer et al., 2005; Albertz et al., 2005) (Fig. 9).

3.1.3 DTM Test Using HRSC Imagery

As described, automatic DTM generation from HRSC images by means of image matching has reached a very high level over the years. In addition to the systematic processing, several groups have been able to produce DTMs using different approaches, or have developed alternative modules for parts of the DTM generation process. It was therefore considered desirable to compare the individual approaches for deriving DTMs from HRSC images in order to assess their advantages and disadvantages (Heipke et al., 2006).

The key goals of the test were to reconstruct the fine details and the geometric accuracy of the DTMs. Fine detail was studied using a variety of qualitative assessments in small but representative areas, while geometric accuracy was analysed with respect to the MOLA DTM. All quality parameters were also related to operational aspects such as the computing effort of the applied method, and thus its applicability to generating DTMs of large areas (multiple orbits, potentially the whole HRSC dataset). The test was organised by the Photogrammetry and Cartography Working Group (PCWG) within the HRSC CoI team under the auspices of the ISPRS Working Group IV/7 on Extraterrestrial Mapping. IPI, Leibniz University of Hannover, and DLR Berlin–Adlershof acted as pilot centres for the test. Based on commonly agreed test datasets, including image orientations refined by bundle adjustment, a total of seven groups have derived DTMs. The pilot centres then analysed the data produced. To our knowledge this is the first multi-site test for DTM generation from planetary imagery.

The test was very successful and demonstrated that a number of methods can be used to generate high-quality DTMs from HRSC imagery. Nevertheless, there were notable differences between the participants' results. Some approaches, not surprisingly those that were developed with planetary imagery in mind, yielded superior results, and have been extensively applied to planetary and in particular to HRSC image data in the past. Most operational methods, in terms of processing time, needed only a few hours. The best approaches yielded a DTM resolution of two

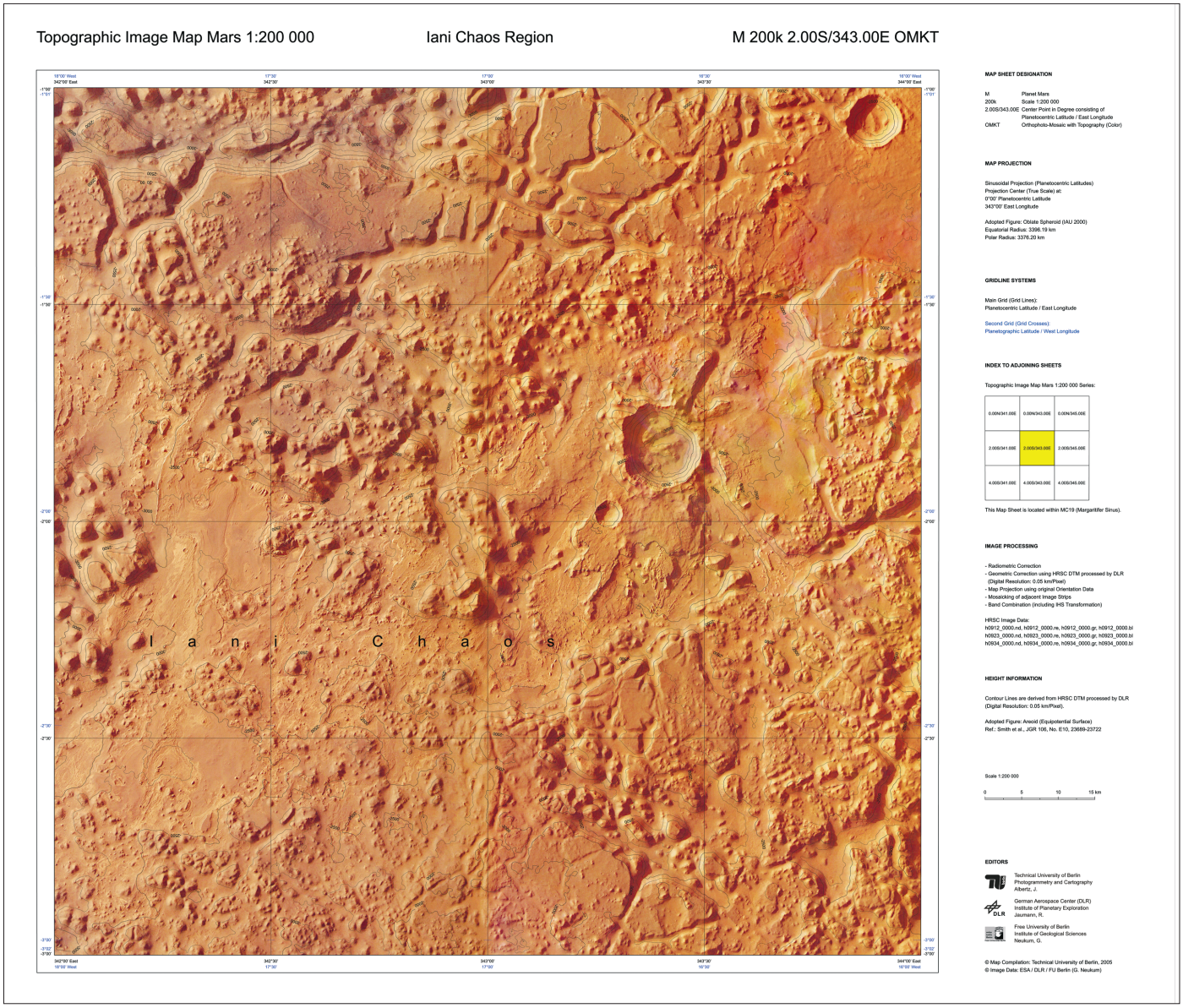

Fig. 10. Example of a sheet from 'Topographic Image Map Mars 1:200 000' showing the Hellas and Centauri Montes region.

to three times that of the nadir image, and a geometric accuracy with respect to the MOLA DTM of one to two pixels in object space depending on the terrain difficulties, still provided operational production times of only a few days processing per orbit. Shape from shading is able to refine the matching DTM to a remarkable degree of detail. Furthermore, the test confirms previous findings that the DTMs generated from HRSC data, at least at lower latitudes, are clearly superior to the MOLA DTM in terms of resolution and visible fine detail.

On the basis of these results, some inferences can be made for further development of the matching algorithms:

— the use of multiple images instead of only the nadir and the two stereo channels often improves the results;
— the reduction of radiometric noise prior to image matching appears to carry a lot of promise (see also Gwinner et al., 2005; Schmidt et al., 2006);
— rectifying the images at least to a plane prior to matching is mandatory. More advantageous seems to be a rectification to a DTM such as the MOLA DTM or,

even better, one generated within the matching process, in particular in areas with steep slopes;
— detecting and eliminating blunders must be seen as an essential sub-task at every step in the processing chain; and
— general purpose algorithms should be carefully adapted to the peculiarities of the HRSC sensor, e.g. the geometric sensor model, macro pixel formats and varying integration times. We were also able to demonstrate within the test that in order to generate consistent results a photogrammetric bundle adjustment using a sufficient number of tie points is necessary.

3.1.4 Mapping of the Martian Surface with HRSC Data

The cartographic standard product of the Mars Express mission is the 'Topographic Image Map Mars 1:200 000' (Albertz et al., 2004, 2005). This large-scale map series is compiled in equal-area map projections, i.e. the Sinusoidal projection between latitudes 85° north and south and the Lambert Azimuthal projection in the polar regions. Mars is covered by a total of 10 372 individual map sheets.

In order to automate the map generation process, the cartographic software package Planetary Image Mapper (PIMap; Gehrke et al., 2005) has been developed at Technische Universität Berlin. The software generates and/or compiles the topographic map content, i.e. the ortho-image basis, contour lines derived from HRSC DTM, topographic names and gridlines, as well as map titles and further marginal information. The resulting digital map sheets contain all raster and vector data in pdf format, and can be printed out on demand. Using PIMap, various sheets of the 'Topographic Image Map Mars 1:200 000' series, special target maps at larger scales, and thematic maps of different types have also been generated. An example is given in Fig. 10.

3.1.5 3D Visualisation

Following the concept 'from 3D camera to 3D image' and based on the stereo-capability of HRSC, the 3D Visualisation Group of the Institute for Cartography of the Dresden University of Technology have developed an optimised cartographic true-3D display method by merging the well known principles of transparent prismatic microlens foils, which have been used for so-called 'flip images' and the lenticular foil technology, and so far have been used for displays with only a few discrete levels of depth. This approach allows the production of hardcopy displays that permit spontaneous, glasses-free viewing without artificial illumination by several individuals simultaneously. For the Mars surface, bitemporal 'three-in-one' scenes showing dynamic geological processes have been generated (see the cover page of the special issue of *Photogrammetric Engineering & Remote Sensing* on planetary mapping, October 2005). For background information about this method, see Buchroithner et al. (2005a, 2005b).

3.1.6 Automated Cartographic Feature Extraction from HRSC imagery

The production of global-scale DTMs with associated ortho-rectified high-resolution images opens up the potential to mine the resultant datasets for significant geomorphometric features such as craters, sand dunes, lava flows and hydrological remnants. Automated crater detection using image data-mining techniques has been described by Kim et al. (2005) and its reliability has been demonstrated with Viking orbiter, MOC and HRSC data to be over 85% (Kim et al., 2005). We show here some examples of the extension of this approach to the use of stereo fusion for both crater detection from multiple HRSC looks (Fig. 12), as well as the detailed geomorphometry of the crater shape (Fig. 11). It is planned to continue development of these data-mining techniques so that a much wider range of geologically important features can be automatically detected, leading in the very long term to the production of geological feature maps. These crater databases can also be employed for surface date aging (Kim et al., 2005) using size–frequency distribution (SFD).

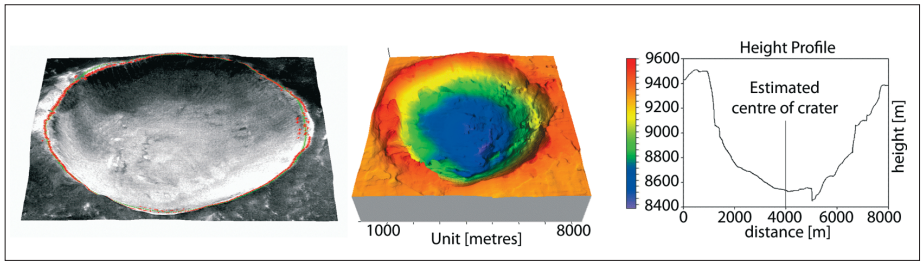

Fig. 11. Stereo HRSC-derived DTMs of an impact crater (Claritas Fossae, orbit 68). Detailed view of the large crater a little left of the centre in Fig.12. The crater has a radius of approximately 3.6 km. *Left:* 3D view, rendered with nadir image showing the detected crater rim (red) and fitted conic section (green). *Centre:* colour-coded and hill-shaded DTM. *Right:* height profile.

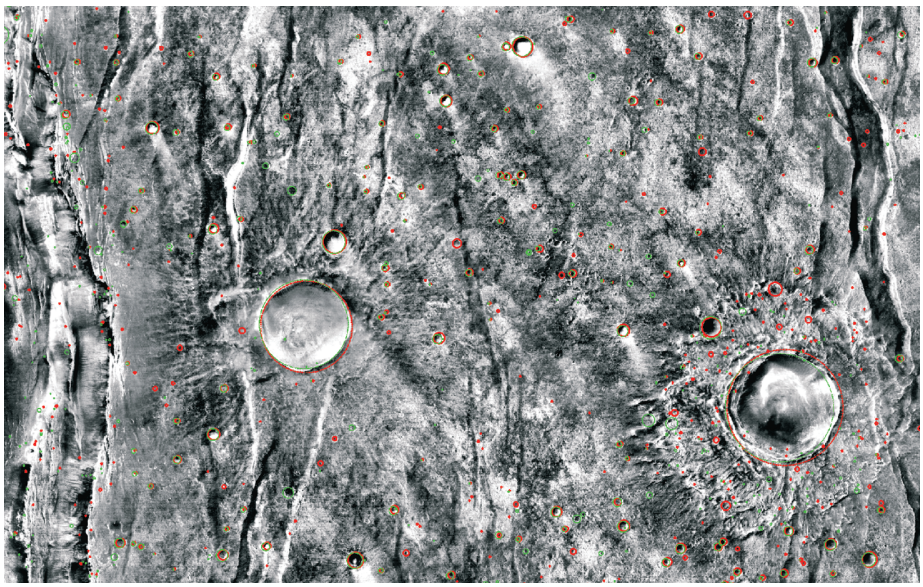

Fig. 12. Stereo detection of large craters (>5 pixels) showing locations from nadir (red) and forward view (green) of a small area near Claritas Fossae (orbit 68).

3.2 Spectrophotometry

3.2.1 Introduction

The HRSC on Mars Express has four basic capabilities – imaging, stereo, photometry and colour – that reveal landforms and clouds as well as topography, surface physical characteristics and compositional units. We summarise here some of the results of an initial analysis of the HRSC colour data. The colour data can be used to identify and map spectral (often compositional) units present on Mars, with some implications for our understanding of the martian geology.

The HRSC camera has been described by Neukum et al. (2004b) and the HRSC investigation by Jaumann et al. (2007). The HRSC focal plane consists of nine linear-array Si-CCD detectors, each consisting of 5184 pixels that view the scene, oriented perpendicular to the orbit track. An image is built up by repeatedly reading out each array as the spacecraft orbits over the surface and the scene sweeps across the camera's focal plane. Each detector array views the scene at a different angle spread out from forward to aft of nadir so that each detector views a different line in the scene at any instant in time. Four of the detectors (panchromatic channels) plus the nadir channel are used to produce DTMs and another is the nadir-viewing channel. All five of these detectors have the same filter over them, constraining the viewing to a specific spectral channel centred at 675 nm. The other four detectors (colour channels) each have a different filter over them, providing four different spectral channels (445, 540, 750 and 955 nm). The field of view at the surface for one pixel in the line array at nadir and 250-km orbit altitude is nominally 10 m (40 µrad or 8.25 arcsec). The colour channels are normally operated in a macro-pixel mode of 2 × 2, 4 × 4 or 8 × 8 pixels summed on the spacecraft into one pixel to reduce the data volume (see section 2).

3.2.2 Colour Data Characteristics

The colour data characteristics have been investigated extensively in order to understand how the data may be used for studying spectral units and Mars' geology and atmosphere, and a lengthy report on this study is given in McCord et al. (2006). In summary, these characteristics include the effects of data compression and of the different angles of viewing among the colour channels. The degree of data compression is different in each colour channel and from place to place on Mars, and this can affect the appearance of colour units. However, it is found that this effect is usually at the few-DN level and is worst where the surface has least albedo and colour features. The differing angles of observation for each colour channel have a more serious effect because the atmosphere can be highly scattering with directionality, and it can contribute considerably differently to each channel, depending on the solar illumination. The surface roughness also can cause different amounts of shadow to appear in each colour image with different viewing angles. Finally, differences in surface photometric functions can create false colour differences.

In addition, the HRSC observes such large swaths of latitude across Mars in each orbit that the solar illumination angle varies greatly within a swath and among swaths, including from equator to pole. McCord et al. (2006) report that applying a simple cosine brightness correction works surprisingly well for removing the first-order effects from the data, but a more complex correction should be attempted for some studies. Since the colour channels each observe the surface at different angles and times, the colour images must be spatially registered in order to construct colour unit maps. This registration process is difficult and resource consuming, so that misregistration and the associated colour artifacts are problematic, especially for topographically complex terrains, unless special efforts are made to register to a few tenths of a pixel dimension.

3.2.3 Comparison with OMEGA and Telescopic Observations

An extensive analysis was conducted (McCord et al., 2006) to compare HRSC spectrophotometric measurements with those of the same regions by other instruments. In summary, this study revealed that the HRSC blue, green and infrared channel I/F values agree with measurements by OMEGA visual channel and telescopic observations, but that the HRSC red channel I/F values are offset from these other measurements, with HRSC being higher in I/F. A search for the reasons for this offset has been inconclusive so far. Possible reasons include a basic error in the HRSC calibration or a change in its performance since ground calibration, an error in the OMEGA visual channel calibration, or an atmospheric or surface scattering effect due to the HRSC red and infrared channels being offset from each other in viewing angles by nearly 30°. Interestingly, a comparison of HRSC and OMEGA measurements for the small Mars satellite Phobos shows this effect but at an even greater size. Phobos has no atmosphere and is relatively dark, so this suggests a calibration error in one or both instruments. An analysis of the potential atmospheric effects on the HRSC spectrophotometric data, due to the differing viewing angles of the four colour channels, was conducted using radiation transfer calculations. This revealed that extra scattering contributions to the red channel could be expected under dusty atmospheric conditions. Further, examples were found where water clouds high in the atmosphere created just such an effect. However, an investigation searching for variations of this effect with solar phase angle revealed no conclusive dependence, in apparent contradiction with this explanation (McCord et al., 2006; Coombs & McCord, 2006).

In spite of these complications, the HRSC colour dataset is a powerful resource for studying Mars. The colour data have been demonstrated to be very good for defining the basic spectral components of Mars and showing their spatial distribution. Thus, HRSC spectral images are an important asset for photo interpretation and mapping. They also are the best link between OMEGA spectroscopy and photo interpretation. By showing that HRSC I/F spectra are consistent with, but slightly offset from, the same wavelengths of OMEGA, telescopic and laboratory spectra, we have validated that familiar compositional information is contained in the HRSC images. The HRSC spectral data, however, were

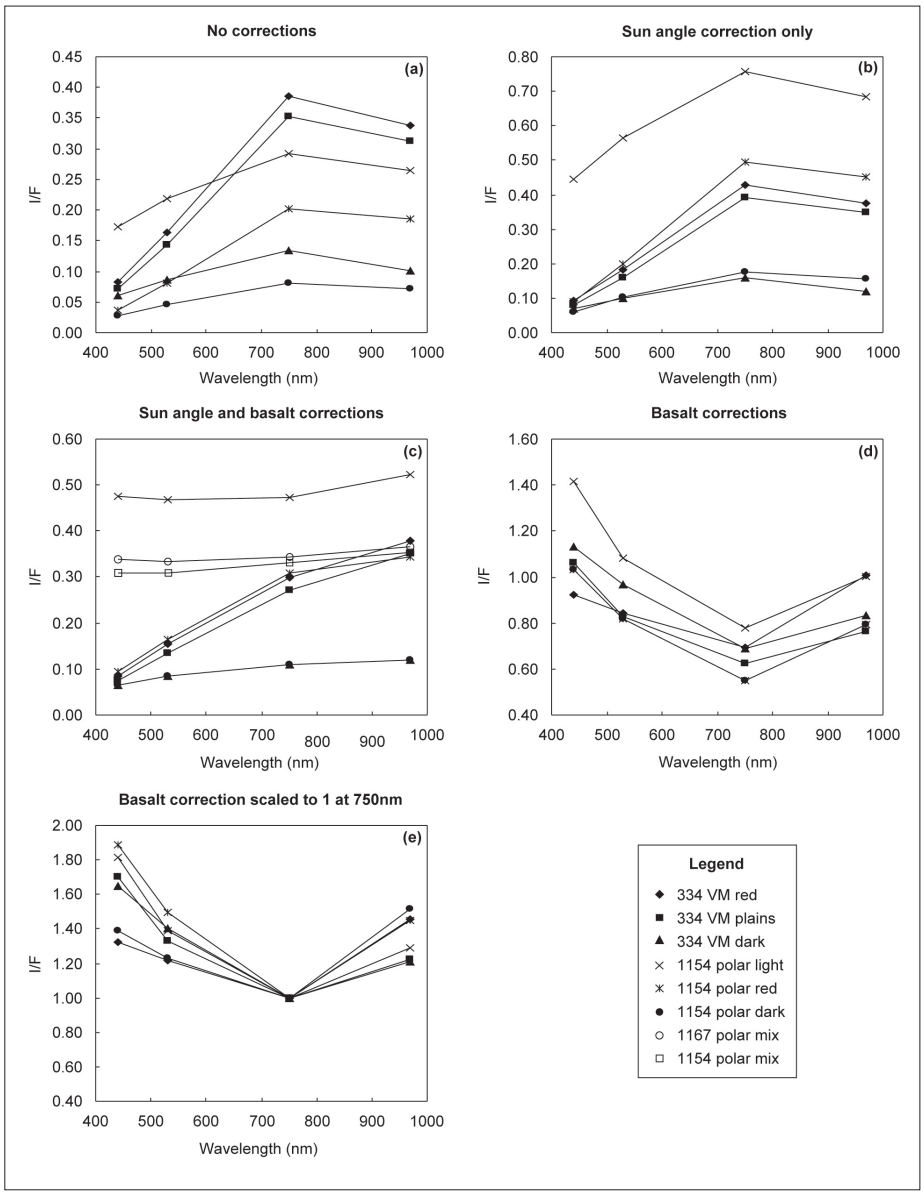

Fig. 13. HRSC four-colour spectra plotted for selected areas in several orbit image stripes, as designated in the legend by orbit number and spot name. (a) Spectra as delivered by HRSC after radiometric calibration. (b) Spectra after correcting for solar illumination angle according to a cosine function. (c) Spectra after also applying the corrections to force the HRSC spectra for dark material to agree with a laboratory basalt spectrum. (d) The basalt correction factors for each of the orbit scenes. (e) The basalt correction factors scaled to unity for the 750 nm channel (McCord et al., 2006).

never intended for identifying composition. There are neither enough spectral bands nor broad enough spectral coverage. OMEGA data are intended for this purpose. The power of the HRSC colour data lies in having both high spatial resolution and broad spatial coverage in the four main colour bands. Combined with OMEGA, it is a unique dataset.

3.2.4 Reflectance Spectra

In spite of the complications described above, and the effects of the atmosphere, *I*/*F* values for the surface units can be calculated if one assumes knowledge of the spectrum of at least one unit in a scene. This approach was used by assuming the darkest units in each scene are composed of basalt and correcting the HRSC dark unit spectrum to match a laboratory spectrum of unweathered basalt and applying this correction to all other pixels in the scene. The example *I*/*F* spectra produced following this procedure, presented in Fig. 13(c), are for specific pixels and locations on Mars that were carefully selected to illustrate three different spectral units and probably classes of material (McCord et al., 2006).

Figure 13 shows HRSC *I*/*F* values for six Mars spots with only the HRSC standard calibration applied. Fig. 13(b) shows these *I*/*F* values corrected for solar illumination angle using the simple cosine function. Then, the 'basalt correction' is applied and the results shown in Fig. 13(c), where first there is a spectrum for the dark, slightly red material that is the basalt we chose for the reference material.

For the scene we analysed in orbit 1154 data it is called 1154 dk stuff. Different dark material deposits were used in each scene analysed. The correction spectra shown in Fig. 13(d) and (e) are similar in overall shape and suggest that this material has similar spectra in all the scenes analysed here. Then, there are spectra for the brighter and much redder material that is the classic oxidised iron-rich red plains material, characterised here by areas named 334 PP01 b, 334 PP01 e, and 1154 red. Again, this class of material appears to have similar spectra in most places where morphology, terrain, albedo and colour suggest its presence. Finally, there are nearly flat spectra for the very bright, white or slightly red material. This spectrum type is found in the brightest areas in the polar regions and appears to represent the least-contaminated water ice. The fact that we find nearly white material (flat spectra) in these brightest, apparently snowy, polar regions suggests that this method of correcting for the atmosphere using the basalt assumption is working fairly well. This is also suggested by the similarity of the basalt correction factor from scene to scene and orbit to orbit. Since these orbits span considerable periods of time and conditions on Mars, this finding is heartening and a little surprising. One might expect the atmosphere effect to be more variable with time and location, and this should be further investigated as it suggests a possible additional effect.

3.2.5 Basic Spectral Components

The most familiar representation of HRSC spectral information is a colour-composite image employing blue = 445 nm, green = 540 nm and red = 750 nm. In such colour composites, most of the martian surface has reddish tones, and the darker areas typically are blue when strongly contrast stretched (Figs. 14 and 15). Combinations of red and blue are common (associated with the colour magenta in these colour composites), and red areas vary considerably in albedo and may appear white in strongly stretched images. Colour composites by themselves, however, often are ambiguous. For example, high-albedo red rock may appear similar to ice in polar images, and dark rock may be difficult to distinguish from shadows and shading. Thus, to define spectral extremes, we (McCord et al., 2006) prepared principal-component images, ratio images, spectral angle images and fraction images. Each of these analytical techniques has advantages and disadvantages (Adams and Gillespie, 2006), but in combination, and using the image context, it became clear that there are three basic spectral components in the north-polar images (ice, red rock and dark rock), and in the Valles Marineris area there are only two spectrally dominant components (red rock and dark rock). It is significant that the same red and dark rock components occur in both polar and equatorial areas. In addition, there are a few areas in some of the equatorial images that stand out in the residual image because they are *not* fully explained by the basic spectral components. These additional components can be detected as residuals after first defining the dominant components as the spectral background. In some cases when an additional spectral unit seems to be present in many pixels, its spectrum might be guessed at, perhaps guided by OMEGA or laboratory inputs, and an iterative linear mixture modelling approach used that allows more end members than the dimensionality of the multispectral data set (e.g. Pinet et al., 2000).

Relatively uncontaminated volatile condensate ('ice') on the north polar cap is distinguished in HRSC spectral images by its high reflectance in all channels, as seen in the spectra plotted in Fig. 13, the colour composite images in Fig. 14, where blue is assigned to the 440 nm channel, the colour-composite images are contrast-stretched to show areas of pure ice as white or lightest blue. In the same images where red is assigned to the 750-nm channel, high-albedo areas that appear light red are interpreted to represent ice that is contaminated with red-rock material, presumably in the form

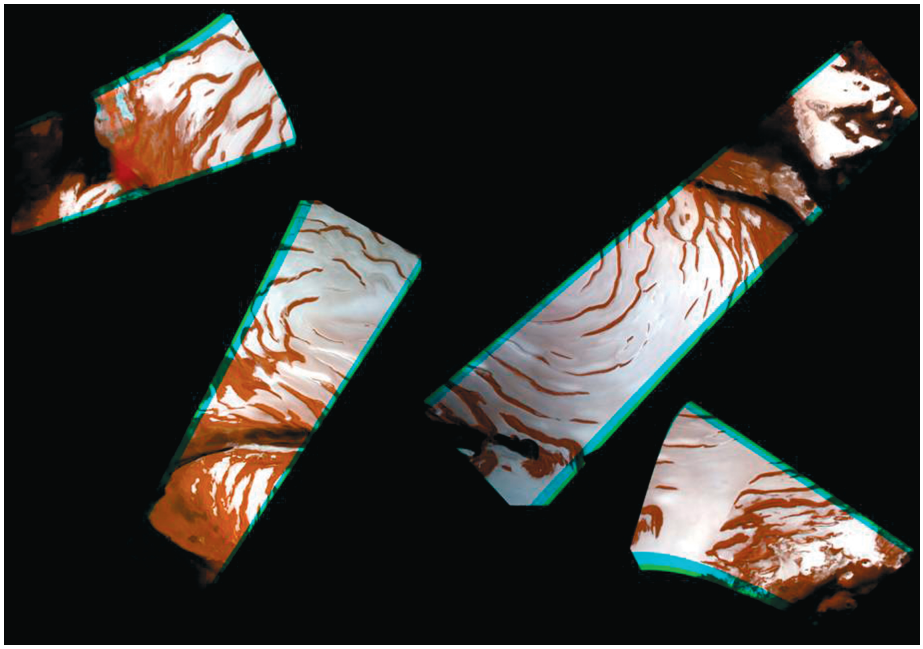

Fig. 14. RGB colour images made from the red, green and blue HRSC image datasets for orbits 1169, 1154, 1167 and 1087 (left to right). The location of these image strips on Mars is in the north polar region. Note that some of the image areas overlap, although they are separated here. No correction for the solar illumination angle has been made (McCord et al., 2006).

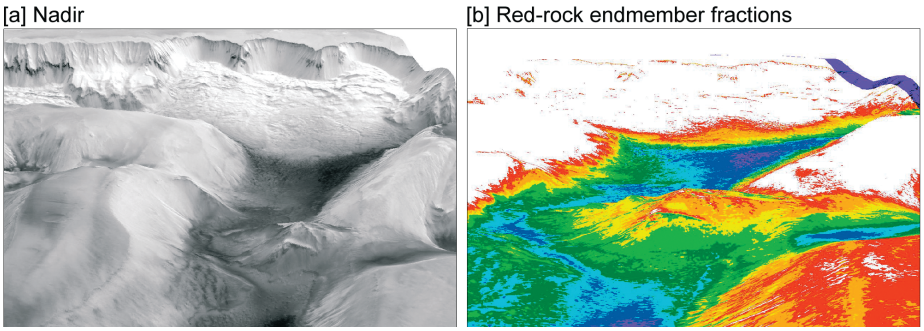

Fig. 15. Nadir and normalised-fraction images of an enlarged part of orbit 334. View is toward the north wall of Ophir Chasma. (a) Nadir image combined with a digital elevation model. (b) Colour-ranked 10% fraction intervals of the red rock spectral unit combined with a digital elevation model (McCord et al., 2006).

of fine dust. The relatively few spectral units found and their suggested identities (McCord et al., 2006) are consistent with past studies of the spectral nature of the Mars surface, including from Viking Orbiter (McCord et al., 1982). This characteristic of Mars, when studied with a few relatively broad spectral bands at visible wavelengths to the spatial resolution used so far, seems to be due to the nature of Mars and not to a fault in HRSC or other instruments.

3.2.6 Geological Interpretation of HRSC Spectral Images

In the Valles Marineris region, we find two of the same dominant spectral types as in the north polar area: red rock and dark rock. Because the materials implied tend to dominate spectral mixtures, the absence of unequivocal evidence for other spectral types in the HRSC images, such as salts (Montgomery & Gillespie, 2005) or ice (e.g. Gillespie et al., 2005), does not mean that other materials are not present, possibly in large amounts. Thus, we consider it important to keep in mind that the observed spectral components (iron oxide and basalt) can act as strong pigments that may have only minor importance volumetrically. Geological context and other spectral information (e.g. OMEGA) may help to determine whether the HRSC spectra imply volumetrically large amounts of the materials that are represented by the spectral units, or whether we are measuring the proportions of lesser components that happen to be spectrally dominant.

In the context of the HRSC images, the red and dark spectral types define two main geological units in the Valles Marineris region. In Fig. 15 we show an example map of the proportions of these two units. The red unit dominates the plains that surround the canyons, the upper parts of the canyon walls, and some of the islands within the larger chasmata. Local outcrops of the red unit occur within the dark unit on the valley floors. In HRSC nadir images and MOC images, some of these outcrops exhibit fine layering. The dark unit makes up most of the floors of the larger chasmata, where it occurs as extensive smooth plains, occasional dunes and uncommon layered deposits. It also occurs in conical depressions within the red unit, as talus slopes, and in a wide variety of irregular patches. The dark unit is locally present on the high plains near the rims of the chasmata. Although the red unit is topographically above the dark unit on a regional scale, the contact between the two is nearly everywhere broadly gradational, and, locally, dark material appears to have intruded and altered the red unit. Our spectral definitions of the red and dark units have potentially important implications for interpreting the geology of Valles Marineris. The high-albedo deposits within the chasmata are spectrally indistinguishable from the materials that comprise canyon walls, rims and the surrounding plains. If the high-albedo materials all have approximately the same composition, the interior deposits may be part of the Hesperian/Noachian 'basement' that comprises the canyon walls and plains, rather than younger deposits that lie unconformably on the basement, as proposed for example by Witbeck et al. (1991). Many workers have lumped the low-albedo materials in the chasmata together with the high-albedo materials as part of the younger, interior deposits.

Based on our spectral definition of units, however, the dark-material unit is compositionally distinct from the red, high-albedo material. Layers of the dark unit are present in the deepest parts of Mellas Chasma and may be stratigraphically below the red unit. We find no evidence that the red unit occurs stratigraphically below the dark unit, as would be implied if the Hesperian/Noachian basement materials had been down-faulted to form the floor on which younger, dark materials were deposited. Excluding dunes and dust deposits, the main interface between the red and the dark units in the chasmata is morphologically complex and extends over an altitude range of several kilometres. Furthermore, the contact is everywhere gradational. If the dark material is basaltic in composition, it is difficult to explain the observed complex and gradational zone as a depositional contact between dark flows/tephra and overlying lighter deposits. On the other hand, it does not appear that the dark unit is simply intrusive into the red one, although in places there is evidence that the dark material has followed fracture zones into the high-albedo material. We suggest that understanding the interface between the red and dark units is essential for understanding the origin of the Valles Marineris region, and HRSC colour data are well suited for this purpose.

3.2.7 Summary

We have demonstrated that the HRSC colour data can contribute a better understanding of the geology of Mars. We find that only a few basic spectral and probably compositional units (red, iron-oxide-rich material; dark basalt; polar water ice) contribute to most pixels to the degree HRSC can sense them. There is evidence of several other units that are brighter and less blue than the other units, probably salts and possibly other materials, may also be detectable with HRSC. Reflectance spectra from HRSC can be calibrated to a level comparable with laboratory spectra and in agreement with OMEGA visual spectra, allowing compositional interpretations of HRSC spectra and extension and mapping of OMEGA compositional identifications to higher spatial resolution and extent than possible with OMEGA (or HRSC) alone. Our exploration of the bright red and dark apparently basalt units reveals that the unit distributions seem to disagree in important cases with existing geological interpretations exhibited in the published Mars geological maps. Thus, there is much geological exploration that can be

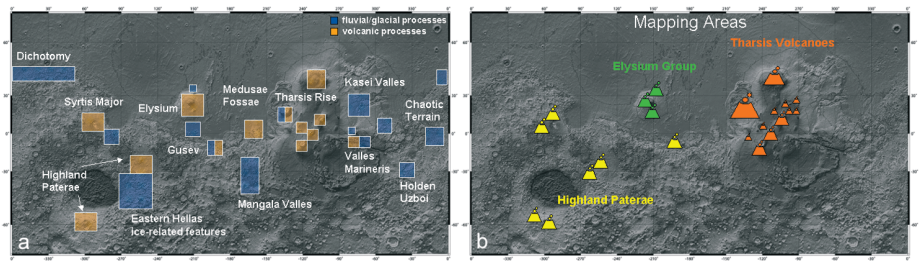

Fig.16. (a) Current working fields on fluvial/glacial and volcanic processes. (b) Volcanic constructs and chrono-stratigraphic relationships.

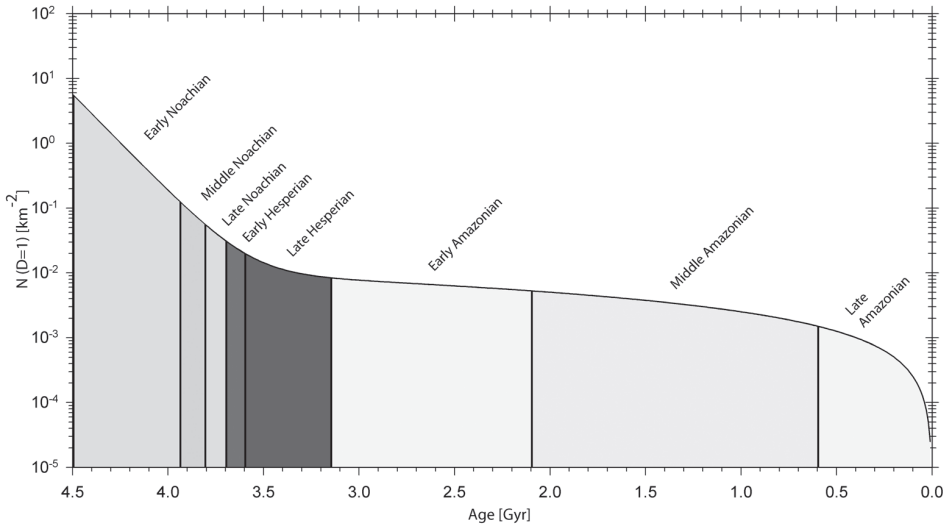

Fig. 17. The Hartmann and Neukum (2001) cratering chronology.

carried out, now that the basic characteristics of the HRSC colour data are better understood and their intrinsic science value is demonstrated.

3.3 Geology and Surface Processes

3.3.1 Stratigraphy and Surface Processes

The locally and regionally good coverage of Mars at high resolution by the HRSC has allowed the team to perform detailed analyses of the stratigraphic relationships and of surface ages through crater-counting methods. A multitude of areas of interest for volcanic activity and corresponding surface evolution, and fluvial as well as glacial activity have been investigated.

Most of the areas marked in Figs. 16(a) and (b) are still under investigation. For some of them, however, hard age data have been acquired and an intermediate assessment of their evolutionary history and of the processes that acted on the surface structures can be given. The relevant measurements in the form of crater size–frequency data have been made by applying the techniques described by Neukum & Hiller (1981), Neukum (1983) and Werner (2005).

3.3.1.1 Cratering Chronology and Absolute Ages

All crater size–frequency data for obtaining absolute ages are related to the Hartmann & Neukum (2001) chronology (cf. Fig. 17) through the expression

$$N_{(D=1\ \mathrm{km})} = 5.44 \times 10^{-4}\,[\exp(6.93T) - 1] + 8.38 \times 10^{-4}T$$

making use of the polynomial expression of the production crater size–frequency distribution for Mars first published by Neukum (1983) and the revised form given by

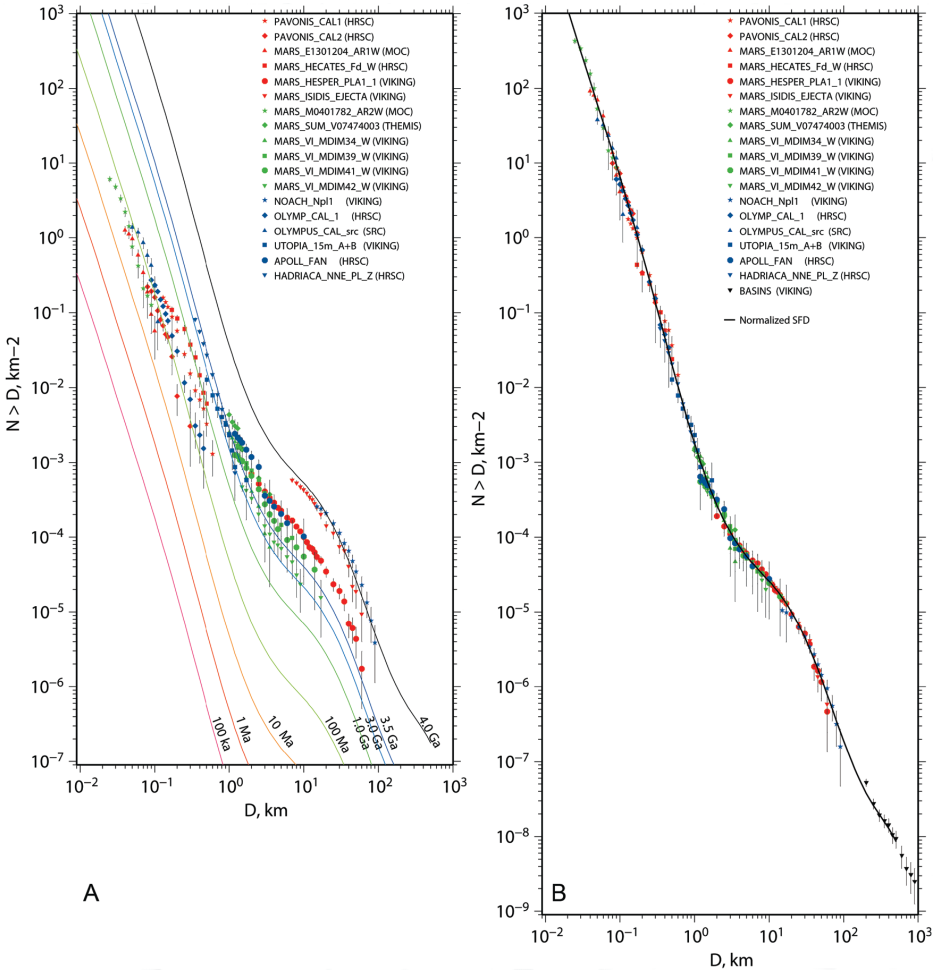

Fig. 18. The martian size–frequency distribution (from Werner, 2005). (a) Assemblage of crater size–frequency measurements obtained for counts performed on HRSC, SRC, Viking, THEMIS and MOC imagery. They represent typical crater size–frequency measurements of differently aged surfaces. The set of isochrones indicate the expected distribution applying the Hartmann–Neukum chronology model for different ages, which makes it possible to derive crater retention ages from the measurements by way of visual interpretation of a graph (Hartmann & Neukum, 2001). Usually, we derive ages by fitting the crater production function to the measurements and obtain a numerical value N(1) for a reference crater diameter (usually 1 km). (b) The same assemblage of crater size–frequency measurements normalised to the UTOPIA 15 m A+B measurement, which represents a measurement in the medium-sized crater diameter range. The black curve is the lunar crater production function transferred to martian conditions, representing a surface age of 3.25 Ga. The good fit strongly suggests that the impactor size–frequency distributions for the Moon and Mars are really the same, and that our previous procedure (Neukum, 1983; Neukum et al., 2001; Ivanov, 2001) of transferring the lunar crater size–frequency distribution to Mars was carried out correctly.

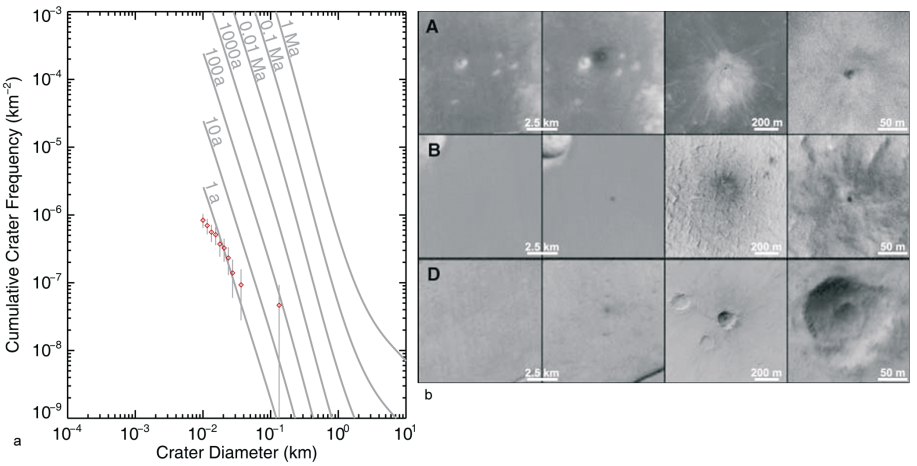

Fig. 19. (a) Isochrons according to Hartmann and Neukum (2001), martian size–frequency distribution by Ivanov (2001). (b) Examples of recent impacts on Mars (from Malin et al., 2006). First column: before impact; second column: after impact (both MOC WA); third column: MOC NA image; fourth column: close-up image of impact site.

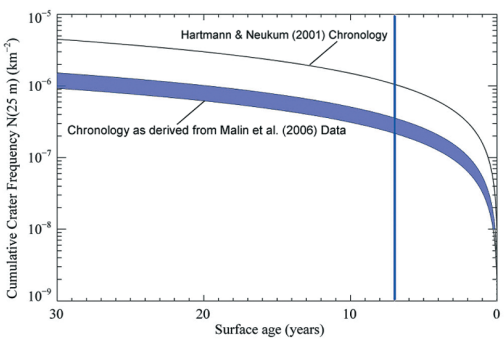

Fig. 20. Malin et al.'s (2006) measurements of recent impacts in comparison with the Hartmann & Neukum (2001) chronology (isochrons and cumulative crater frequencies for craters >25 m).

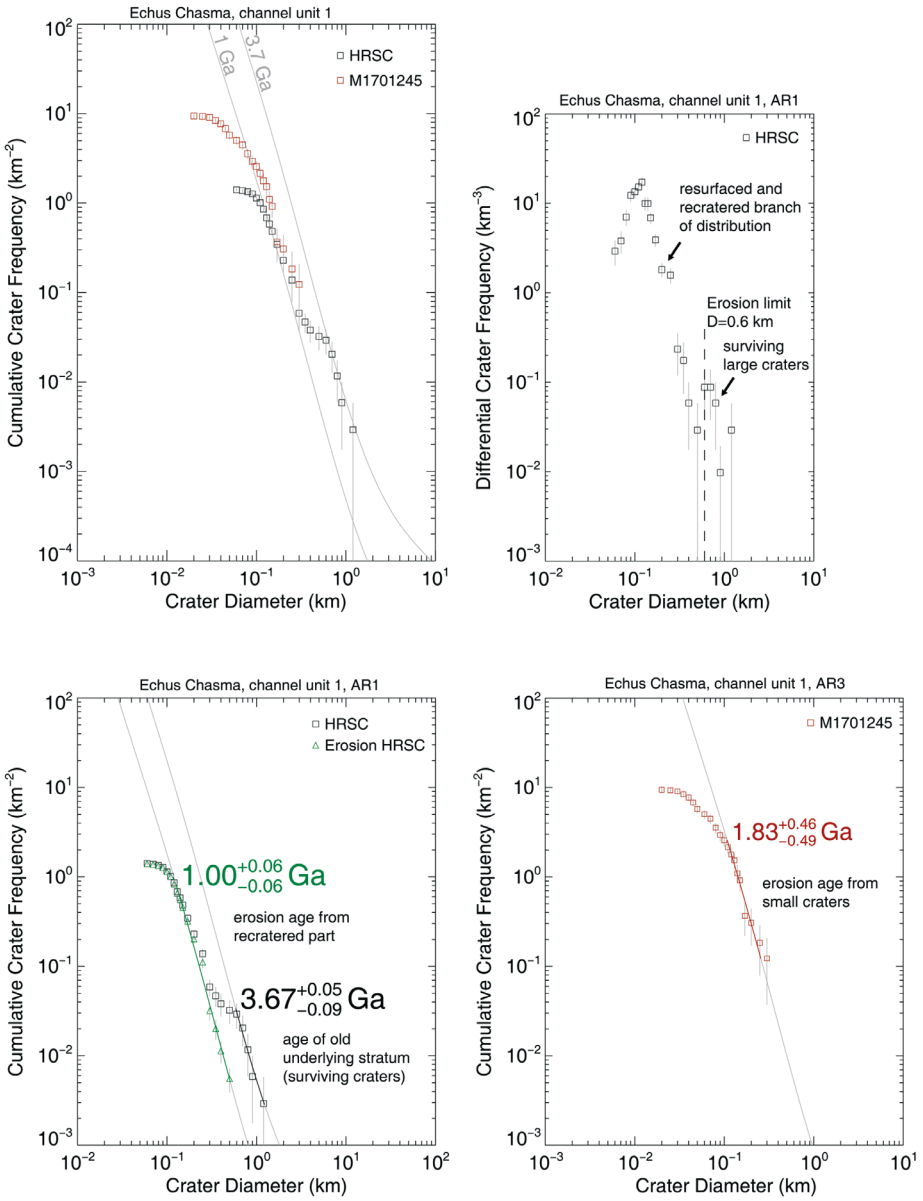

Fig. 21. Examples of crater size–frequency measurements showing characteristic resurfacing effects.

Ivanov (2001). This production function has been confirmed by new measurements carried out by Werner (2005) (cf. Fig. 18).

The Hartmann–Neukum chronology model for recent times, and from that the impact rate ratio Mars/Moon, has been confirmed to be correct at least within a factor of 2 to 3 of crater frequency measurements of the present-day cratering rate on MOC imagery by Malin (2006).

Figures 19 and 20 show our capability to extract resurfacing ages from crater size–frequency distributions and in this way to follow the geological evolution of a surface structure over time. This capability has been greatly improved by applying new analytical techniques to segments of a crater size–frequency distribution where the effects of multiple erosional and/or sedimentary effects with size-dependent destruction of craters can be identified in kinks with related flattening and steepening of the distributions. One of these techniques is described in Werner (2005), and a further refinement of the methodology in Michael et al. (2007). Examples of measurements that show such multistage histories with characteristic resurfacing are presented in Fig. 21.

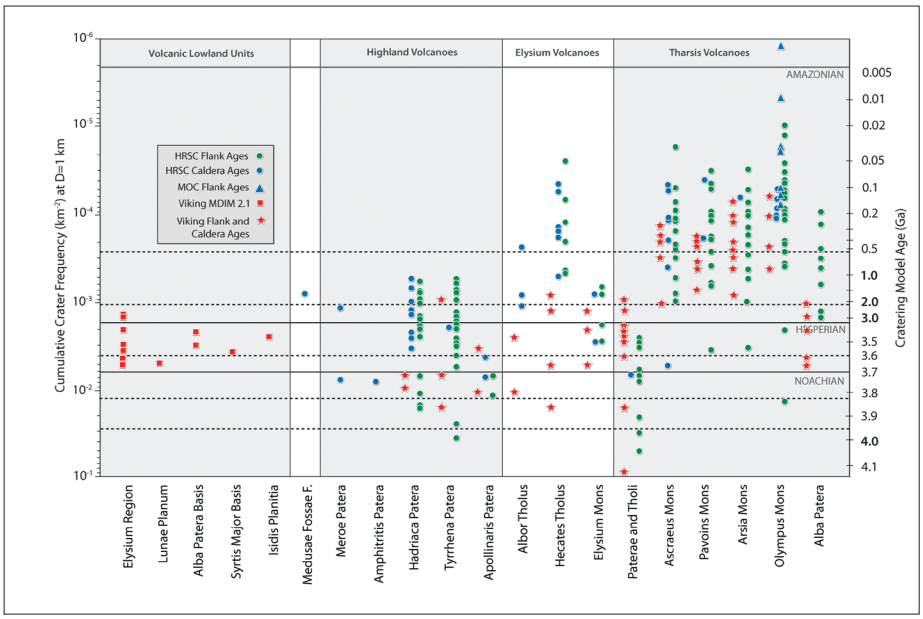

Fig. 22. Ages of volcanic constructs and related landforms. Highland volcanoes formed more than 4.0–3.7 Ga ago and latest activity ended ~1.5 Ga ago. Hadriaca and Tyrrhena Paterae show effusive later phases ~1.5 Ga ago, correlated with fluvial activity. Elysium volcanoes formed more than 3.6 Ga ago, Elysium Mons activity ended 1.5 Ga ago; subsequent activity over the past 2 Ga, Hecates Tholus even past 1 Ga until ~100 Ma ago. Tharsis Paterae and Tholi formed more than 4 Ga ago in major parts, activity ended 3.7 Ga ago. Tharsis Montes, Alba Patera and Olympus Mons formed more than 3.5 Ga ago, and have been episodically active until very recently (2 Ma, Olympus Mons). Possible correlation with SNC ages (Nyquist et al., 2001), SSR: ~1.5 Ga and 150–200 Ma ages in volcanic activity. Medusae Fossae deposits formed ~1.6 Ga ago, when most highland volcanoes were last active (~1.5 Ga ago). Modified after Werner (2005).

3.3.1.2 The Secondary-cratering Problem

Small secondary craters are produced by large primary impacts and can contaminate the crater size–frequency measurements and thus affect the precision of the age determination. For the Moon and Mars, several papers in recent decades (Neukum & Wise, 1976; Neukum & Hiller, 1981; Neukum & Ivanov, 1994; Neukum et al., 2001) have shown that in most cases the effect is minor (<10%) and the majority of small craters found on the martian (and lunar) surface outside immediate secondary strewn fields of large craters are primaries. In particular, the steep part of the distribution at size $D \leq 1$ km is due not to 'background secondaries' (cf. McEwen, 2006), but mainly to the distribution behaviour of primaries. This has been substantiated by measuring the production distribution of small craters directly in the source region, the asteroid belt, on the objects Gaspra and Ida (Chapman et al., 1996a, 1996b). Recently, however, McEwen et al. (2003; 2005) have maintained that the majority of small craters on Mars are not primaries but secondaries produced by large primary craters. They have also proposed the Hartmann & Neukum (2001) chronology to be in error by a factor of more than a thousand in crater frequency, and that in particular all young ages derived through this method based on small craters to be wrong. Obviously, the results of Malin et al. (2006) (cf. Figs. 9 and 10) prove that Hartmann & Neukum (2001) are correct and that McEwen et al. (2003, 2005) themselves must be wrong by a factor of a thousand.

3.3.1.3 Ages of Volcanic Activity on Mars

The ages of a large number of volcanic constructs have been determined from HRSC imagery, often in combination with MOC imagery, and are summarised in Fig. 22.

Volcanic activity has obviously occurred throughout martian history, from more than 4 Ga ago until very recently. The volcanic and fluvial/glacial history of Olympus Mons and direct surroundings, especially the western escarpment area, has been investigated in detail (cf. Neukum et al., 2004a, 2006). The western escarpment of Olympus Mons is shown in oblique view in Fig. 23. The investigated areas on the shield and at the foot of the escarpment are shown in Fig. 24. Olympus Mons shows volcanic resurfacing activity over much of the past ~400 Ma until about 2 Ma ago, and glacial activity until very recently, at least until 4 Ma ago.

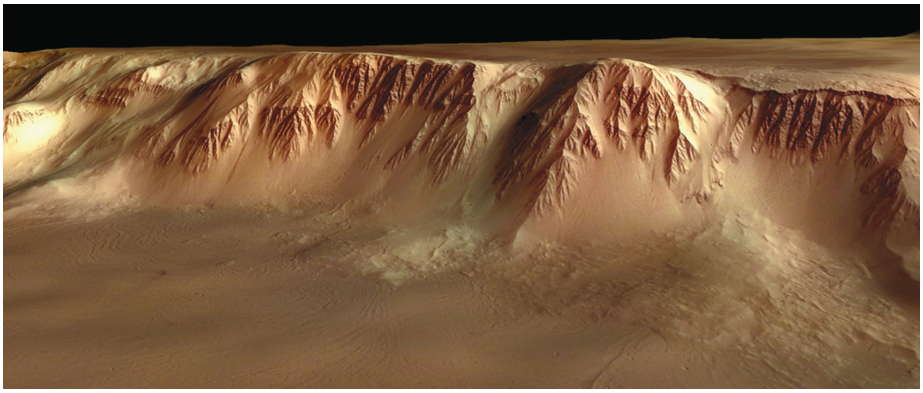

Fig. 23. Oblique view of the western escarpment of Olympus Mons.

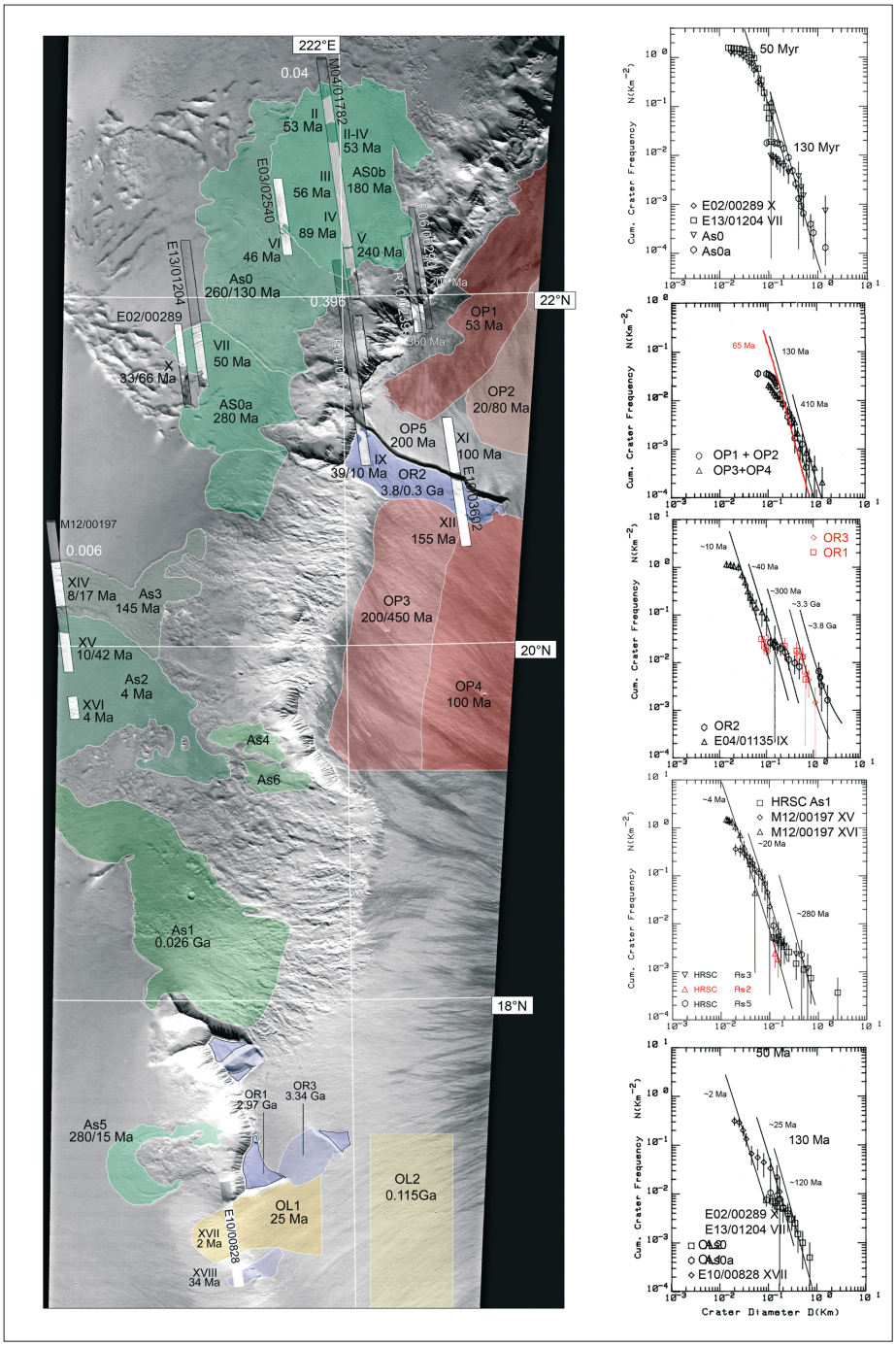

Fig. 24. HRSC image base map with nested MOC data and depiction of the counting areas (left panel) and the resulting ages of the western near-escarpment area of the Olympus Mons volcanic shield, the 7 km-high escarpment and the adjacent plains area to the west with remnants of glacial features (five right panels). The counts show different resurfacing episodes with erosion of craters and subsequent re-cratering. These episodes and processes are reflected in the variable steepness of the distributions on the log–log plots, giving a kinked appearance. The flat parts show erosional effects; the steep parts show re-cratering after erosion episodes. The martian impact crater size–frequency distribution has been fitted to individual segments of the distribution, giving individual crater frequency values for the different episodes; individual absolute ages can be extracted by applying the Hartmann–Neukum chronology. In this way it is possible to extract the evolutionary history of the area under investigation in detail. Here the fits to the crater frequencies partly have the character of average isochrons for a group of counts yielding similar numbers. The errors of the ages are usually around 20–30% for ages younger than 3 Ga (only 100–200 Ma for older ages) owing to statistical limitations. The error bars represent a 1σ error. In the same way, all ages of less than 2 Ga may be affected by a possible systematic error of a factor of about two in the cratering chronology model used. North is at the top.

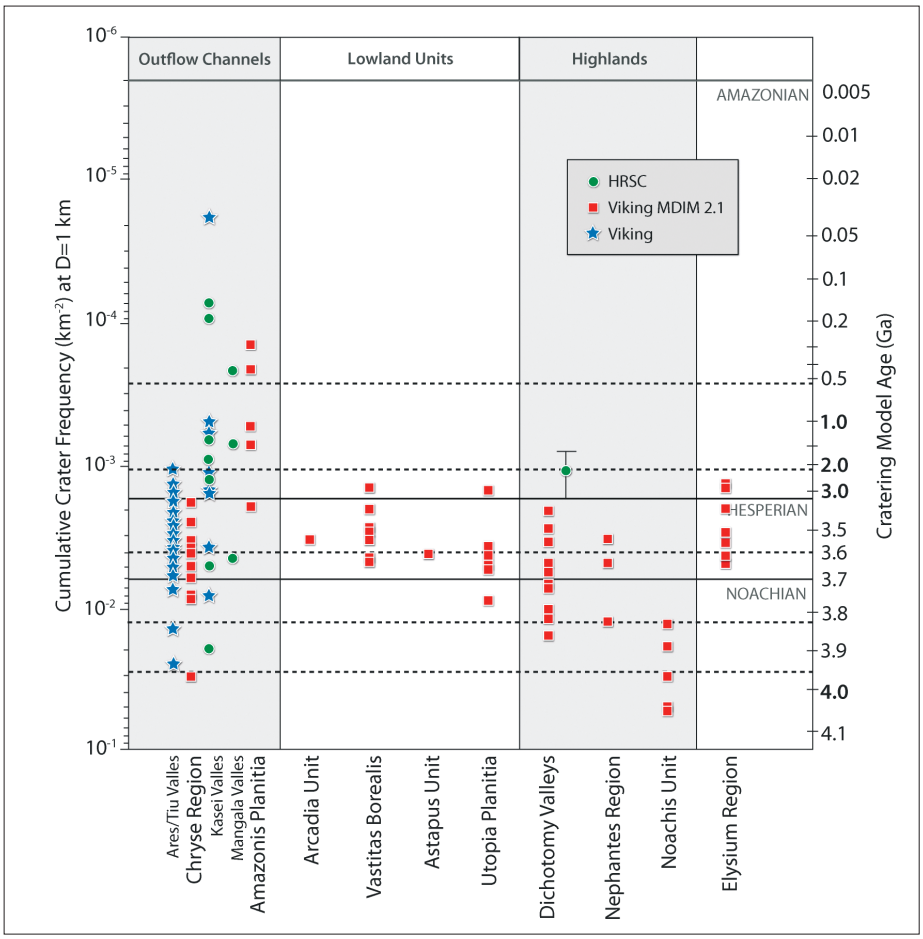

Fig. 25. Ages of ancient fluvial and ice-related processes on Mars. Outflow channel formation ended ~3.5 Ga ago, subsequent volcanic and water/ice-related processes lasted until recently (hundreds of millions of years). Glacial scours in Kasei, for example, formed more than ~1.3 Ga ago. Lowland deposits formed between 3.8 and 3.4 Ga ago. The highland–lowland boundary formed more than 3.8 Ga ago, and subsequent (regressive) erosion is possibly still ongoing. Phases of subsurface ice melt or water release from aquifers triggered by volcanic activity (Mangala Valles) might have occurred 400–700 Ma ago. Sedimentation through fluvial or glacial activity in the northern lowlands ended more than 3 Ga ago at least, probably even more than 3.5 Ga ago. Modified after Werner (2005).

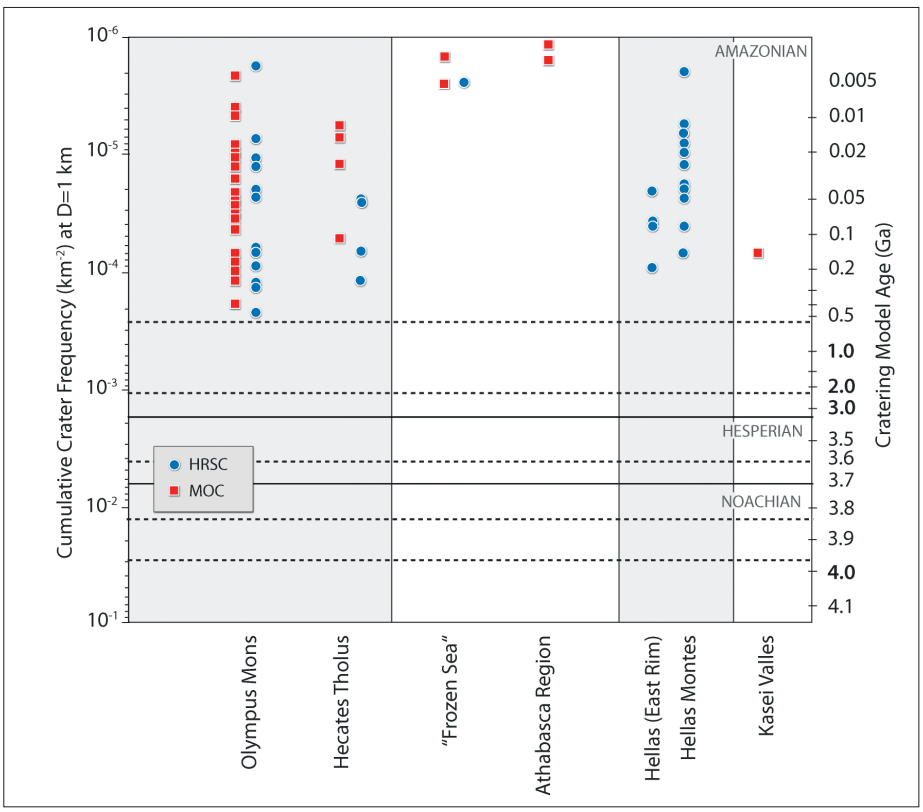

Fig. 26. Ages of ice-related processes on Mars. Landforms in the investigated areas suggest the presence of ice on the surface (under a dust cover) even now. Recent glacial (fluvial) activity is observed in the last 500 Ma, and often seems to have been related to volcanic/magmatic (hydrothermal) activity. This activity may be related to either obliquity changes and/or to changes in the solar flux. Modified after Werner (2005).

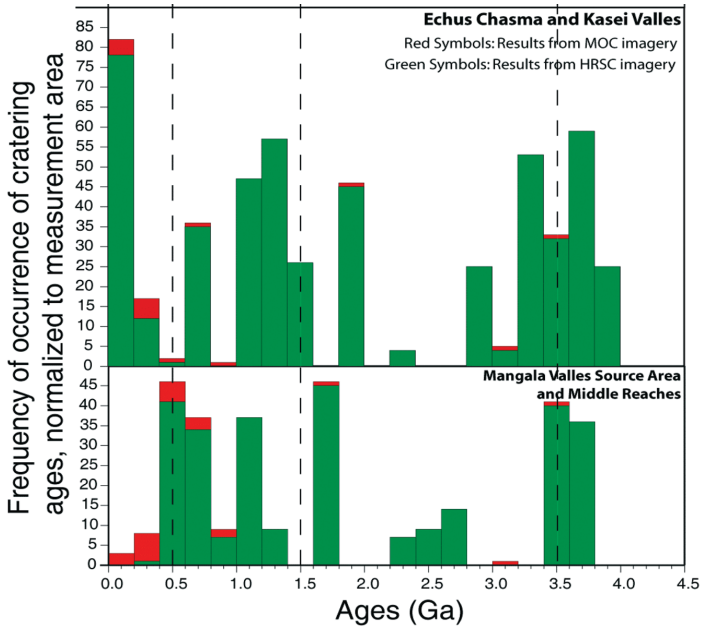

Fig. 27. Histogram of ages extracted from measurements on HRSC (green) and MOC (red) imagery in the Echus Chasma/Kasei Valles and Mangala Valles. HRSC-related values normalised to the size of the counting area.

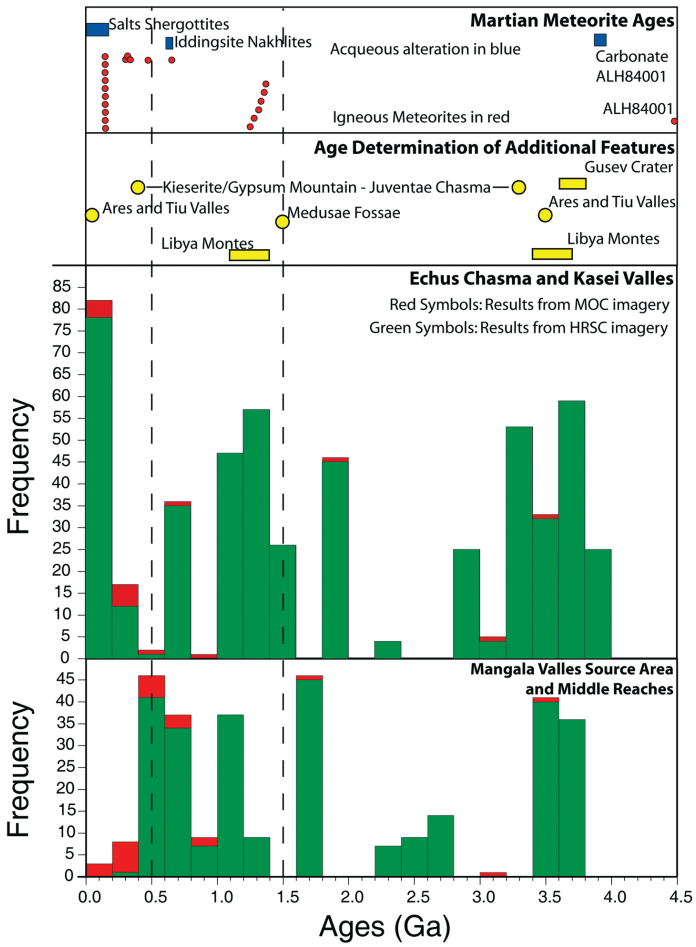

Fig. 28. Histogram of ages extracted from measurements on HRSC and MOC imagery in the Echus Chasma/Kasei Valles and Mangala Valles, combined with cratering age measurements on additional features, in comparison with known radiometric ages of martian meteorites (from Borg & Drake, 2005).

3.3.1.4 Ages of Fluvial and Glacial Activity on Mars

Most of the measurements performed to date on the activity of water and/or glacial processes are compiled in Figs. 25 and 26. It is obvious that water was on the surface in liquid form or as ice throughout much of martian history, starting more than 4 Ga ago and continuing, at least episodically, until a few million years ago.

3.3.1.5 Episodicity of Martian Fluvial, Glacial and Volcanic Activity

The age data in Figs. 22, 25 and 26 show that activity was probably not equally distributed over time but occurred at certain times or time intervals, such as around 3.5 Ga ago. No attempt had been made in those measurements, however, to sharpen the time resolution in terms of specific choice of counting areas or weighting of results. For a better understanding of the geological evolution of Mars, and possibly to verify an episodicity of activity that we suspect but which cannot convincingly be concluded from the general datasets discussed so far, a number of large geological units, in particular the outflow channels Kasei Valles and Mangala Valles, have been carefully mapped and their ages measured (Chapman et al., 2007; Basilevsky et al., 2007). Although this work has not yet been finalised, it is clear from the histograms in Fig. 27 (cf. Neukum et al., 2007) that the evolution of these outflow channels shows relatively strong episodicity.

The dating results for Echus/Kasei and Mangala, together with a number of additional cratering age measurements on geological features all over the martian surface, are compiled in Fig. 28. All the ages from cratering measurements (cf. Neukum et al., 2007; Chapman et al., 2007; Basilevsky et al., 2007) are compared

with the radiometric ages of the martian meteorites (Borg & Drake, 2005). There is a striking appearance of peaking of the geological activity or episodicity of resurfacing at certain times: ~3.5 Ga, 1–1.5 Ga, 300–600 Ma and ~200 Ma ago, respectively. It is even more striking that within relatively narrow limits, the cratering ages of the different age groups coincide with those of martian meteorites. The martian meteorite ages reflect both igneous events and aqueous alteration events, and so do the cratering ages. There is a remarkable paucity of age occurrences in the 2–3 Ga age range in the cratering data. This corresponds to a paucity of meteorite ages in the same, even somewhat more extended age range. This appears to hint at either lower geological activity in this time frame, or, more likely, the covering up of more ancient activity by subsequent events <2 Ga ago, with the exception of the residues from the time >3 Ga ago (the peak at ~3.5 Ga) when the martian surface was thoroughly shaped at a very high level of activity by gigantic volcanic, fluvial, and glacial events that could not be completely erased by later events but most always show up in the cratering data in terms of the large-crater survivors of the tail end of the distributions.

3.3.2 Glacial Processes and Cold-climate Landforms

The current position of ice deposits on the surface of Mars is an indication of the presence of water and its stability in the present environment. For example, the thick polar layered terrain is testimony to the latitude dependence of ice stability, and recent Mars Odyssey GRS/NRS data show the presence of near-surface ice in the regolith down to about 60° latitude.

HRSC image and stereo data of the polar layered deposits (PLD) have been essential in the determination of the three-dimensional configuration of layers in the PLD and in deconvolving the complex layers and unconformities to test various hypotheses for polar history (e.g. Milkovich et al., 2006).

The position of deposits and structures involving water in solid and liquid form in non-polar areas is critical to the understanding of past climates and to unravelling the history of climate change on Mars. For example, the work of Laskar et al. (2004) has shown that variations in spin-axis and orbital parameters were quite large in the history of Mars and thus, polar ice should have been mobilised and transported equator-ward to produce water- and ice-related deposits. HRSC data have provided abundant and clear evidence for such deposits and have helped unravel the history of climate change. Along the dichotomy boundary in the northern mid-latitudes, for example, abundant evidence has been cited in the past of lineated valley fill (LVF) and lobate debris aprons (LDA), but the origins of these deposits have been uncertain. Some felt that movement of material in the LDA and LVF was rather minimal, resulting largely from water vapour diffusion, ice emplacement, and mobilisation of talus aprons. Others have suggested that glacier-like debris-covered ice may have been more important. High-resolution HRSC data have shown that many LDA contain substantial amounts of ice (Head et al., 2005a, 2005b), sufficient to suggest that many LDA are actually the remnants of debris-covered glaciers (Fig. 29a). In other places, LVF deposits have been shown to be integrated systems of flow over many hundreds of kilometres, rather than local talus aprons meeting in the middle of the valley. Analysis of HRSC and Mars Odyssey data have documented the location of ice accumulation zones in alcoves and breached craters, the collection and flow of ice and debris cover, its merging and folding into chevron folds, which are then further compressed and deformed into lines representing the lineated valley fill (e.g. Head et al., 2006a, 2006b).

These analyses strongly suggest that climate change in the last several hundred million years resulted in transport of significant water from the poles to the northern mid-latitudes to produce valley glacial land systems there.

HRSC data were instrumental in the acquisition of the high-resolution imaging, stereo and crater counting necessary to document fundamental changes in climate. HRSC data on mid-latitude volcanoes also provided evidence of climate change. Unusual deposits in a crater at the base of Hecates Tholus (Fig. 29b) have been

shown by HRSC data to be of glacial origin and to date from the relatively recent geological past (Hauber et al., 2005a). Furthermore, the origin of Hesperian-aged valley networks arrayed radially around the flanks of Hecates and Ceraunius Tholus has always been enigmatic, as most valley networks are of Late Noachian age. New HRSC data and modelling of magmatic intrusions within the edifices, however, have led to development of the hypothesis that snowpack developed on the summit of the volcanoes during periods of climate change was then melted by the heat of periodic volcanic intrusions, causing radial drainage to form the valley networks (Fassett and Head, 2006a, 2006b). This explanation helps to account for why some volcanic edifices in this latitude range have no radial channels: these volcanoes may not have been active during the episodic emplacement of summit snowpack.

Striking evidence for even more extreme climate change has been documented by HRSC in the form of important details and ages of tropical mountain glacier deposits. Fan-shaped deposits on the northwestern flanks of the Tharsis Montes and Olympus Mons have long been known, but their interpretation has been varied and controversial. HRSC data, together with MOC and THEMIS data, have shown unequivocally that these deposits represent the remnants of huge tropical mountain glaciers. Images revealed details of the outer ridged facies, interpreted to be cold-based glacial drop moraines; the knobby facies, interpreted to be sublimation till representing the collapse of the huge piedmont glaciers; and the smooth facies, interpreted to be proximal and late-stage debris-covered glaciers (e.g. Head & Marchant, 2003; Neukum et al., 2004a; Head et al., 2005a, 2006c; Milkovich et al., 2006; Shean et al., 2005, 2006). HRSC data have also provided sufficient information for high-quality crater size–frequency distribution analyses (Neukum et al., 2004a; Head et al., 2005a; Shean et al., 2006), showing evidence for glaciation in the last several hundred million years, but also for smaller-scale glacial advances in the last few tens of millions of years (e.g. Neukum et al., 2004a; Head et al., 2005a).

What were the conditions that led to the tropical mountain glaciers? The interpretations from the HRSC and related data provided atmospheric modellers with sufficient constraints to determine that the tropical mountain glaciers formed during periods of high obliquity when water-laden winds from the north rose along the western Tharsis rise, and then rose again sharply at the northwestern margin of the volcanic edifices, causing adiabatic cooling and significant snow precipitation to result in ice accumulation and glaciation (e.g. Forget et al., 2006). Finally, recent dyke emplacement events in the Elysium Planitia region (Cerberus Rupes) have cracked and breached the cryosphere, causing combined volcanic and aqueous outpourings. Evidence for aqueous outpourings comes from hydrodynamically shaped landforms and scour marks, increasingly revealed by HRSC data. Also revealed in the HRSC data are spectacular plate-like features that are separated from each other but fit together like pieces of a puzzle. Previously interpreted as the segmented platy surface of a large lava flow, Murray et al. (2005) used HRSC data to argue that these large plates actually represent 'icebergs' formed on the surface of the floodwaters and preserved below a layer of sublimation till (Fig. 29c).

In summary, HRSC high-resolution image data have revealed the fine-scale geomorphology of water- and ice-related features, and stereo data have provided the 3D data necessary for determining flow directions, stratigraphic relationships, layer orientations and deposit thicknesses. The broad coverage of image data has been essential in determining crater size–frequency distribution ages for these events, all of which have contributed significantly to the analysis of climate change and the past history of climate on Mars.

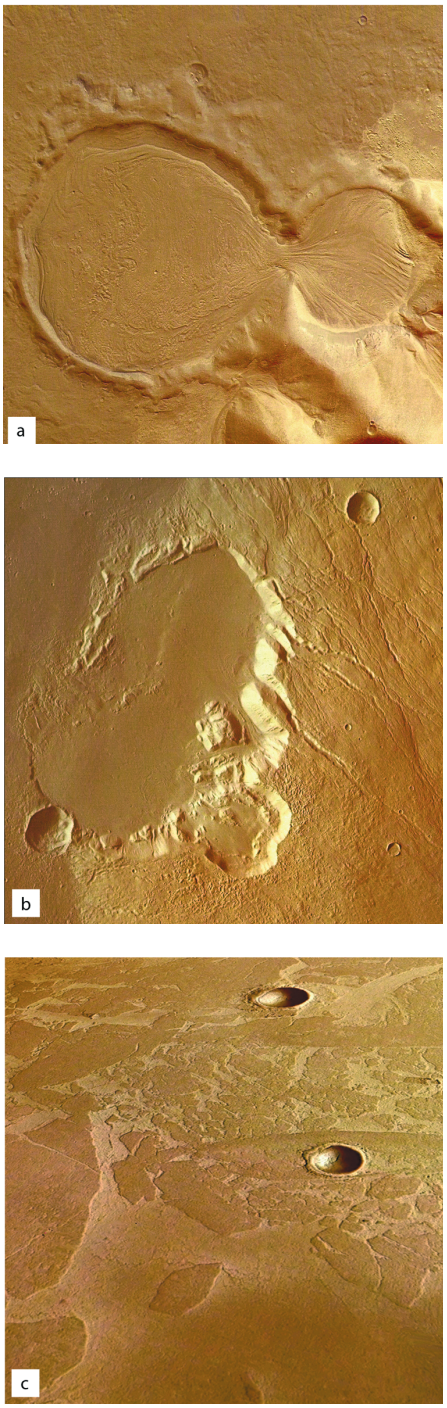

Fig. 29. Ice-related landforms as imaged by HRSC. (a) Debris-covered infill in impact crater (Promethei Terra; Head et al., 2005a); (b) flank caldera showing traces of glaciation (Hecates Tholus; Hauber et al., 2005a); (c) ice floes in Elysium Planitia (Murray et al., 2005).

3.3.3 Sedimentary Processes

Deltaic sedimentary bodies on Mars have been described using Viking data in a few pioneer papers (Grin & Cabrol, 1997; Ori et al., 2000a, 2000b). However, the idea of the presence of complex lacustrine environments (Cabrol et al., 1996; Ori & Mosangini, 1998) has been widely accepted by the scientific community only recently,

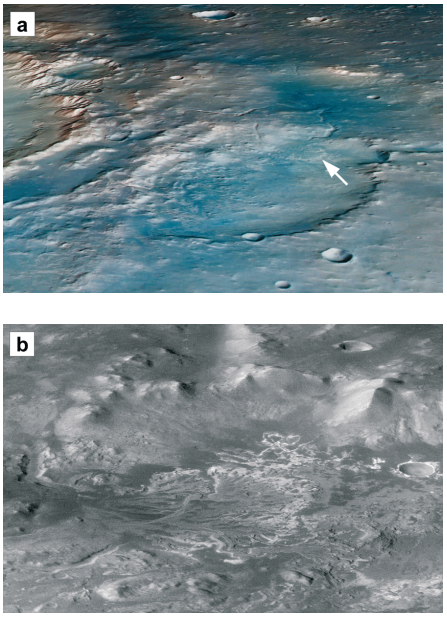

Fig. 30. The delta in the Eberswalde crater (ca. 50 × 70 km). (a) Perspective 3D false-colour view of the Eberswalde delta and the delta (arrow). To the left (=south), the rim of the large Holden crater is visible. Both craters have been proposed as future landing sites due to their spectacular fluvial and lacustrine landforms (HRSC image 511). (b) The delta in Eberswalde crater seen in perspective view from the south. The delta is located at 24.1°S and 326.4°E and has a size of 12 × 12 km (detail of HRSC image 2013).

when data from the new mission have provided other data. The contribution of the HRSC to our understanding the lacustrine sedimentary environments and associated deltas has been remarkable. The high-quality data with stereo capability allow detailed analysis of the sedimentary strata patterns, morphologies and even facies.

It is now clear that deltas exhibit a variety of facies associations, ranging from Gilbert-type deltas to shallow-water fluvial-dominated deltas. Gilbert-type deltas are simple bodies and form when short-headed fluvial systems debouch in a lacustrine basin with a steep margin. Shallow-water deltas are controlled by long fluvial systems and display a large number of distributary channels. The transition from the deltaic plain and the prodelta area is subtle due to the low gradient. Mouth bars are poorly developed. Between these end members there are a number of fan-shaped bodies that in places show distinct evidence of interaction with a standing body of water, but can often be ascribed to alluvial fans due the lack of evidence of a lacustrine environment.

HRSC images in combination with HRSC-based DTM and, at places, MOC narrow-angle images allow us to observe the outcrops with an Earth-like approach and in particular to describe the internal geometry of layered sequences. These observations are particularly important with respect to sedimentary bodies, because these systems display complex internal geometrical patterns. Delta-like deposits, wave-cut terraces, and shorelines are fundamental features to support the hypothesis of standing and long-lived water bodies on Mars. Intra-crater lakes, due to their relatively limited size and their strong climatic coupling, might allow the reconstruction of local hydrological cycles, which could help improve our understanding of the evolution of the martian climate.

Figure 30 presents an example from the Eberswalde fan delta, centred at 24.1°S and 326.4°E, located in one of the richest fluvial-related morphologies areas of Mars (e.g. Malin & Edgett, 2001). The delta is made of bright and dark interlayered deposits, which display a cyclic depositional pattern. The bright layers appear to be more resistant to weathering and erosion. Some of the bright layers consist of very poorly sorted material, with boulders up to 10 m in diameter floating in a finer matrix suggesting an emplacement as mass flows. Other layers consist of finer and better-sorted material. The sedimentary complex displays a low-dipping proximal area (1–2), a distal relatively high-dipping area (6–10) and a more distal low-dipping area (1–2), which gradually connects with the crater floor.

We interpret the low-dipping proximal part as delta plain facies consisting of distributary areas, mostly built by coalescing point bars, and interdistributary area, in which crevasse splays flood into the plain (Pondrelli et al., 2006). At places the topset–foreset–bottomset architecture typical of fan deltas is present, even if the foresets are just slightly inclined. We interpret the high-dipping part of the fan delta as delta front deposits (Pondrelli et al., 2006).

Along an erosional cut, a transgressive–regressive cycle has been observed, with layers at the base showing a retrogradational stacking pattern on top of which clinoforms suggesting a progradational stacking pattern develop forming an offlap surface. We interpret the retrogradational stacking pattern as formed during a transgressive system tract followed by a high stand system tract corresponding to the progradational stacking pattern. The transition among these systems is marked by a maximum flooding surface. This geometry suggests an allogenic control on the deposition.

A survey of the Xanthe Terra cratered terrains revealed several delta-like deposits inside impact craters (Subur, Sabrina, Nanedi and Tyras Vallis) and downstream of a widening of the valley floors (Hypanis Valles) (Di Achille et al., 2006a; Hauber et al., 2005b). In particular, the Tyras palaeolacustrine system, formed by the Tyras Vallis channel and an as yet unnamed Noachian complex crater (70 km in diameter) (Scott & Tanaka, 1986), has been studied in detail using high-resolution topography derived from HRSC stereo data (Di Achille et al., 2006a; Fig. 31a). This supports the recognition of the Tyras fan deposit and its morphometric description, which allows the reconstruction of the overall lacustrine depositional history from the parallel

analysis of the Tyras fan and crater floor deposits. In fact, the delta has been used as a sedimentary recorder of the crater lake history and has allowed the assessment of the overall hydrological evolution. Two major stands of the water level have been inferred at 700 and 550 m above the crater floor, based on the correlation between the morphology and topography of the fan and the crater floor deposits (Di Achille et al., 2006a). The hydrological reconstruction reveals a complex sedimentary evolution of the fan, which underwent deltaic and alluvial sedimentation as a result of the different lake water levels and Tyras Vallis supplies. A second fan-shaped deposit found in the Coprates Catena region, has been also recently investigated using the HRSC data (Di Achille et al., 2006b). Water flowing in a 45 km long sapping valley entered a deep trough and formed a stepped fan with a height of 1100 m above the trough floor and a mean slope of 7.4 (Fig. 31b). The Coprates fan radius ranges from 4900 m up to 8500 m in front of the valley mouth, where the fan slightly overlaps the northern trough wall. The surface of the fan covers an area of about 45 km^2 with a total volume of almost 25 km^3. Detailed topography from HRSC allowed the detection of a longitudinal slope break over the fan (Di Achille et al., 2006b). This characteristic, combined with a sedimentological analysis of the host basin, led to the interpretation of the deposit as an alluvial, sheet-flood dominated deposit. Regional morphotectonics and previous geological mapping suggested that groundwater-related aqueous sedimentation could have been active from Hesperian to Early Amazonian, implying favourable climatic conditions for the flow and possible ponding of water during that period.

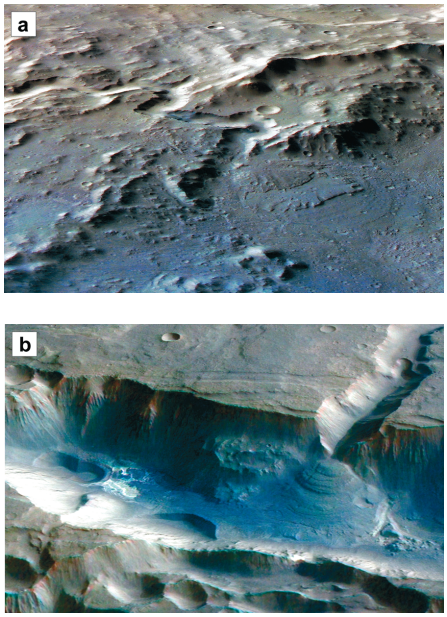

Fig. 31. Examples of sedimentary bodies on Mars. (a) Fan at the termination of Tyras Vallis (Di Achille et al., 2006a). Perspective 3D view of HRSC false-colour image (orbit 927; fan located at 8.5°N, 310.3°E; north is at the top, image width about 25 km). (b) Alluvial deposit at termination of a sapping valley in Coprates Catena (Di Achille et al., 2006b). Perspective 3D view of HRSC false-colour image (orbit 1929; fan located at 15.15°S, 299.75°E; north is to the bottom left; image width about 30 km).

3.3.4 Water-related Activity

High-resolution stereo data of the Mars Express HRSC experiment has allowed for the first time quantitative analyses of small-scale features such as interior channels in martian valley networks and thus estimates of fluvial discharges, sediment transport balances and fluvial erosion rates (Jaumann et al., 2005a).

In HRSC images a 130-km long inner channel has been identified within a 400-km long valley in the Libya Montes. Figure 32 (left) shows a segment of the inner channel incised in a narrow valley at 3°N, 82°E. Based on HRSC stereo information, we were able to determine the depth of this inner structure and thus to estimate the discharge in the inner channel.

With maximum bank-full discharge rates of 10^4 m^3/s (Jaumann et al., 2005a), this channel is comparable with terrestrial rivers like the Mississippi and Amazon. Using the valley depth in connection with the ages of the floor, as derived from crater statistics, an average erosion rate of <1 µm/a is deduced. The development of the valley began 3.7 Ga ago and lasted for 350 Ma. However, it is unclear whether the valley was formed continuously or through isolated flooding events. The eroded valley volume amounts to 460 km^3. Taking the maximum bank-full discharge it would require 4×10^4 days to erode the valley, which would be consistent with a flooding event every few thousand years. On the other hand, if we assume only 5% bank-full discharge, it would take about a million years to erode the valley (Jaumann et al., 2005a). Thus, even with shallow flow, the valley network would have been eroded much faster than is indicated by the average erosion rate. Therefore it is more reasonable to assume that episodic flooding events rather than sustained flow conditions formed the valley network in Libya Montes.

Nanedi Valles in the Xanthe Terra region contains a series of features interpreted to have formed by surface flow of water including meanders, slip-off and undercut slopes (Fig. 33, arrows A, B), terraces and inner channels. The slip-off and undercut slopes that developed in the meanders (Fig. 32) suggest changes that provide evidence of fluvial erosion (Jaumann et al., 2005b). The topographic data of HRSC have allowed us to determine the depth and width of Nanedi Valles and to create a cross-sectional profile of the meander with slip-off and undercut slopes (Fig. 33). The valley in this region is about 500 m deep and 4.5 km wide. The undercut slope can clearly be identified in the profile due to a steeper slope. Several terraces that have developed on the slip-off slope are exposed.

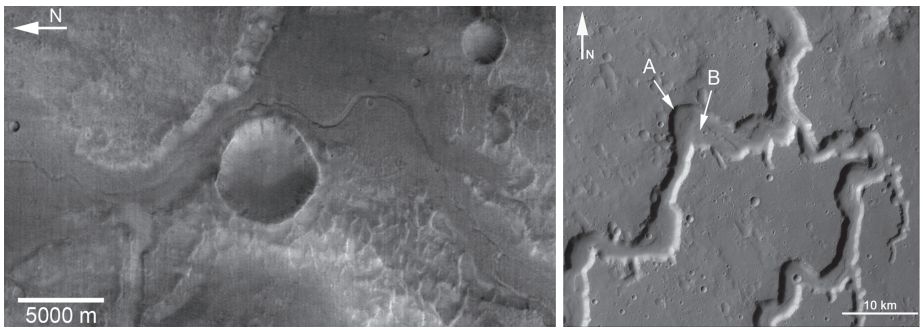

Fig. 32. ***Left:*** **Part of the inner channel in the Libya Montes (orbit 47).** ***Right:*** **Part of the Nanedi Valles in the Xanthe Terra region, at 7°N, 312°E (orbit 905). Slip-off (B) and undercut slopes (A) are marked.**

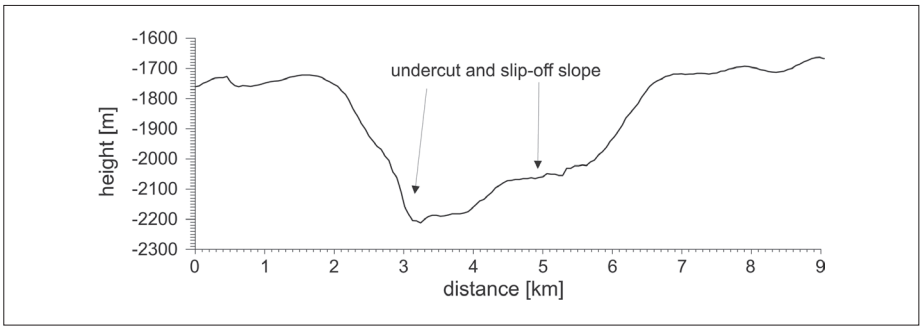

Fig. 33. Cross section profile of Nanedi Valles.

In contrast with these old valley networks, morphologically young gullies suggest that water flowed in geologically recent timescales on Mars (Malin and Edgett, 2000). The analysis of the orientation and distribution of gullies in HRSC imagery have confirmed previous and recent studies using MOC data. They occur most commonly in latitude bands between 30° and 50° in the southern hemisphere (Balme et al., 2006) and between 30° and 60° in the northern hemisphere (Kneissl, 2006). In the southern hemisphere the preferred orientation of gullies is on poleward facing slopes (Balme et al., 2006). Gullies in the northern hemisphere between 30° and 40°N are mainly located on poleward-facing slopes and between 40° and 60°N mainly on equator-facing slopes (Kneissl, 2006). The studies of Balme et al. (2006) and Kneissl (2006), based on HRSC imagery in the northern and southern hemispheres, found strong indications that insolation and atmospheric conditions rather than groundwater are involved in gully formation.

3.3.5 Volcanic Processes

The evolution of the surface of Mars has been strongly influenced by volcanic processes and the emplacement of volcanic materials throughout its history, as first determined from mapping based on Viking Orbiter data (Greeley & Spudis, 1981). Further insight was gained from Thermal Emission Spectrometer (TES) data from the Mars Global Surveyor, which showed the southern cratered highlands to be predominantly basaltic, and the northern lowlands to be mostly basaltic andesite (Bandfield et al., 2000) or weathered basalt (Wyatt & McSween, 2002). HRSC images have been instrumental in determining the chronology of volcanic activity on Mars. For the first time, the wide areal coverage afforded by HRSC taken at consistent high resolutions and illumination conditions allowed the application of crater statistical techniques (i.e. crater counts; e.g. Hartmann & Neukum, 2001) to determine the ages of key volcanic units. The large shield volcanoes of the Tharsis region appear to have formed early in martian history (>3.5 Ga; Werner, 2005) but, surprisingly, HRSC data also showed geologically young (~100–600 Ma old) surfaces on the floors of the calderas and very young lava flows on Olympus Mons (~2 Ma old; Neukum et al.,

2004a; and ≤25–40 Ma old; Basilevsky et al., 2006). These results suggest that the Tharsis volcanoes have periodically erupted within their calderas throughout martian history, and could have the potential for current or future activity.

HRSC images have also enabled regional mapping of the Tharsis shields to determine the styles of flow emplacement and the general evolution of basaltic volcanic systems. Bleacher et al. (2006) mapped a north–south transect across Olympus Mons and found that lava channels rather than tubes dominate the flanks of the volcano at a ratio of 5:1, and that younger channels embay older tubes. These results suggest that late-stage (Amazonian) activity on Olympus Mons changed from longer-lived, stable eruptions to shorter-lived, less stable eruptions, similar to the evolution of Hawaiian volcanoes on Earth.

Hiesinger et al. (2005) mapped Ascreaus Mons to determine the lengths, widths and depths of individual flows as inputs for analytical models to infer lava yield strength, viscosity, and (broadly) magma composition. Their results suggest that the Ascreaus lavas are basaltic to basaltic andesites, consistent with available global spectral information but inconsistent with the compositions measured for the lavas in Gusev crater (McSween et al., 2004). Complete mapping of the Tharsis shield using HRSC data should further elucidate the variations in late-stage volcanism.

HRSC images have also provided insight into volcanism in the Elysium region of Mars. Hauber et al. (2005b), for example, found that part of a large depression on the northwestern base of Hecates Tholus is actually a 10 km diameter caldera formed ~350 Ma ago, consistent with the hypothesis for explosive volcanism on Hecates (Mouginis-Mark et al., 1982). Williams et al. (2005) investigated a sinuous channel on the flank of Hecates Tholus and, using computer modelling constrained by measurements from HRSC data and compositional information on martian basalts from the Mars Exploration Rover *Spirit* (McSween et al., 2004), concluded that erosion by flowing lava could have formed the initial lava channel. The channel appears to have been subsequently enlarged by running water from volcanically induced snowmelt, as suggested by HRSC data (Fassett & Head, 2006a).

3.3.6 Aeolian Processes

Aeolian processes involve the interaction of wind with the surface, resulting in the development of surface features such as sand dunes, wind-eroded hills called yardangs and albedo patterns (called variable features) that appear, disappear or change shape with time as sand and dust are moved by the wind. Active aeolian processes include the formation of dust storms on local, regional and global scales, and the development of atmospheric vortexes called dust devils that inject dust into the atmosphere.

HRSC data have provided new insight into the nature of wind-related features and processes. For example, more than 14 active dust devils were identified on HRSC images, including those seen in Arcadia Planitia, Syrtis Major, Thaumasia Planum, Amazonis Planitia (Stanzel et al., 2006) and most recently in Peneus Patera. Dust devils as large as 654 ± 63 m in diameter and 2956 ± 94 m in height have been found. All of the active dust devils occurred between noon and 15:00 local Mars time, consistent with times of dust devil formation on Earth and as seen on Mars from the rover, *Spirit* (Greeley et al., 2006). Dust devil tracks have also been found on the caldera floor of Arsia Mons and the southern interior slope of the Pavonis Mons caldera. In the case of the Arsia caldera floor, which is at an elevation of 16 km above the reference Mars aeroid, the atmospheric density is very low, and the wind speeds estimated to move dust under boundary layer shear exceed 80 m/s (Greeley & Iversen, 1987), which is far greater than have been measured or predicted for the surface of Mars. Thus, the evidence for dust devils at this altitude shows that vortices are more efficient in lifting fine particles than are boundary layer winds.

The multiple line-scan capability of the HRSC system results in the ability to track rapid time-variable features from orbit for the first time. For example, some of the dust devils described above were ‘captured’ on multiple lines in the same frame; by knowing the scale of the features derived from the altitude of the orbiter and the timing

between HRSC line array exposures, the speeds of the dust devils could be determined. Speeds were found to range from a few to about 25 m/s (Stanzel et al., 2006).

HRSC images enable an assessment of the detection of variable features as a function of imaging wavelength. Such features have been mapped on images from previous missions (primarily the Viking Orbiter) for comparison with predictions of near-surface winds as a function of season. Unfortunately, most of the previous mapping was conducted without regard to the filter through which the images were taken, potentially leading to erroneous correlations. Because HRSC data are taken through four colour filters almost simultaneously, the detection of variable features can be assessed consistently; the results show that most bright variable features (such as wind streaks) are best seen through the red filter.

Future work will involve studies of variable features in selected regions of Mars and analysis of dune fields for which HRSC and compositional data, as from the Omega instrument, are available. This work will allow us to trace potential source regions of the sands in the dune fields as part of the overall analysis of sediment transport pathways on Mars.

3.3.7 Tectonism

The morphology of the martian surface displays clear and unambiguous evidence of tectonic processes (e.g. Carr, 1981; Banerdt et al., 1992). A variety of structural landforms suggests brittle failure of the crust and the lithosphere. The most frequent examples are extensional features (e.g. long and narrow simple grabens, rifts) and contractional features (wrinkle ridges, lobate scarps and fold belts; for a recent review see Mueller & Golombek, 2004). A critical aspect of any study of martian geodynamics based on the analysis of tectonic structures is the determination of the chronology. The relative ages of the features and, therefore, the processes responsible for their formation may be dated by structural mapping and crater counts, while additional information on topography and gravity is required to model loads and to derive stresses in the lithosphere (Golombek & Banerdt, 1999; Anderson et al., 2001). HRSC data were used for the investigation of extensional as well as contractional tectonic features.

On Earth, tectonic (continental) rifts are defined as ‘elongated tectonic depressions associated with which the entire lithosphere has been modified in extension’ (Olsen & Morgan, 1995: 4). Therefore, rifts provide information on significant crustal deformation and associated stress fields. Earlier studies by members of the HRSC team, but still without HRSC data, reported the identification of extensional structures on Mars that can be directly compared in several aspects with their terrestrial analogues, i.e. terrestrial continental rifts (Hauber & Kronberg, 2001, 2005c). The use of HRSC images has improved the situation in that they provide relatively high-resolution data (typically 10–20 m/pixel) over large areas. Such images are ideally suited for crater counting and, therefore, for the age determination of key surface units. Two martian rifts have been investigated with HRSC images so far: the Acheron Fossae and the Coracis Fossae rift systems.

The Acheron Fossae region is an ancient crustal block exposed in the northwestern Tharsis province on Mars. The extensional tectonics along the E–W-trending topographic high of Acheron Fossae is interpreted as a surface expression of upwelling asthenospheric material that initiated regional uplift, crustal extension and breakup, and associated volcanism in the Noachian period (Kronberg et al., 2006). The tectonic architecture and the dimensions of the extensional structures are comparable with those of terrestrial continental rifts (Fig. 34). An area of elevated topography and strong erosion in the eastern Acheron Fossae region is interpreted as a rift-related centre of volcanism. The extension across the Acheron Fossae reaches 1.2–8.7 km, comparable to young continental rifts on Earth. Crater statistics indicate an absolute cratering model age of between ~3.9 and 3.7 Ga for the rifting. The uplift observed on the rift flanks of the Acheron Fossae indicates a fairly thin and thus hot lithosphere. Using flexural analysis, Kronberg et al. (2006) have constrained the elastic lithosphere

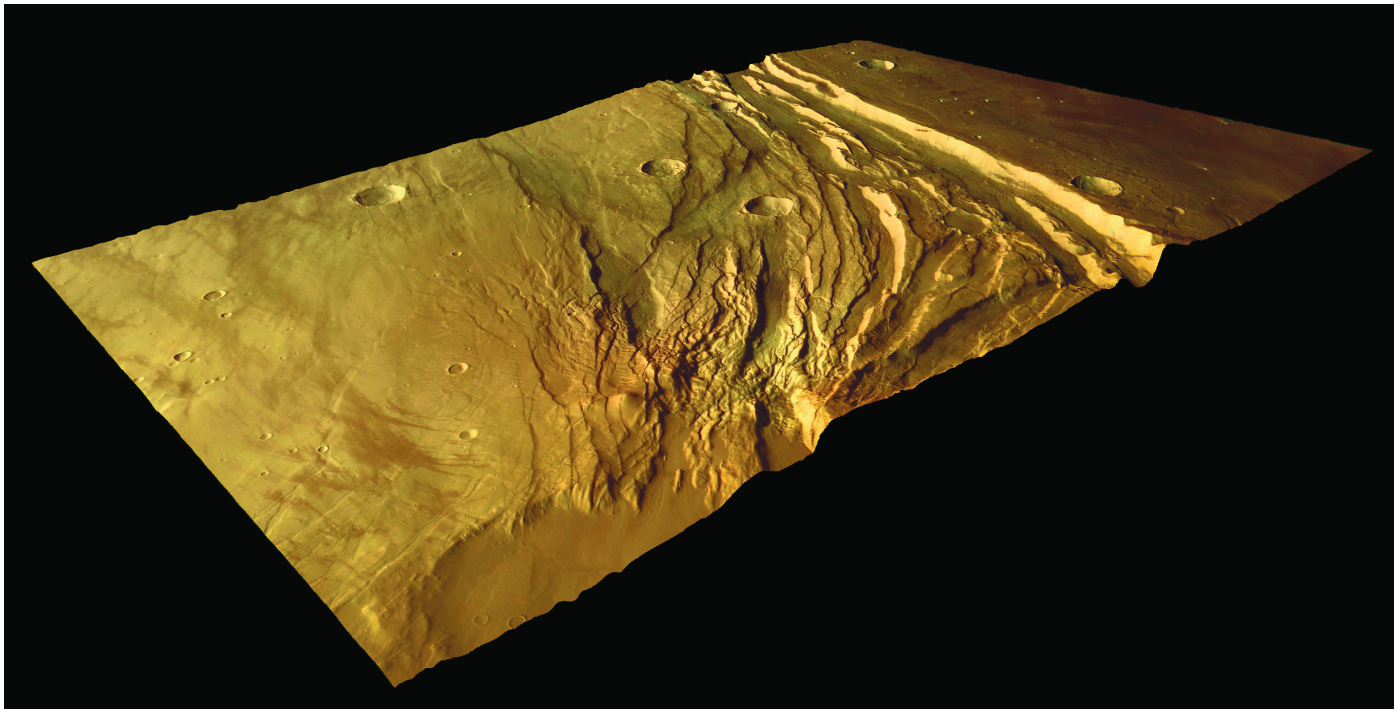

Fig. 34. 3D perspective view of the eastern Acheron Fossae region, based on HRSC colour and stereo data. The area is heavily fractured by extensional faults. The large elevated area in the foreground is interpreted to be a pre- or synrift volcanic region. Two small cones in the middle left foreground may be volcanic edifices.

thickness at the time of rifting to 8.9–11.3 km, corresponding to thermal gradients of between 28 and 41K/km. These heat flows are substantially larger than Noachian heat flow values previously reported, but are consistent with the presence of rift-related volcanism and a magmatically very active environment.

The Coracis Fossae are located in the southern Thaumasia region and cut the Thaumasia highland belt in the NE–SW direction. Their structural architecture is also similar to terrestrial continental rifts. Grott et al. (2005) have identified flexural uplift at the flanks of the central Coracis Fossae rift valley. Modelling the topography, the elastic thickness is constrained to 10.3–12.5 km; the corresponding mechanical thickness and thermal gradient are 15–19 km and 27–33K/km, respectively. These values are similar to those found for the Acheron Fossae region, which are similar in age. The time of rifting of the Coracis Fossae is dated by evaluating the crater size–frequency distribution of key surface units related to the rifting. Thus, the heat flux between 3.5 and 3.9 Ga ago is calculated to be 54–66 mW/m² . Furthermore, the stresses supported by the rift bounding faults are estimated to be below 5 MPa. We speculate that this weakness may be connected to the presence of water below the surface.

Contractional tectonic surface features on Mars include wrinkle ridges and lobate scarps (Mueller & Golombek, 2004). It is possible to gain insight into the state of the early martian lithosphere by modelling the topography above lobate scarps (surface breaking thrust faults). HRSC data and MOLA topography were used to analyse two thrust faults in the southern Thaumasia region (Grott et al., 2006). Crater counts of key surface units associated with the faulting indicate a scarp emplacement in the Late Noachian–Early Hesperian periods between 4.0 and 3.5 Ga. The seismogenic layer thickness at the time of faulting is constrained to 27–35 km and 21–28 km for the two scarps investigated, implying palaeo-geothermal gradients of 12–18 and 15–23K/km, corresponding to heat flows of 24–36 and 30–46 mW/m². The heat flow values obtained by Grott et al. (2006) are considerably lower than those derived from rift flank uplift at the nearby Coracis Fossae for a similar time period, indicating that surface heat flow is a strong function of regional setting. If viewed as representative of magmatically active and inactive regions, the thermal gradients at rifts and scarps

Table 3. Phobos encounters

Orbit	*Encounter times (UTC)*	*Mean anomaly (deg)*	*Flyby distance (km)*
413	2004-05-18T08:34	32.02	1881
649	2004-07-23T12:40	185.11	1834
682	2004-08-01T18:35	178.02	1465
715	2004-08-11T00:30	171.36	1207
748	2004-08-20T06:25	164.77	1239
756	2004-08-22T12:06	169.14	147
1064	2004-11-16T14:21	114.14	4676
1163	2004-12-14T08:05	94.43	3815
1212	2004-12-28T02:52	91.7	1966
1558	2005-04-03T23:50	40.54	3598
1574	2005-04-08T11:20	53.57	3801
1607	2005-04-17T17:15	47.54	3988
1769	2005-06-02T03:40	202.77	1440
1901	2005-07-09T03:25	181.73	3109
2151	2005-09-16T23:24	136.73	3825
2192	2005-09-28T11:02	131.8	2924
2233	2005-10-09T22:29	127.02	2111
2381	2005-11-20T09:06	94.23	3169
2397	2005-11-24T20:38	100.8	1672
2405	2005-11-27T02:15	106.72	1426
2446	2005-12-08T13:44	96.6	2026
2463	2005-12-13T08:03	75.12	4233
2479	2005-12-17T19:26	83.87	2913
2487	2005-12-20T01:15	89.69	2571
2501	2005-12-24T00:50	272.4	4745
2583	2006-01-15T23:49	262.03	4141
2601	2006-01-20T23:07	103.4	5264
2643	2006-02-01T17:26	63.74	4189
2673	2006-02-10T04:40	262.97	2027
2682	2006-02-12T17:32	241.91	5149
2706	2006-02-19T10:24	256.23	2179
2739	2006-02-28T16:24	250.2	1783
2747	2006-03-02T22:04	252.95	1050
2756	2006-03-05T11:05	236.23	4168
2780	2006-03-12T04:03	246.45	606
2805	2006-03-19T04:19	238.99	1955
2813	2006-03-21T09:58	239.68	832
2846	2006-03-30T15:54	233.92	1328
2854	2006-04-01T21:30	237.83	973
2912	2006-04-18T03:46	223.28	2394
2979	2006-05-06T23:15	211.97	5092
3005	2006-05-13T23:41	208.94	5305
3245	2006-07-20T06:16	150.96	4942
3310	2006-08-07T10:50	161.7	606

span the range of admissible global mean values. This implies dT/dz = 17–32K/km, with the true value probably being closer to the lower bound.

3.4 Phobos

3.4.1 Observation Opportunities

The Mars Express spacecraft is in a unique elliptic (apoapsis: 13 560 km) near-polar (86.6°) orbit and occasionally approaches the small satellite Phobos in its near-equatorial, near-circular (9515 km) path about Mars. By 1 November 2006, 44 individual flyby manoeuvres had been executed (see Table 3 for an overview), and Phobos could be observed from ranges between 5000 km and as close as 150 km (see Fig. 35 for a sample image). Images of the smaller satellite Deimos were also obtained from large distances (>10 000 km), but they show little surface detail. Some of the images reveal areas of Phobos at unmatched resolution levels. In addition, the shadow of Phobos as it moved across the surface of Mars was captured on 11 HRSC images in six different orbits (Fig. 35). The HRSC and SRC data from the satellite encounters have been used for astrometric measurements of the satellite position, for topographic modelling of Phobos, as well as for initial geological analyses.

3.4.2 Phobos Orbit

3.4.2.1 Direct observations

During a flyby, the camera is pointed at some fixed (inertial) position in the celestial sphere, solely controlled by the on reaction wheels. Typically, a few stars are captured in dedicated long-exposure (SRC) images, taken immediately before and after the flyby sequences for pointing control. An SRC imaging sequence is executed as the target crosses the field of view (Fig. 35). Among a typical set of seven images, only two to four images would show Phobos or parts thereof. HRSC is operated through the flyby, and Phobos is usually caught in all nine channels of HRSC. Using limb-fitting techniques, Phobos position (centre of figure) data were obtained with an estimated accuracy of 0.5–5 km (Oberst et al., 2006). These measurement results differ substantially, by about 5–10 km, from the various available Phobos orbit predictions, and have motivated work on new Phobos orbit models (Lainey et al., 2005), as orbit models of this satellite deep in the gravity field of Mars have a strong bearing on tidal dissipation and the internal structure of Mars, possibly even on the higher-order terms of the Phobos gravity field.

3.4.2.2 Phobos shadow

The shadow observations by HRSC are used as an independent check on the Phobos orbit models, as locations of the shadow with respect to Mars surface surroundings are not affected by uncertainties in spacecraft trajectory and pointing data. The position of the shadow of Phobos could be determined with an accuracy of ±0.81 km and ±0.4 km in the east–west and north–south directions, respectively (Fig. 35). Image acquisition times on the ground (noting the high speed of Phobos' shadow of ~2 km/s) could be estimated to within ±250 ms. Comparisons of shadow observations with the new model by Lainey et al. (2005) show a remaining discrepancy of 1.6–7 km (average 3.4 km), with Phobos being ahead of the predicted position. Across-track offsets between 0.6 and 10.6 km (average 5.6 km) were also observed, with the shadow being further south than predicted. These data attest to the improved orbit models, although agreement between predictions and observations may still be improved.

3.4.3 Phobos Shape and Topography

The Viking orbiters have provided hundreds of images of Phobos with resolutions of 200 m per pixel on average, some better. Previous shape modelling efforts of Phobos used a combination of data from limbs, terminators and control points (Simonelli et al., 1993; Thomas, 1993). However, the effective spatial resolution of the model of ~4°, or ~760 m at the Phobos equator, remained limited. During the flyby in orbit 756, HRSC obtained images of Phobos at resolutions down to 7 m/pixel, showing an area

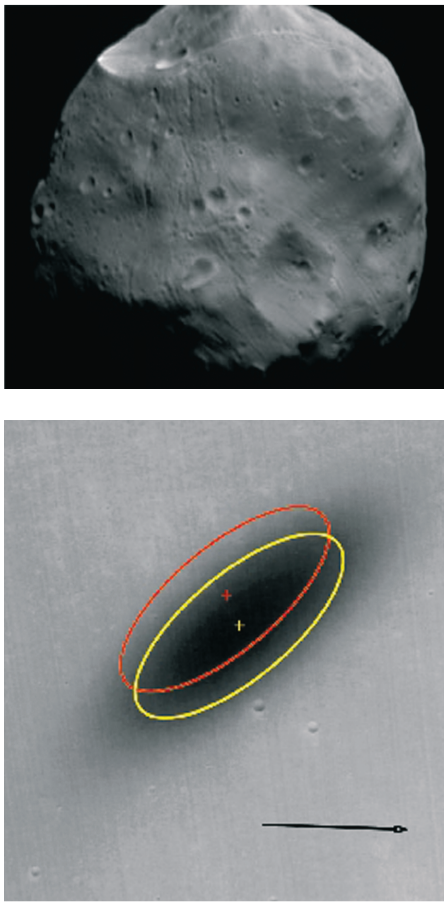

Fig. 35. Phobos (13.3 × 11.1 × 9.3 km), captured by SRC during orbit 2151 (16 September 2006), from a range of 3800 km (left) and its shadow, captured by HRSC during orbit 2345 (11 November 2005, right). The yellow ellipse marks the best fit to the observations; the position of the red ellipse has been computed on the basis of the Phobos orbit model by (Lainey et al., 2005). The arrow shows the direction of motion of the shadow.

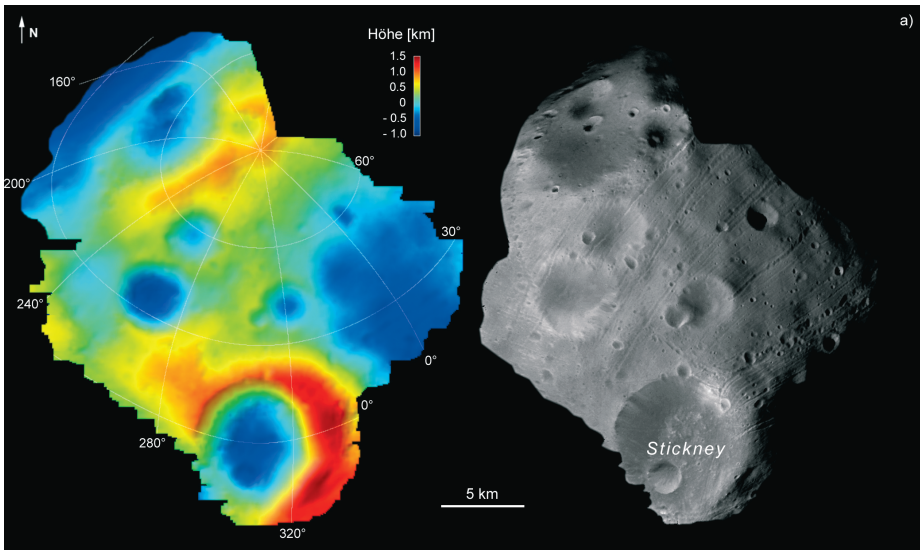

Fig. 36. ***Left:*** **Colour-coded elevation model of Phobos derived from HRSC stereo images taken during orbit 756. The reference surface for elevations is a tri-axial ellipsoid. There has been fivefold stereo coverage of most parts of the modelled area, and a vertical resolution of ~6 m has been achieved. Near Stickney, the resolution is 12–24 m.** ***Right:*** **Orthoimage mosaic derived from the image data and the elevation model.**

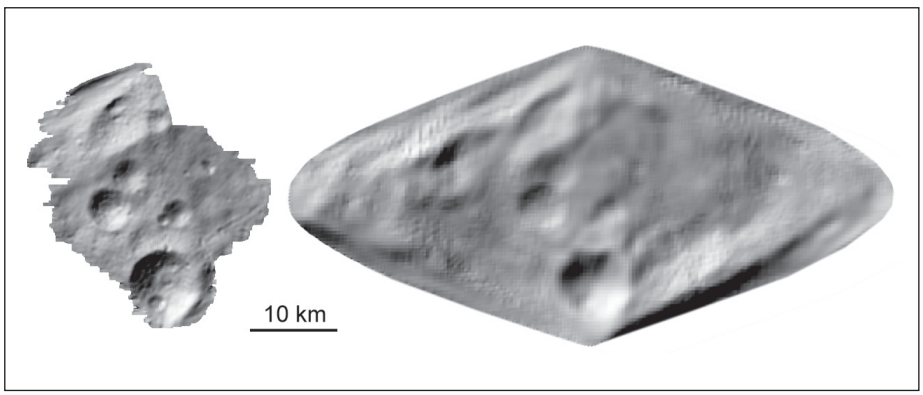

Fig. 37. Shaded relief maps of Phobos derived from Mars Express images (*left*) and the Viking-based numerical shape model (*right*) (Giese et al., 2005). Numerical shape model data copied from *www.psi.edu/pds/archive/astdata/SHAPE/m1phobos.tab*.

north and west of Stickney, the largest crater (9 km) on Phobos. Using the stereo capability of the camera these images allowed us to derive a digital elevation model with effective resolutions of 100–200 m (Giese et al., 2005) (Fig. 36). Although the HRSC model is limited in coverage, it has a higher resolution than the earlier Viking model (Fig. 37). Surface morphological features, notably craters, can now be studied in much greater detail.

3.4.4 Morphology

Based on the terrain model and taking into account the relative positions of Phobos, the Sun and the spacecraft, a map of the solar elevation over the local horizon has been computed. Analysis of images, DTM and the solar elevation map in combination show that the geometry of relatively large (2–9 km in diameter) craters of Phobos is rather similar to that of lunar craters of that size, including bowl-shaped craters with elevated rims, inner slopes locally reaching 25–35°, and depth/diameter ratios reaching 1/5 to 1/4 for the most prominent forms (Fig. 38). This suggests that the impact cratering process on the Phobos surface with very small surface gravity (0.3–0.6 cm/s^2) is generally similar to that on the Moon and the larger planets. Studies of the subpopulation of the smaller craters (100–1000 m in diameter) in comparison with the larger craters show that the percentage of prominent forms is significantly lower. This implies longer survival times against erosion for larger craters, an effect that is also typical for sub-kilometre impact craters on the Moon (Basilevsky, 1976).

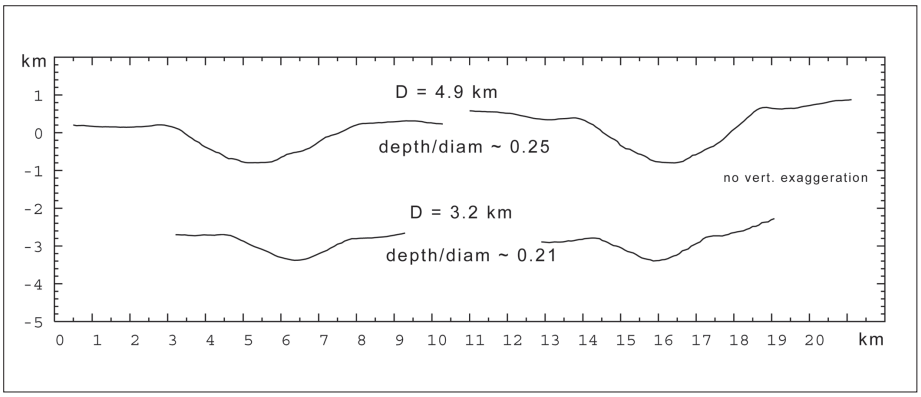

Fig. 38. Profiles across craters of Phobos, showing a characteristic bowl-shape, similar to what is seen on the Moon and other planets.

3.4.5 Future Observations

More Phobos flybys and shadow observations are planned during the Mars Express extended mission. These new observations will further improve the Phobos ephemeris to accuracy levels of better than 5% of the size of Phobos. Furthermore, the added observations by both cameras, HRSC and SRC, will allow us to update the current shape and topography models of Phobos and will give us more insight for further morphological studies.

3.5 Atmospheric Sciences

Although HRSC has been designed primarily to study the surface of Mars, it can also be successfully used to collect data on atmospheric phenomena, including clouds, fogs, hazes and dust storms. Also of interest are surface variable phenomena such as dust devils and frosts. In this section we describe several examples of how HRSC has been used so far to address this aspect of martian science.

3.5.1 Dust Devils

One advantage of the stereo channels of HRSC is the feasibility to detect the motion of atmospheric features such as dust devils. A sample of HRSC images showing dust devils in Thaumasia Planum, south of Valles Marineris (southern hemisphere) is shown in Fig. 39. The solar longitude L_s was 118°, corresponding to southern winter. The five dust devils of different sizes are all oriented in a row. The vortices can be identified for four dust devils (dust devils 1, 2, 4 and 5), two of which (2 and 4) are quite large. One dust devil (3) looks like a large dust cloud where no vortex can be seen. Four dust devils (2–5) were detected in all stereo images (forward-looking channel, nadir and backward-looking channel), and one (1) only in the nadir and backward-looking image because it is out of the field of view of the forward-looking channel. The velocities of the dust devils were calculated between their positions seen in the three images. The forward-looking image was taken nearly 44 s before the nadir, and the backward-looking image nearly 53 s after the nadir. It is usually assumed that dust devils move with the ambient wind (Sinclair, 1969). The fact that the observed dust devils had the same direction of motion and moved approximately the same distance in the same time seems to confirm this assumption. In another orbit (37) three dust devils were found in the nadir channel. Three additional dust devils were found only in the backward-looking stereo image. These additional vortices must have developed in the two minutes between the imaging of the nadir and stereo images, which may indicate that dust devils develop and decay extremely rapidly and are very short, transient atmospheric features.

The forward velocities of the observed dust devils range from 9.4 to 24.3 m/s (Table 4). They move much faster than was expected for dust devils on Mars (Ryan & Lucich, 1983; Metzger et al., 1999; Renn et al., 2000; Ferri et al., 2003), in

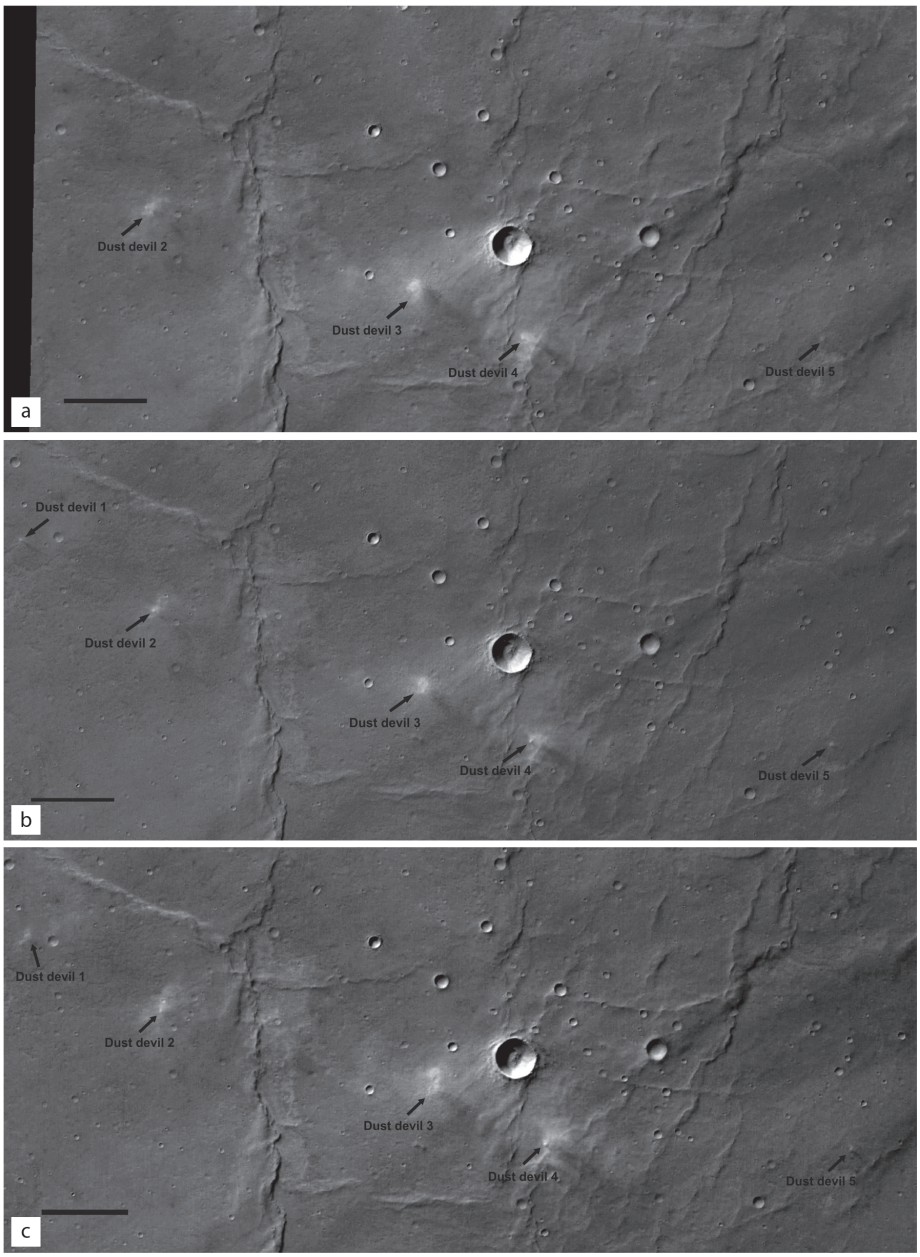

Fig. 39. (a) HRSC stereo 1 forward-looking channel image (orbit 1081) showing five dust devils in Thaumasia Planum. The different sizes of the dust devils and the differences between vortex (very bright spot) and plume (dust devil 4) can be seen. The illumination is from the upper left. North is at the top of the image. (b) HRSC nadir channel showing the changes in position of the dust devils after 44 s. (c) HRSC stereo 2 backward-looking channel showing the changes in position of the dust devils after 53 s after the nadir image (97 s after stereo 1 image). The image extends from 22.6° to 23.3°S, and from 296.6° to 298.2°E. The scale bar represents 8 km.

comparison with measurements and observations on Earth (Sinclair, 1969; Snow & McClelland, 1990). On Earth it is assumed that that dust devil activity is suppressed by wind speeds above a certain value (Sinclair, 1969). The highest dust devil activity on Earth has been observed at wind speeds of 0.5–4.5 m/s; only two dust devils have been observed moving at speeds greater than 9 m/s. There is, however, much less data taken for atmospheric conditions with higher ambient wind speeds. Data obtained by Snow & McClelland (1990) show average dust devil speeds of around 4 m/s when the maximum ambient wind speed was 10.5 m/s; they concluded that speed values greater than 11 m/s are due to measurement errors.

We estimated the error in the recorded positions of dust devils to be 5 pixels (62.5 m in nadir image). The effect of this error on forward velocity is shown in Table 4. We believe that these errors are not of the same kind as the time and range errors made in measurements on Earth, where dust devils are observed in almost

Table 4. Dust devil forward velocities derived from images obtained in orbits 37 and 1081.

		S1-ND (m/s)	*ND-S2 (m/s)*
Orbit 37	Dust devil 1		23.1 ± 1.0
	Dust devil 2		24.3 ± 1.0
	Dust devil 3		25.3 ± 0.9
Orbit 1081	Dust devil 1		9.4 ± 2.4
	Dust devil 2	13.0 ± 2.9	17.2 ± 2.4
	Dust devil 3	21.6 ± 2.9	14.8 ± 2.4
	Dust devil 4	15.2 ± 2.8	15.9 ± 2.4
	Dust devil 5	12.9 ± 2.8	15.2 ± 2.3

horizontal view only (Snow & McClelland, 1990), and estimates of the size, height and distance travelled have to be made in a relatively short time. Here, we have three images and three clear positions of dust devils on Mars, so that the calculations of their velocities across the surface should be more accurate than the determinations of dust devil forward velocities on Earth.

Toigo et al. (2003) simulated the evolution and development of martian dust devils taking into account the background horizontal wind speed. Two dust devils developed in the highest and in the no-wind speed case. Although their study is based on limited data, they suggest that dust devil development is not necessarily connected to background wind speed, but to the convergence of environmental vertical vorticity. The simulated dust devils can be considered as rotating, free-convective plumes.

We can interpret the relatively high forward velocities in two ways. First, assuming that dust devils move with the ambient wind would suggest that this wind speed is much faster than the usually assumed 5 m/s. The analyses of Sinclair (1969), Snow & McClelland (1990) and Toigo et al. (2003) show that dust devil occurrence is also possible at higher ambient wind speeds (>10 m/s) and thus a higher forward velocity is possible. Second, if the ambient wind speed is indeed only a few m/s, then there must be a component in dust devil motion that leads not only to a high rotational and vertical velocity (within the dust devil), but also to a strong forward velocity. Nevertheless dust devils seem to move in the direction of the ambient wind even if they travel at lower velocity than the ambient wind speed (Sinclair, 1969). All dust devils in orbit 1081 moved in approximately the same direction, but the prevailing wind direction could not be determined because of the lack of crater streaks.

3.5.2 Limb Images

To date, HRSC has taken many limb images, several examples of which are shown in Fig. 40. These three colour images, together with *I*/*F* profiles perpendicular to the limb show a rich vertical structure in the martian atmosphere. The signal detected by the camera is the light scattered by the martian aerosols.

The visible structure can hence be deconvolved for the vertical dependence of the aerosols with respect to their size distribution, number density and optical properties. This is not a trivial problem, however, and is subject of ongoing research. The synergy with OMEGA and SPICAM is proving to be very important here. Figure 41 shows an example of a SRC image of the limb. It is clear that the layers seen in the other HRSC channels (Fig. 40) are further subdivided by finer shear layers. Shear layers of this type are commonly observed in Earth's atmosphere. The approximate width of the HRSC images in Fig. 40 is about 200 km, while the width of the SRC frame in Fig. 41 is about 7.5 km.

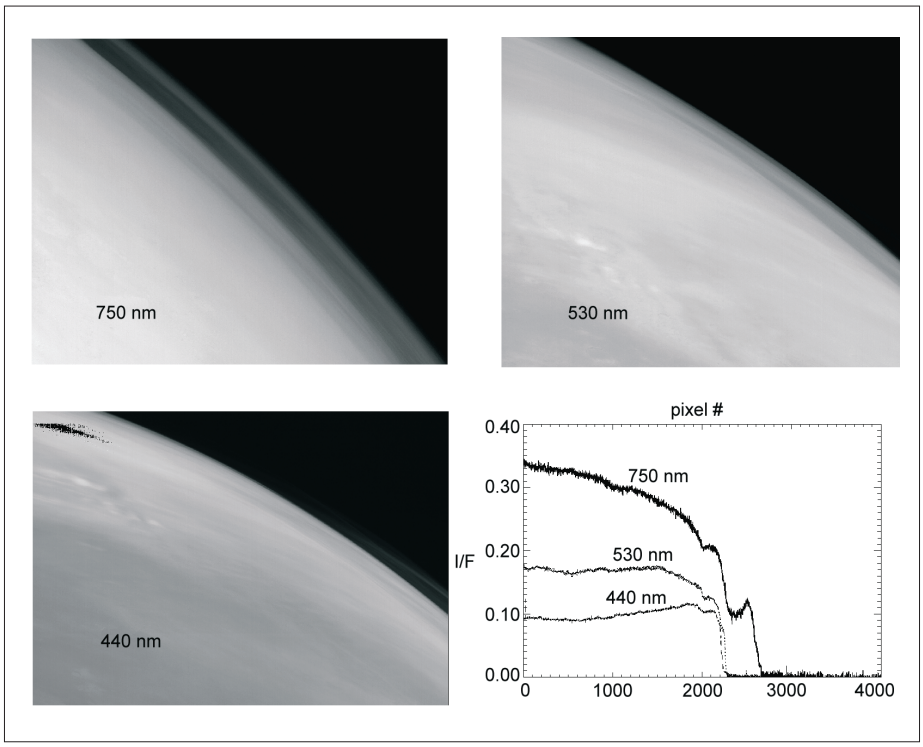

Fig. 40. Limb images in three wavelengths and *I/F* profiles through the limb. Limb position is approximately at pixel number 2000. The detached haze can be seen in the 750 nm image and in the corresponding profile between pixels 2300 and 2500. The width of the images at the limb is approximately 200 km. The black dots in the 440 nm image are due to saturation.

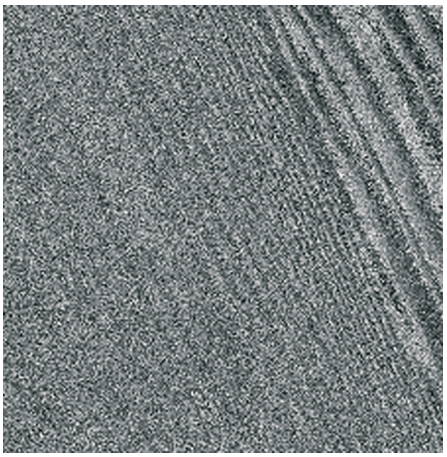

Fig. 41. SRC image of section of the martian limb. The width of the image is approximately 7.5 km.

3.5.3 Lee Wave Clouds

Lee wave clouds are a well known phenomenon in Earth's atmosphere. Usually they show up as large and dense clouds that hover near and over the tops of the mountains. They can prevail for long periods of time, and, even if there are very strong winds, they are usually almost stationary. Lee wave clouds are formed by vertical deflection of winds on a topographic obstacle; the air is forced to oscillate in the lee of the obstacle. In the crest of the wave air rises up to the cooler region where condensation occurs due to adiabatic cooling. In this way a regular train of elongated clouds often forms, aligned orthogonal to the prevailing wind.

Martian clouds have been the subject of scientific interest for a long time. The understanding of their appearance, distribution and behaviour is closely related to the understanding of the martian water, dust and CO_2 cycles. Since lee wave clouds in the martian atmosphere are smaller than a few kilometres, and thus too small to be visible with ground-based observatories, they were observed for the first time by Mariner 9 in 1971. The HRSC on Mars Express has the advantage of combining high enough resolution to detect rather small-scale lee wave phenomena with a relatively wide field of view. This usually allows observation of the lee wave cloud and the obstacle on which it is formed within the same image. From the beginning of the Mars Express mission the HRSC has detected different types of cloud in the martian atmosphere, including many lee wave clouds in equatorial regions and also over the northern polar cap. To date 23 lee wave clouds have been imaged with HRSC in different locations and during different seasons. Lee waves are frequently observed in the northern hemisphere during the local summer, and toward the polar region in autumn, where they are often superimposed on haze and streak clouds. Of all the lee wave clouds observed so far, only one has been in the southern hemisphere.

One of first works to describe the physics of the lee waves was that of Lyra (1940). The advantage of Lyra's formulation is that it gives a simple connection between the wavelength of produced lee wave and the horizontal wind speed. This means that we can estimate the wind speed directly from images of lee waves. An HRSC image taken

Table 5. Coordinates and properties of the 23 lee wave clouds observed on Mars.

No.	Orbit	Latitude (°N)	Longitude (°E)	L_S (°)	Wavelength (km)	Wind speed (m/s)
1	18	50	324	333		
2	68	43.00	256.5	342.2	17.59	25.2
3	533	–36.01	323.27	50.00	3.8	5.52
4	719			72.8	17.10	24.5
5	751			76.6	20	30.9
6	1096	79.98	256.5	119.7	15.2	
7	1107	24.07	262.8	121.2	5.6	7.86
8	1158	39.5	290.7	128.24	5.5	7.72
9	1169	33.8	289.9	129.7	1.41	1.98
10	1210	15.6	221.5	135.28	na	na
11	1235	26.74	283.99	138.71	na	na
12	1262	26.39	148.66	142.47	na	na
13	1266	64.16	114.51	143.03	20.58	28.9
14	1395	64.8	30.8	161.6	13.5	18.99
15	1483	59.44	22.46	175.07	28.22	39.64
16	1487	75.02	339.87	175.69		
17	1500	50.1	150.8	177.73	na	na
18	1521	76.0	238.0	181.03		
19	1523	69	43	181.35		
20	1533	66.4	144	182.94		
21	1546	49.2	308.7	193.12		
22	1603	54.77	103.95	194.27		
23	1636	47.62	99.49	199.73		

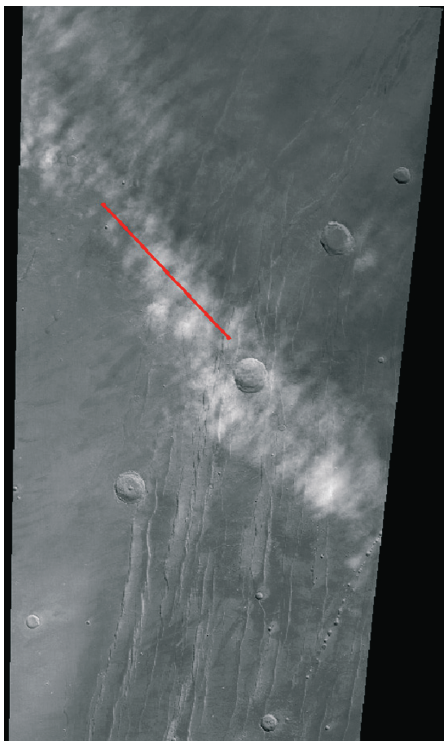

Fig. 42. HRSC image of a lee wave cloud taken during orbit 68.

during orbit 68 (Fig. 42) shows a lee cloud smeared by the motion of the atmosphere. The position of the image is 43°N, 256°E. Unfortunately, the mountain over which this lee wave was formed is outside the image frame. The lee wave structure is distinct enough however, to measure its wavelength. The red line in Fig. 42 marks the points chosen for the *I*/*F* plot shown in Fig. 43. This cut is made perpendicular to the regular train of clouds that mark the crest of a lee wave cloud. The black curve represents the raw data. One can see that periodical lee wave structure is most prominent in the middle part as three pronounced crests. These raw data points were filtered with the low-pass filter (Fig. 43) to remove the high-frequency part of the signal and to make the wave structure more distinguishable. The results are plotted as the red curve. The wavelength value for this lee wave cloud is 17.59 km, from which we can estimate the speed of the wind producing it to be 25.2 m/s. Wind speeds were calculated with this procedure for other lee wave clouds observed with HRSC. The positions of the observed lee wave clouds, times of observation, wavelengths of the lee wave patterns and corresponding wind speeds, are shown in Table 5.

HRSC stereo imaging is performed using nadir-directed, forward-looking (+18.9°), and aft-looking (–18.9°) line sensors. They are used for the extraction of 3D data, which result finally in a digital terrain model. The same procedure could theoretically be used to infer the heights of clouds. The heights of cloud formation, i.e. the condensation level in the atmosphere, are of great interest in atmospheric

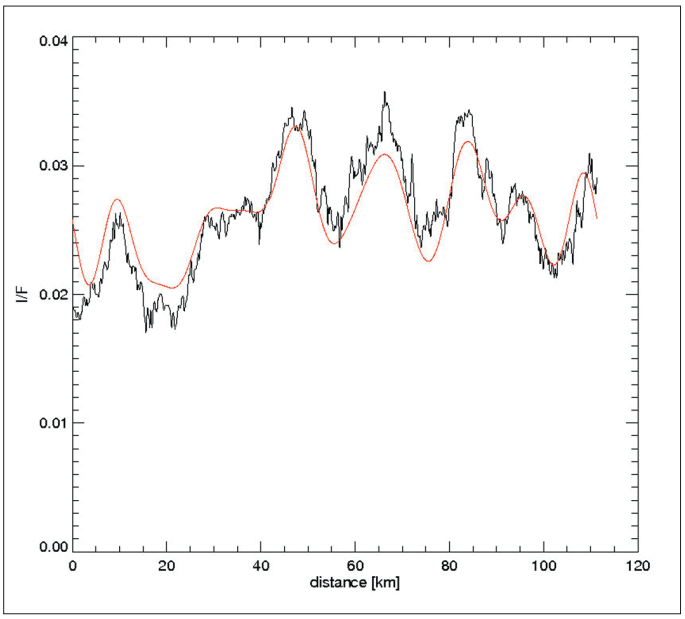

Fig. 43. *I/F* profile along the red line in Fig. 42. Raw data points are shown in black. Red curve: data filtered with the low-pass filter.

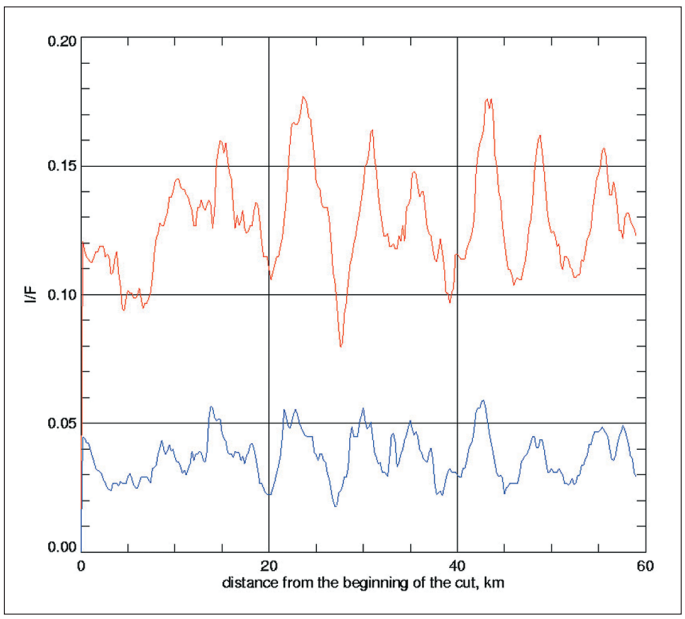

Fig. 45. *I/F* plot of the cut across lee wave cloud shown in HRSC image 1096 in Fig.44. Red and blue curves: data from the red and blue channel images, respectively.

Fig. 44. Image from orbit 1096 showing a lee wave cloud formed over the edge of the north polar cap.

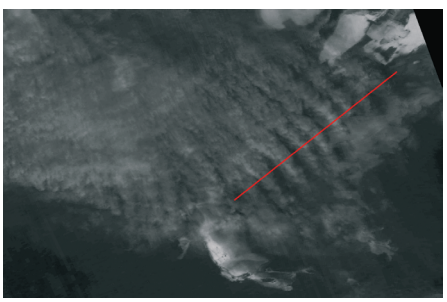

studies and are important for understanding atmospheric circulation. However, measuring cloud altitudes with HRSC is complicated by the fact that clouds do not have sharp boundaries, so that differences in their positions in the stereo channels can not be defined with sufficient precision. In addition, in the time that passes between forward- and backward-looking stereo channel images the cloud changes its absolute position. Nevertheless, lee wave clouds have several physical properties that enable us to measure their heights using the stereo facilities of HRSC. First, a lee wave cloud is a steady phenomenon: the area where condensation occurs remains at the same geographical position while the air moves over the obstacle. Thus the cloud stays at the same absolute position when observed in the forward- and backward-looking channels of HRSC despite the time delay between the channels. Second, lee wave clouds form in the relatively thin atmospheric layer: warm, wet air is brought up from the lower layer to the cold, dry area where condensation immediately begins. Third, a train of lee wave clouds can be used to calculate statistically the shift between the positions of the clouds on two images taken at different angles of incidence, thus reducing the error that is caused by poorly defined cloud boundaries.

The HRSC red channel image from orbit 1096 (Fig. 44) shows a lee wave cloud formed over the edge of the north polar cap. We have chosen this thick cloud for its pronounced wave pattern that allows calculation of cloud altitude. The position of the cloud is 79°N, 256°E. The lee wave in this image has a wavelength of 15.2 km, which corresponds to the source wind speed of 21.4 m/s. The red line in Fig. 44 marks the points chosen for the *I*/*F* plot, which is shown with the red curve in Fig. 45. The blue curve is the *I*/*F* plot for the same geographical position, but from data taken by the HRSC blue channel. From correlation of the two curves in Fig. 45, and using simple geometry, we calculate the cloud altitude to be 4.5 km over the reference ellipsoid used for calculating coordinates. The same procedure was repeated for two other channel combinations: from a combination of two photometric channels we obtain a cloud altitude of 4.4 km, and from two stereo channels, 4.1 km. In polar areas, the real surface lies below the reference ellipsoid: in this particular location it is 15 km lower. The cloud height calculated relative to the real surface is therefore about 20 km.

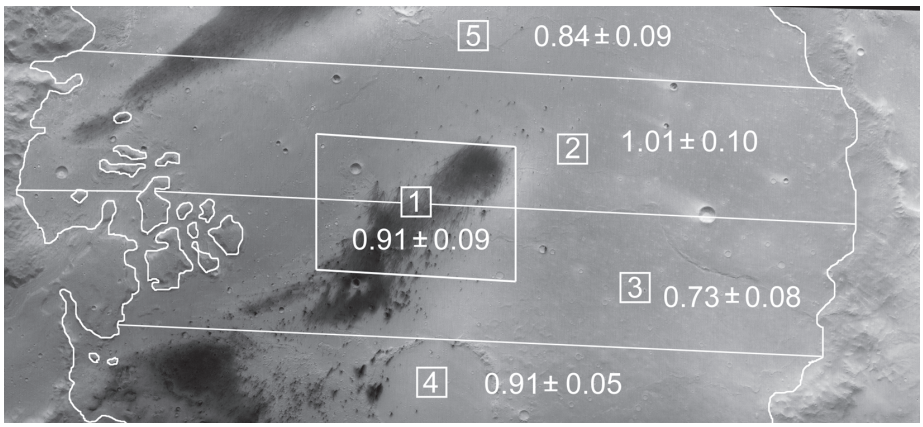

Fig. 46. Gusev crater as observed during orbit 24. Regions 2–5 together cover most of the floor of the crater. The smaller region 1 is centred on the landing site of the *Spirit* rover. For each region, the optical depth as retrieved with the stereo method is given. *Spirit* measured an optical depth of 0.88 ± 0.01 near the moment when HRSC imaged the crater. There is good agreement between *Spirit's* 'ground-truth' and the stereo method retrievals.

3.5.3 Optical Depth of the Atmosphere

The remote sensing of the martian surface from HRSC images is complicated by strong scattering of the solar radiation by aerosols in the atmosphere. Airborne dust and other aerosols strongly change the observed colour and contrast of the martian surface. Scientific analysis of HRSC images (and of OMEGA spectra) requires corrections for these effects and such corrections require knowledge of the atmospheric optical depth.

The goals of our work are, first, to remove atmospheric effects from HRSC images of Mars, and second, to study the aerosols. Good atmospheric correction is a complicated task in which the Mars Odyssey and Mars Global Observer teams have invested considerable effort. In general the results of these teams have been mixed. The Mars Express team actually is in a better position since it is able to use HRSC's stereo information.

Since 2001 we have developed several algorithms to measure optical depths in the martian atmosphere from HRSC (stereo) images, and algorithms that, once the optical depth is known, can correct these images for the influence of airborne dust and other aerosols. Images of good quality can now be individually corrected with good accuracy. The programs for measuring optical depths exploit the stereo capabilities of HRSC with the so-called 'stereo method' or sometimes, when the Sun is low in the sky so that there are sufficient shadows on the surface, analyse shadows with the so-called 'shadow method'.

3.5.4 HRSC Stereo Method

During the early MEX mission, the stereo method has been validated on images of Gusev crater, where the ground-truthing of the MER rover *Spirit* was available (see Fig. 46). Since then, the method has been operational and, under optimal conditions, it appears capable of reaching an accuracy of about ±0.05 in optical depth. However, the method has several major drawbacks (see Hoekzema et al., 2009a). For example, it can not be used for images that were observed while the Sun was high in the sky; in such images the phase angles with which the stereo channels observe the surface differ too much (see Fig. 47). As an input, the stereo method needs images in which perspective effects are minimised: 'ortho-images'. Nevertheless, it typically fails when an analysed field contains rough terrain such as cliffs. The ortho projection that is used to minimise perspective effects can not cope with topography that is too steep. The stereo method only works for some of the bi-directional reflectance functions that are common on the surface of Mars. So-called normalised cumulative intensity distributions (NCIDs) are used to check manually the quality of retrievals (for further explanation, see Fig. 47).

The column optical depth of the aerosols depends strongly on the elevation of the surface. Thus, it is important to know how it changes with altitude since knowledge of

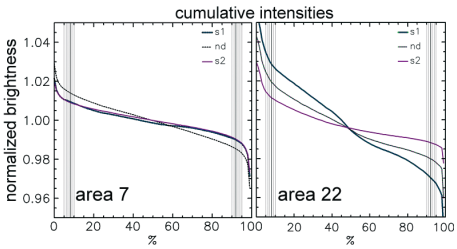

Fig. 47. Examples of normalised cumulative intensity distributions (NCIDs). An (*x*, *y*) value of e.g. (20, 1.01) tells that 20% of the analysed pixels are at least 1.01 times brighter than the average. The martian surface displays a wide range of bi-directional reflection functions. The stereo method can only work properly for a limited subset of these functions. The NCIDs offer a check on whether the bi-directional reflection function of a region allows a proper retrieval of the optical depth. The left-hand plot shows an example for a usable region: the NCIDs for s1 and s2 are quite similar, which indicates that the stereo method will probably yield a reliable result. The observations that yielded the NCIDs in the right-hand plot are not usable; this is evident from the large differences between the curves for s1 and s2. For good observations, typically between a quarter and a half of the imaged surface can be used for accurate stereo method retrievals.

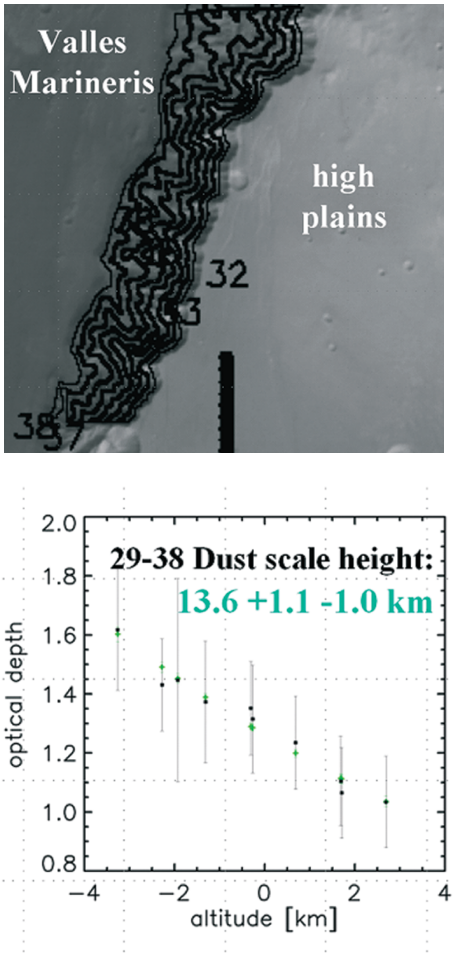

Fig. 48. ***Top:*** **Regions around contour lines (altitude ±500 m) on scree slopes in Valles Marineris. The optical depths retrieved from these regions (*bottom*) reveal a scale height of dust that is almost equal to that of gas. This indicates that over the imaged regions the dust is well mixed into the atmosphere. Other walls of the Valles (not shown) offered examples of the opposite. For details of this analysis of the Valles and the implications for the scale height of dust, see Hoekzema et al. (2009b).**

the altitude dependence makes it possible to extrapolate from a measured optical depth to the optical depth of close-by regions at different elevations. The stereo method was successfully used to study this correlation (see Fig. 48).

3.5.5 HRSC Digital Terrain Models and the shadow method

At first glance, many images of Mars show frequent shadows on its surface. However, once HRSC's digital terrain models (DTMs) became available, it became evident that many images show only shades, and hardly any true shadows. The detailed DTMs of HRSC show that on Mars, true shadows become common only when the Sun is quite low in the sky since steep slopes are quite rare on the planet. As a result, the shadow method is of limited use. In effect, it can only be used for images taken when the Sun is less than about 25° from the horizon. As a result it proved impossible to use the ground truth as measured by *Spirit* and *Opportunity* to validate the shadow method for HRSC images. There simply do not (yet) exist HRSC image sequences of the MER landing sites in Gusev and Meridiani that contain significant shadows. We expect such observations to be made during the extended mission.

3.5.6 Aerosol Scattering Properties

The Pathfinder mission yielded accurate measurements of the local aerosol properties around the landing site. Thus, before the MEX mission, we expected to have sufficient knowledge about martian aerosols to do accurate atmospheric correction once an optical depth was known. However, the results of the MEX mission made it clear that the 'Pathfinder' aerosols are not the only common aerosols in the martian atmosphere. Sometimes Pathfinder aerosols do yield accurate results in our atmospheric correction software, but more often they do not. In some cases simulations with only Pathfinder aerosols yielded errors in the estimated surface albedo of more than 20%. In this respect, HRSC stereo imagery hints at the importance of high-altitude hazes. Such hazes are thin, but apparently can be important since the small (probably often icy) particles that make up such hazes show quite strong backscattering, whereas airborne dust does not.

3.5.7 Simultaneous Observations by OMEGA and HRSC

OMEGA and HRSC usually measure reflectance simultaneously. HRSC provides very high spatial resolution images in nine channels from the VIS to the NIR, and OMEGA provides spectra from 0.36 to 5.2 µm, so these instruments complement each other. We are especially interested in these simultaneous measurements because they can help us to choose and rule out different sets of optical properties. Also, comparison of the datasets serves as a validation of the reflectance measurements. On top of that, OMEGA can detect water ice in the atmosphere (and differentiate it from that on the surface) from its measurements around 1.5 µm. All these analyses will be used to better determine the surface albedos.

With this aim in mind, we have often combined simultaneous HRSC and OMEGA measurements to determine, for instance, the composition of bright hazes detected in Valles Marineris and around volcanoes.

Simultaneous observations of HRSC and OMEGA of the Valles Marineris during the southern autumn show a dense haze inside the valley, which became thinner three days later and disappeared after nine. OMEGA spectra showed that, contrary to what one would guess from HRSC colour images, the haze contains only airborne dust and no measurable amount of ice.

Often, HRSC images show bright regions around volcanoes on Mars, probably clouds of water ice that evolve with time. Simultaneous OMEGA spectra indeed show the presence of water ice in these clouds. Figure 49 shows an example, here near the summit of Pavonis Mons, of such detection of water ice by OMEGA. The water ice is present mainly on the flank of the volcano, where the relative band depth reaches in some areas 10%. The analysis of the spectra around 3.5 µm suggests particles of the order of 2–3 µm, confirming that the absorption is due to water ice in the atmosphere. This kind of analysis helps to differentiate between atmospheric and surface ice.

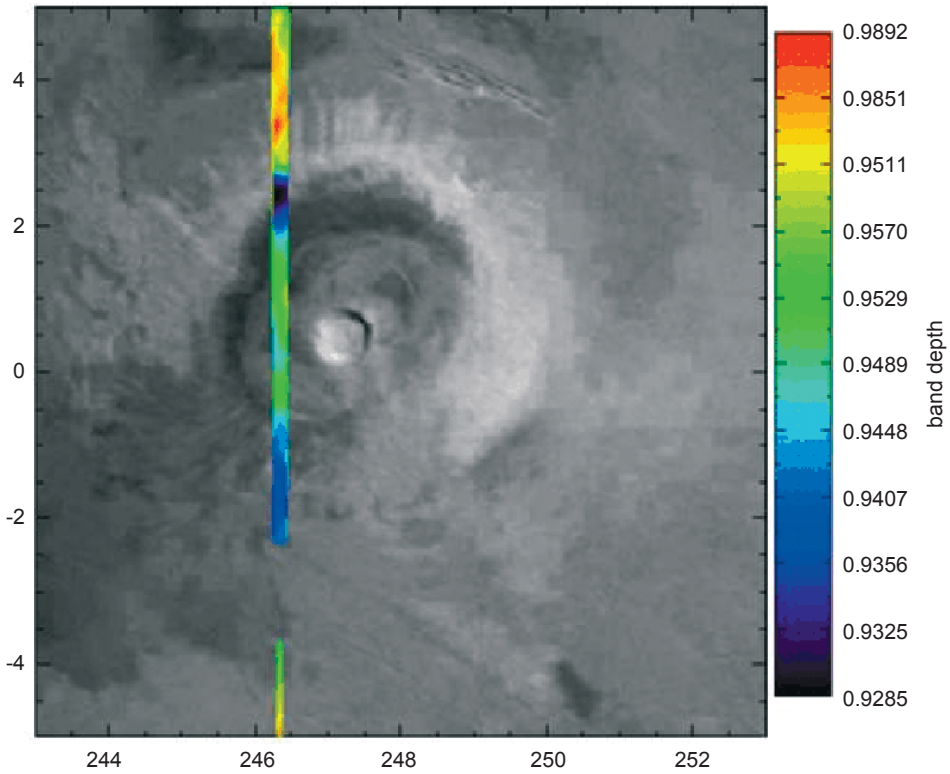

Fig. 49. OMEGA relative transmittance in the 1.5 µm band over Pavonis Mons during orbit 902. The volcano appears to be surrounded by water-ice clouds.

4.1 Joint Studies with the NASA Mars Exploration Rovers

The concurrent operation of Mars Express and the NASA Mars Exploration Rovers (MERs) has provided opportunities to obtain data from the surface and from orbit with modern instruments. For example, HRSC data were taken over the floor of Gusev crater in early 2004, shortly after the landing of the rover, *Spirit*. HRSC and MOC images showed that the landing occurred in a low-albedo surface streak inferred to be the track left by the recent passage of a dust devil. The hypothesis (based on orbiter images) was that such streaks result from the removal of a thin layer of bright dust to expose a darker substrate. As the rover traversed away from the landing site, it passed out of the streak. Microscopic imager (MI) data from the rover revealed that the soils within the streak are relatively dust-free in comparison to the brighter soils outside the streak, which were seen to be dustier, thus confirming the hypothesis for dark streak formation (Greeley et al., 2005a).

Observations from orbit by HRSC and from the ground by *Spirit* also provide complementary data. For example, prior to the landing of *Spirit* in Gusev crater, the prevailing view was that the crater floor was surfaced with aqueous deposits associated with Ma'adim Vallis. MER analyses showed the rock compositions to be predominantly basaltic, causing re-evaluation of the hypothesis. Analysis of HRSC and other orbiter data and new geological mapping of Gusev crater using higher-resolution HRSC data (Zegers et al., 2005) suggested that the crater floor was covered with lava flows similar to those seen in some craters on Earth's Moon. The MER compositional data were then used to estimate the viscosity of the basalts at the time of their emplacement in Gusev, and were found to be rather fluid in comparison to most basalts on Earth, and to have had viscosities more like those inferred for the lunar basalts. This result led to the interpretation that the floor of Gusev was flooded with basalts that were erupted from vents buried by their own products, as on the Moon, and that any sedimentary deposits associated with Ma'adim Vallis likely were also buried by the basalts (Greeley et al., 2005b).

4. Further HRSC-related Activities

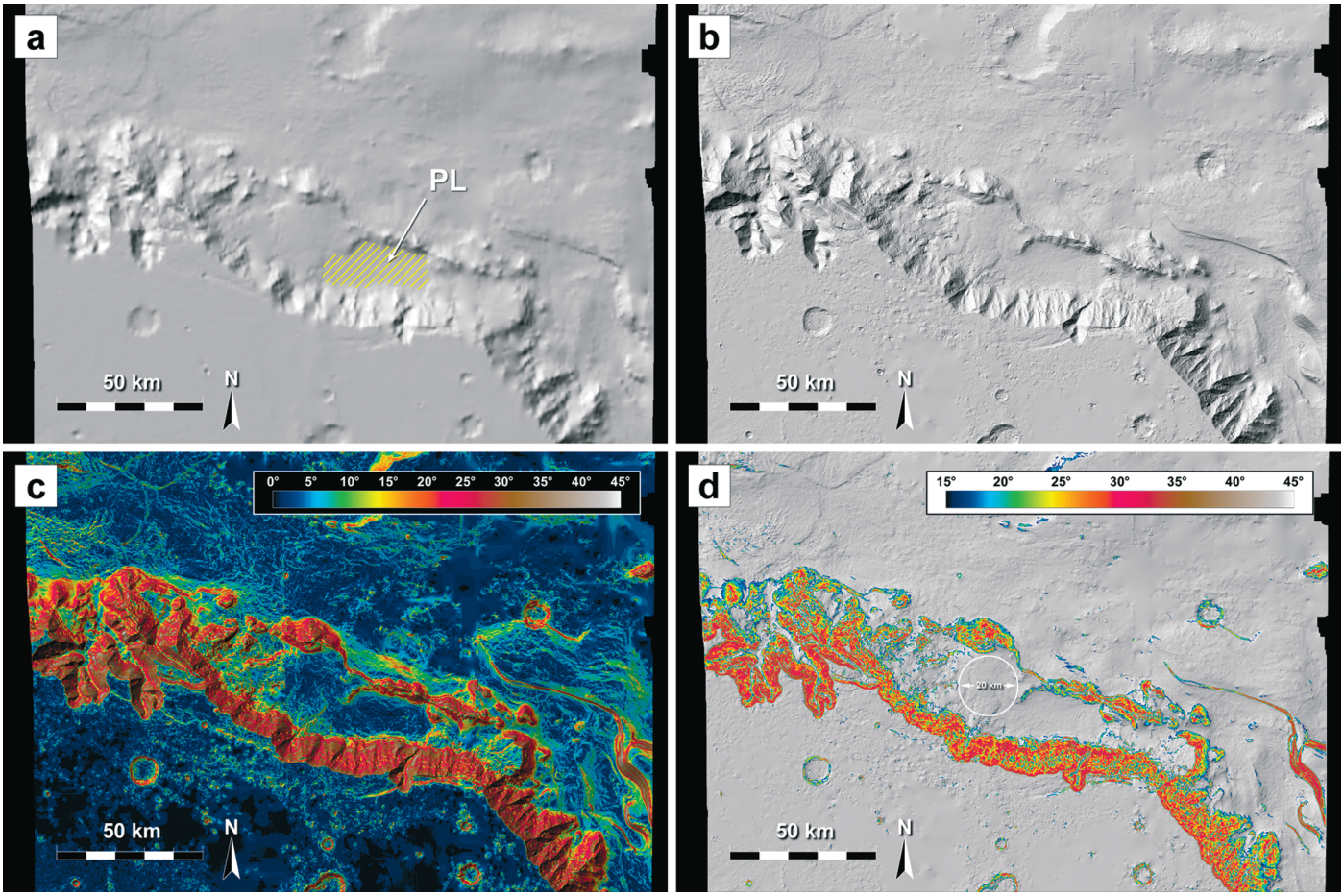

Fig. 50. Example of HRSC Digital Elevation Model (DEM) and landing site selection support. (a) Shaded relief representation of MOLA DEM (horizontal resolution ~463 m/pixel) of a region in SW Melas Chasma, Valles Marineris. The area on a topographic bench at the southern border of Melas Chasma ('PL') has been proposed as a potential landing site for the MSL mission because the morphology and mineralogy suggest the former presence of liquid water, i.e. a palaeolake (Quantin et al., 2005, 2006). (b) Shaded relief representation of HRSC DEM (horizontal resolution 50 m/pixel). Note the considerable improvement in resolution compared with the slope map based on HRSC DEM (c). (d) Slopes steeper than 15 are colour coded. All slopes within the landing ellipse (currently defined as a circle of radius 10 km) have to be 15° or less over a 20–40 m length scale in order to avoid altimetry errors in preparation for the rover release. One area that complies with this requirement is revealed by HRSC data and is marked with a white circle. It is adjacent to the possible palaeolake and could serve as a landing site from where the rover could travel to the study area.

4.2 Landing Site Selection

The focus of Mars exploration is currently shifting from orbiter missions to lander and rover missions. The Mars Exploration Rovers (Golombek et al., 2003) have successfully demonstrated the high potential of rover missions to perform detailed in situ investigations of rocks and soils (e.g. Squyres et al., 2006). Future lander and rover missions are planned by NASA (Phoenix; a Scout Mission launched in August 2007, and the Mars Science Laboratory, a large rover that will be launched in fall 2009), ESA (the ExoMars rover of the Aurora programme) and Russia (the Phobos–Grunt mission, a sample return mission to the martian moon, Phobos). The possible landing site of the Phoenix mission is already constrained to a few regions in the high-latitude northern lowlands (Arvidson et al., 2006; Seelos et al., 2006), but the landing sites for the other missions are yet to be determined.

The Mars Science Laboratory (MSL), NASA's next rover mission to Mars (Meyer et al., 2004; Vasavada and the MSL Science Team, 2006), will launch in autumn 2011 and will begin science operations a year later. The scientific goal is to explore and quantitatively assess a local region on the martian surface as a potential habitat for extant or extinct life. The MSL rover is designed to carry ten PI-led scientific instruments and a sample acquisition, processing and distribution system. The preliminary constraints on the landing site selection are described by Golombek et al. (2006). At a 2006 workshop in Pasadena, more than 30 potential landing sites were proposed (Kerr, 2006), and the possible contribution of HRSC to the landing site selection was presented by Hauber et al. (2006).

Table 6. Comparison of HRSC and other imaging instruments with high spatial resolution (from Hauber et al., 2006).

Instrument	*Spatial resolution*	*Swath width*
HRSC	~11–20 m/pixel	~60 km (at periapsis)
MOC	~few metres/pixel (cPROTO <1 m/pixel)	typically 3 km
THEMIS	19 or 38 m/pixel	20 km
THEMIS	~100 m/pixel	32 km
HiRISE	25 cm/pixel	>6 km (red) >1.2 km (blue/green/near-IR)
Context Imager	6–8 m/pixel	40 km
CRISM	18 m/pixel	~20 km

ESA's ExoMars mission will be launched in 2013. The goal is to establish whether life has ever existed on Mars, or even exists today (Vago et al., 2006). Phobos–Grunt might be launched as early as 2009 and should perform both *in situ* and remote studies of Phobos, including laboratory analysis of soil samples (Marov et al., 2004). The prerequisite for all these missions is a safe landing site. The biggest asset that HRSC can provide to landing site selection is stereo capability (Scholten et al., 2005; Gwinner et al., 2005). The resolution of the stereo channels is 10–40 m/pixel, and derived Digital Elevation Models (DEMs) have a grid spacing of 50–100 m (Fig. 50). In comparison, the distance between single Mars Orbiter Laser Altimeter (MOLA) shots, which have very high vertical accuracy, is 330 m along-track and up to several kilometres across-track at lower latitudes. The combination of the global MOLA geodetic reference frame with laterally higher-resolution HRSC images and DEMs yields excellent results. HRSC DEMs provide very good information about slopes over long (2–5 km) base lengths, and will also be useful to assess slopes over intermediate (20–40 m) base lengths. Since the swath width of HRSC is ~60 km, the entire size of a landing site ellipse (20 km diameter) can be easily covered by one HRSC image and DEM. This could be of enormous help, since no mosaicking is required, which is usually affected by different illumination and atmospheric conditions such as dust or clouds.

Another aspect that will be helpful in landing site selection is the combination of HRSC with other geospatial datasets. Very high-resolution Mars Orbiter Camera (MOC) (Malin et al., 1992) images (few metres/pixel) can easily be combined with HRSC images and DEMs. It will also be possible to combine HRSC with the upcoming HiRISE images (~30 cm/pixel) (McEwen et al., 2007), as well as with data from the Context Imager, both on NASA's MRO mission (Table 6). In contrast, the very large difference in spatial resolution between the MOC and MOLA data makes their combination much more problematic. It will be particularly useful to combine HiRISE images and HRSC DEM (HiRISE will also produce DEM, but the spatial coverage will be limited). Therefore, HRSC images and DEM can serve as bridges between lower- and higher-resolution data and are therefore ideally suited for use as base maps. Mineralogical information from spectrometers such as OMEGA (MEX) and the Compact Reconnaissance Imaging Spectrometer for Mars (CRISM, MRO) may be crucial for MSL landing site selection. In the close cooperation between the HRSC and OMEGA teams, HRSC images are already used to provide morphological context for geological interpretation. While other images (Viking, MOC and THEMIS-VIS) can also be used, HRSC images are particularly useful as a bridge to mineralogy due to their large areal extent and colour information. Therefore, HRSC

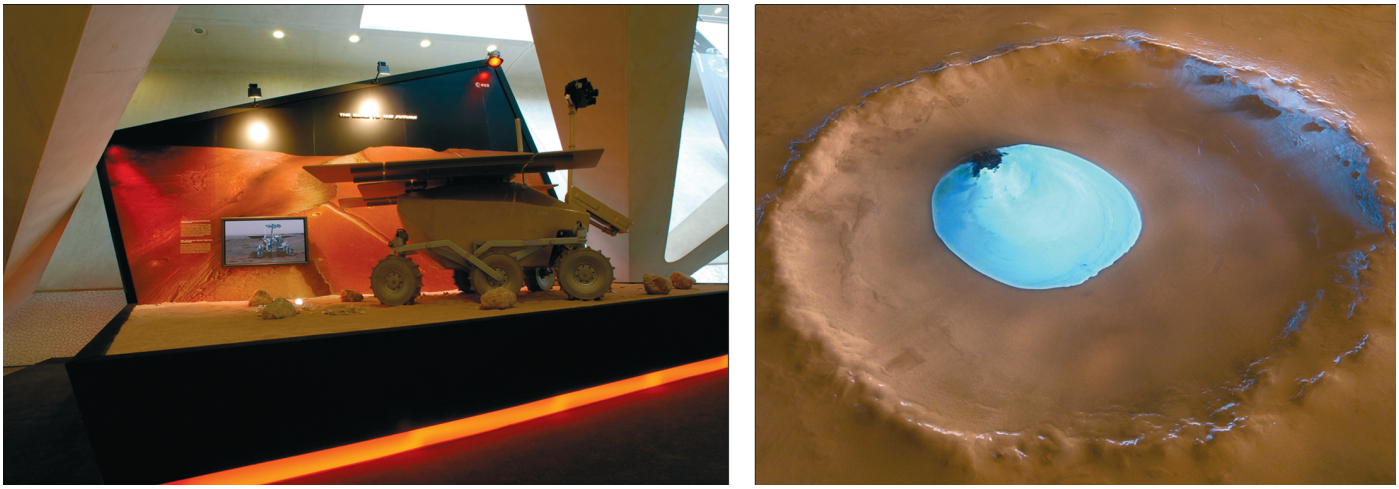

Fig. 51. ***Left:*** **Perspective view of Kasei Valles on a 6.5 × 3.5 m panel, behind a model of the ExoMars rover, at the International Astronautical Congress (IAC) 2006 in Valencia, Spain (image © ESA – M. Pedoussaut).** ***Right:*** **One of the most successful press images showing an unnamed crater with residual water ice on its floor (perspective view released in July 2005).**

data might be a very useful component among the various datasets that will be used as the basis for landing site selection.

4.3 HRSC Public Relations Efforts

HRSC data-based visualisations can be used to image products that are very close to what a human observer would perceive when travelling to Mars. The images do not necessarily require scientific knowledge, and this, together with their undeniable aesthetic quality, make them perfect instruments for igniting public interest in and awareness of the Mars Express mission (Fig. 51).

The HRSC raw data are prepared by DLR Berlin and stored in four different processing levels. They are then used by the PI team at Freie Universität Berlin to create a variety of end products for various areas of interest, such as map-projected grey-scale nadir images, RGB colour scenes, perspective views, anaglyphs and movie sequences. Since the release of the first HRSC images on 17 July 2003 a total of 314 image products and 10 movies have been produced. Combined with context maps and accompanying descriptive texts, the products were released in 67 sets for incorporation in local websites at ESA, DLR and FU Berlin.

The publication of each new set of HRSC images triggers a peak in visitor numbers to the web pages of ESA, FU Berlin and DLR. Together, the three Mars web portals attracted an estimated 1.6 million visitors in 2005. Once they are picked up by major news agencies such as Deutsche Presse-Agentur (dpa), Reuters and Agence France-Presse (AFP) and global news sources such as the British Broadcasting Corporation (BBC) and Cable News Network (CNN), the HRSC images turn up worldwide on web pages, in newspapers and magazines and on television. Regular releases of new images and text content will ensure the continued presence of the HRSC experiment and the Mars Express mission in mainstream media, and thus greater public awareness. The image content is often also used to illustrate related almanacs and books. One book has been produced with the support of the ESA Communications Department for the commercial market in English (*Space*), German (*Raumfahrt*) and French (*l'Espace*). The first copies were proudly presented to European Ministers at a meeting of the ESA Council in Berlin in December 2005.

Owing to the large areas of the surface of Mars they cover, and the level of ground detail, HRSC images are especially suitable for large print products. At the International Astronautical Congress (IAC) 2006 in Valencia, Spain, single-perspective views of Kasei Valles were scaled to cover panels of up to 6.5 × 3.5 m. In addition, the camera's 3D capabilities mean that it is possible to present the data in various forms of 3D stereo visualisation. A promising approach of 3D stereo displays,

which enable 3D perception without the need for additional devices such as glasses, has been developed in cooperation with mbm-Systems. The display panels range from postcard size to large displays 2.2 × 1 m. Exhibited in prominent places, these are always eye-catching features at the facilities of ESA, DLR and FU Berlin.

The three institutions are also using the material and its potential by participating in public events such as the 'Night of Science' in Berlin, and arranging open days at their facilities. There is also frequent support and guest lectures at observatories and cooperation with various science and space museums around the world. Most events are covered by TV and newspapers. HRSC images are exhibited at major scientific and industry events such as those of the European Geosciences Union (EGU), the Earth and Space Week (ESA/European Commission), the Farnborough International Airshow (UK), and the Berlin, Moscow and Paris air shows, to name but a few.

Probably the most successful direct contact with the public and policy makers can be attributed to the touring exhibition 'A New Perspective on Mars', prepared by DLR in cooperation with the HRSC team. Mounted at venues around the world, such as during the Germany–Japan year in Tokyo, at the University Museum in Kyoto, Japan, at the meeting of the Committee on the Peaceful Uses of Outer Space (COPUOS) in 2006 in Vienna, Austria, at the Deutsches Museum in Munich, Germany, and at the United Nations headquarters in New York, USA, in 2007, the exhibition attracted more than 500 000 visitors.

HRSC data have been used in many innovative ways, including to provide members of the public with the interactive experience of flying across the martian surface. The first opportunity was provided by DLR and the German company KUKA, who joined forces to build an unprecedented robotic flight simulator called Mars 'Robodome'. It mimics the three-dimensional movements of a real spaceship in conjunction with a visualisation of the martian surface from HRSC data. The second opportunity was initiated by a cooperation of the Open University, University College London and Imperial College London, at the Royal Society Summer Science Exhibition in London in 2006. Visitors were able to interactively fly through martian landscapes generated using HRSC data, which were projected onto a Geowall 3D Display, giving the user a truly 3D experience.

Up to now, the HRSC data have provided extensive public relations materials, and have given access to and worldwide recognition of the HRSC experiment and the ESA Mars Express mission.

References

Adams, J.B. & Gillespie, A.R. (2006). *Sensing of Landscapes with Spectral Images: A Physical Modeling Approach*, Cambridge University Press.

Albertz, J., S. Gehrke, M. Wählisch, H. Lehmann, T. Schumacher, G. Neukum & the HRSC Co-Investigator Team (2004). Digital Cartography with HRSC on Mars Express, *Int. Arch. Photogram. Rem. Sens. Spatial Inform. Sci.* **35**, 869–874.

Albertz, J., M. Attwenger, J. Barrett, S. Casley, P. Dorninger, E. Dorrer, H. Ebner, S. Gehrke, B. Giese, K. Gwinner, C. Heipke, E. Howington-Kraus, R. L. Kirk, H. Lehmann, H. Mayer, J.-P. Muller, J. Oberst, A. Ostrovskiy, J. Renter, S. Reznik, R. Schmidt, F. Scholten, M. Spiegel, M. Wählisch, G. Neukum & the HRSC Co-Investigator Team (2005). HRSC on Mars Express Photogrammetric and Cartographic Research, *Photogram. Eng. Rem. Sens.* **71**, 1153–1166.

Anderson, R.C., J.M. Dohm, M.P. Golombek, A.F.C. Haldemann, B.J. Franklin, K.L. Tanaka, J. Lias & B. Peer (2001). Primary Centers and Secondary Concentrations of Tectonic Activity through Time in the Western Hemisphere of Mars, *J. Geophys. Res*. **106**, 20563–20586.

Arvidson, R.E., L.M. Barge, J. Barnes, W.V. Boynton, J. Friedson, M.P. Golombek, J. Guinn, D.M. Kass, R. Kirk, M. Malin, M. Mellon, T. Michaels, D. Paige, T.J. Parker, S. Rafkin, K. Seelos, M.D. Smith, P.H. Smith, L. Tamppari & D. Tyler (2006). Overview of Mars Exploration Program 2007 Phoenix Mission Landing Site Selection, in *37th Lun. Planet. Sci. Conf.* Abstract 1328 (CD-ROM), League City, Houston, Texas, USA.

Attwenger, M. & G. Neukum (2005). Klassifikation von HRSC-Objektpunkten zur Generierung hochwertiger Geländemodelle der Marsoberfläche (in German), *Photogrammetrie, Fernerkundung, Geoinformation* **5**, 395–402.

Balme, M.R., N. Mangold, D. Baratoux, F. Costard, M. Gosselin, P. Masson, P. Pinet & G. Neukum (2006). Orientation and Distribution of Recent Gullies in the Southern Hemisphere of Mars: Observations from High Resolution Stereo Camera/Mars Express (HRSC/MEX) and Mars Orbiter Camera/Mars Global Surveyor (MOC/MGS) data, *J. Geophys. Res*. **111**.

Bandfield, J.L., V.E. Hamilton & P.R. Christensen (2000). A Global View of Martian Surface Compositions from MGS-TES, *Science* **287**, 1626–1630.

Banerdt, W.B., M.P. Golombek & K.L. Tanaka (1992). *Stress and Tectonics on Mars*, University of Arizona Press, pp.249–297.

Basilevsky, A. (1976). On the Evolution Rate of Small Lunar Craters, in *Proc. 7th Lunar Sci. Conf.,* Pergamon Press, Oxford, UK, pp.1005–1020.

Basilevsky, A.T., S.C. Werner, G. Neukum, J.W. Head, S. van Gasselt, K. Gwinner & B.A. Ivanov (2006). Geologically Recent Tectonic, Volcanic and Fluvial Activity on the Eastern Flank of the Olympus Mons Volcano, Mars, *Geophys. Res. Lett.* **33**, 13 201.

Basilevsky, A.T., G. Neukum, S.C. Werner, S. van Gasselt, A. Dumke, W. Zuschneid, M.G. Chapman & R. Greeley (2007). Geological Evolution of Mangala Valles, Mars: Analysis of the HRSC Image H0286, in *38th Lun. Planet. Sci. Conf.,* Lun. Planet. Inst., p.1338 (CD-ROM), League City, Houston, Texas, USA, 12–16 March.

Bleacher, J.E., R. Greeley, D.A. Williams, G. Neukum & the HRSC Co-Investigator Team (2006). Comparison of Effusive Volcanism at Olympus, Arsia, Pavonis and Ascraeus Montes, Mars from Lava Flow Mapping Using Mars Express HRSC Data, in *37th Lun. Planet. Sci. Conf*. (Eds. S. Mackwell and E. Stansbery), p.1182.

Borg, L. & Drake M.J. (2005). A Review of Meteorite Evidence for the Timing of Magmatism and of Surface or Near-surface Liquid Water on Mars, *J. Geophys. Res*. **110**, E12S03.

Buchroithner, M., T. Gründemann, K. Habermann, G. Neukum & the HRSC Co-Investigator Team (2005a). Multitemporale und grossformatige Echt-3D-Hartkopien der Marsoberfläche, *Photogrammetrie, Fernerkundung, Geoinformation* **5**, 433–438.

Buchroithner, M.F., T. Gründemann, R.L. Kirk & K. Habermann (2005b). Three in One: Multiscale Hardcopy Depiction of the Mars Surface in True-3D, *Photogram. Eng. Remote Sensing* **71**, 1105–1108.

Cabrol, N.A., E.A. Grin & G. Dawidowicz (1996). Ma'adim Vallis Revisited through New Topographic Data: Evidence for an Ancient Intravalley Lake, *Icarus* **123**, 269–283.

Carr, M.H. (1981). *The Surface of Mars*, Yale University Press, New Haven, CT.

Chapman, M.G., G. Neukum, S.C. Werner, S. van Gasselt, A. Dumke, W. Zuschneid & G. Michael (2007). Echus Chasma and Kasei Valles, Mars: New Data and Geologic Interpretations, in: *38th Lun. Planet. Sci. Conf.,* Lun. Planet. Inst., #1407 (CD-ROM), League City, Houston, Texas, USA, 12–16 March.

Chapman, C.R., J. Veverka, M.J.S. Belton, G. Neukum & D. Morrison (1996a). Cratering on Gaspra, *Icarus*, **120(1)**, 231-245.

Chapman, C.R., E.V. Ryan, W. J. Merline, G. Neukum, R. Wagner, P.C. Thomas, J. Veverka & R.J. Sullivan (1996b). Cratering on Ida, *Icarus* **120(1)**, 77-86.

Christensen, P.R., B.M. Jakosky, H.H. Kieffer, M.C. Malin, H.Y. McSween, Jr., K. Nealson, G. L. Mehall, S.H. Silverman, S. Ferry, M. Caplinger & M. Ravine (2004). The Thermal Emission Imaging System (THEMIS) for the Mars 2001 Odyssey Mission, *Space Sci. Rev.* **110**, 85–130.

Coomb, J.P. & T.B. McCord (2006). Investigation of the Spectrophotometric Measurements by the Mars Express HRSC and OMEGA instruments, *Adv. Space Res*., **43(1)**, 128–137.

Di Achille, G., L. Marinangeli, G.G. Ori, E. Hauber, K. Gwinner, D. Reiss & G. Neukum (2006a). Geological Evolution of the Tyras Vallis Paleolacustrine System, Mars, *J. Geophys. Res*. **111**, 4003.

Di Achille, G., G.G. Ori, D. Reiss, E. Hauber, K. Gwinner, G. Michael & G. Neukum (2006b). A steep fan at Coprates Catena, Valles Marineris, Mars, as Seen by HRSC data, *Geophys. Res. Lett*. **33**, 7204.

Dorrer, E., H. Mayer, Y. Haase, A. Ostrovskiy, J. Renter, M. Rentsch, S. Reznik, G. Neukum & the HRSC Co-Investigator Team (2005). Improvement of Spatial Data by Means of Shape-from-Shading (in German), *Photogrammetrie, Fernerkundung, Geoinformation* **5**, 403–408.

Ebner, H., M. Spiegel, A. Baumgartner, B. Giese, G. Neukum & the HRSC Co-Investigator Team (2004). Improving the Exterior Orientation of Mars Express HRSC imagery, *Int. Arch. Photogram. Rem. Sens. Spatial Inform. Sci.* **35**, 852–857.

Eliason, E. (1997). Production of Digital Image Models Using the ISIS System, *Lun. Planet. Sci. Conf. Abstracts* **XXVIII**, p.331–332.

Eliason, E., T. Hare, H. Kieffer, E. Lee, J. Mathews, L. Soderblom, T. Sucharski & J. Torson (1997). An Overview of the Integrated Software for Imaging Spectrometers (ISIS), *Lun. Planet. Sci. Conf. Abstracts* **XXVIII**, pp. 387–388.

Fassett, C.I. & J.W. Head (2006a). Valley Formation on Martian Volcanoes in the Hesperian: Evidence for Melting of Summit Snowpack, Caldera Lake Formation, Drainage and Erosion at Ceraunius Tholus, *Icarus*, **189**, 118–135

Fassett, C.I. & J.W. Head, III (2006b). Valleys on Hecates Tholus, Mars: Origin by Basal Melting of Summit Snowpack, *Planet. Space Sci*. **54**, 370–378.

Ferri, F., P.H. Smith, M. Lemmon & N.O. Renno (2003). Dust Devils as Observed by Mars Pathfinder, *J. Geophys. Res*. **108**.

Forget, F., R.M. Haberle, F. Montmessin, B. Levrard & J.W. Head (2006). Formation of Glaciers on Mars by Atmospheric Precipitation at High Obliquity, *Science* **311**, 368–371.

Gaddis, L., J. Anderson, K. Becker, T. Becker, D. Cook, K. Edwards, E. Eliason, T. Hare, H. Kieffer, E. Lee, J. Mathews, L. Soderblom, T. Sucharski, J. Torson, A. McEwen & M. Robinson (1997), An Overview of the Integrated Software for Imaging Spectrometers (ISIS), *Lun. Planet. Sci. Conf. Abstracts* **XXVIII**, p.387–388.

Gehrke, S., M. Wählisch, H. Lehmann, J. Albertz & T. Roatsch (2005). Generation of Digital Topographic Maps of Planetary Bodies, *Int. Arch. Photogram. Rem. Sens. Spatial Inform. Sci.* **36**.

Giese, B., J. Oberst, F. Scholten, H. Hoffmann, M. Spiegel, G. Neukum & the HRSC Co-Investigator Team (2005). Ein hoch auflösendFes digitales Oberflächenmodell des Marsmondes Phobos (in German), *Photogrammetrie, Fernerkundung, Geoinformation* **5**, 435–440.

Gillespie, A.R., D.R. Montgomery & A. Mushkin (2005). Planetary Science: Are there Active Glaciers on Mars? *Nature* **438**.

Golombek, M.P. & W.B. Banerdt (1999). Recent Advances in Mars Tectonics, in *5th Int. Conf. on Mars,* Pasadena, CA.

Golombek, M.P., J.A. Grant, T.J. Parker, D.M. Kass, J.A. Crisp, S.W. Squyres, A.F.C. Haldemann, M. Adler, W.J. Lee, N.T. Bridges, R.E. Arvidson, M.H. Carr, R.L. Kirk, P.C. Knocke, R.B. Roncoli, C.M. Weitz, J.T. Schofield, R.W. Zurek, P.R. Christensen, R.L. Fergason, F.S. Anderson & J.W. Rice (2003). Selection of the Mars Exploration Rover Landing Sites, *J. Geophys. Res*. **108**, 13–1.

Golombek, M., J. Grant, L. Lorenzoni, A. Steltzner, A. R. Vasavada, C. Voorhees & M. Watkins (2006). Preliminary Constraints and Plans for Mars Science Laboratory Landing Site Selection, in *37th Lun. Planet. Sci. Conf*., **#2172** (CD-ROM), League City, Houston, Texas.

Greeley, R. & J.D. Iversen (1987). Measurements of Wind Friction Speeds over Lava Surfaces and Assessment of Sediment Transport, *Geophys. Res. Lett*. **14**, 925–928.

Greeley, R. & P.D. Spudis (1981). Volcanism on Mars, *Rev. Geophys. Space Phys.* **19**, 13–41.

Greeley, R., R. Arvidson, J.F. Bell, P. Christensen, D. Foley, A. Haldemann, R.O. Kuzmin, G. Landis, L.D.V. Neakrase, G. Neukum, S. W. Squyres, R. Sullivan, S. D. Thompson, P.L. Whelley & D. Williams (2005a). Martian Variable Features: New Insight from the Mars Express Orbiter and the Mars Exploration Rover *Spirit*, *J. Geophys. Res.* **110**, 6002.

Greeley, R., B.H. Foing, H.Y. McSween, G. Neukum, P. Pinet, M. van Kan, S.C. Werner, D. A. Williams & T.E. Zegers (2005b). Fluid Lava Flows in Gusev Crater, Mars, *J. Geophys. Res.* **110**, 5008.

Greeley, R., R.E. Arvidson, P.W. Barlett, D. Blaney, N.A. Cabrol, P.R. Christensen, R.L. Fergason, M.P. Golombek, G.A. Landis, M.T. Lemmon, S.M. McLennan, J.N. Maki, T. Michaels, J.E. Moersch, L.D.V. Neakrase, S.C.R. Rafkin, L. Richter, S.W. Squyres, P.A.

de Souza, R.J. Sullivan, S.D. Thompson & P.L. Whelley (2006). Gusev Crater: Wind-related Features and Processes Observed by the Mars Exploration Rover *Spirit*, *J. Geophys. Res. (Planets)* **111**.

Grin, E.A. & N.A. Cabrol (1997). Limnologic Analysis of Gusev Crater Paleolake, Mars, *Icarus* **130**, 461–474.

Grott, M., E. Hauber, S. Werner, P. Kronberg & G. Neukum (2005). High Heat Flux on Ancient Mars: Evidence from Rift Flank Uplift at Coracis Fossae, *Geophys. Res. Lett*. **32**, L21201.

Grott, M., E. Hauber, S.C. Werner, P. Kronberg & G. Neukum (2006). Mechanical Modeling of Thrust Faults in the Thaumasia Region, Mars and Implications for the Noachian Heat Flux, *Icarus* **186(2)**, 517–526.

Gwinner, K., E. Hauber, R. Jaumann & G. Neukum (2000). High-Resolution, Digital Photogrammetric Mapping: A Tool for Earth Science, *Eos Trans*. **81**, 513–520.

Gwinner, K., F. Scholten, B. Giese, J. Oberst, R. Jaumann, M. Spiegel, R. Schmidt, G. Neukum & the HRSC Co-Investigator Team (2005). Hochauflösende Digitale Geländemodelle auf der Grundlage von Mars Express HRSC-Daten, (in German), *Photogrammetrie, Fernerkundung, Geoinformation* **5**, 387–394.

Hartmann, W.K. & G. Neukum (2001). Cratering Chronology and the Evolution of Mars, *Space Sci. Rev.* **96(1–4)**, 165–194.

Hauber, E. & P. Kronberg (2001). Tempe Fossae, Mars: A Planetary Analogon to a Terrestrial Continental Rift? *J. Geophys. Res.* **106**, 20 587–20 602.

Hauber, E. & P. Kronberg (2005). The Large Thaumasia Graben on Mars: Is it a Rift? *J. Geophys. Res*. **110**, 7003.

Hauber, E., S. van Gasselt, B. Ivanov, S. Werner, J.W. Head, G. Neukum, R. Jaumann, R. Greeley, K.L. Mitchell, P. Muller & the HRSC Co-Investigator Team (2005a). Discovery of a Flank Caldera and Very Young Glacial Activity at Hecates Tholus, Mars, *Nature* **434**, 356–361.

Hauber, E., K. Gwinner, D. Reiss, F. Scholten, G.G. Michael, R. Jaumann, G.G. Ori, L. Marinangeli, G. Neukum & the HRSC Co-Investigator Team (2005b). Delta-like Deposits in Xanthe Terra, Mars, as Seen with the High Resolution Stereo Camera (HRSC), in 36th *Lun. Planet. Sci. Conf*. (Eds. S. Mackwell & E. Stansbery), pp.1661.

Hauber, E., G. Neukum, R. Jaumann, K. Gwinner, F. Scholten, H. Hoffmann, S. van Gasselt & T. Duxbury (2006). The High Resolution Stereo Camera (HRSC): A Tool for Landing Site Selection, in *1st MSL Landing Site Workshop*, Pasadena, California.

Head, J.W. & D.R. Marchant (2003). Cold-based Mountain Glaciers on Mars: Western Arsia Mons, *Geology* **31**, 641–644.

Head, J.W., III & D.R. Marchant (2006). Evidence for Global-Scale Northern Mid-Latitude Glaciation in the Amazonian Period of Mars: Debris-covered Glacier and Valley Glacier Deposits in the 30–50°N Latitude Band, in *37th Ann. Lun. Planet. Sci. Conf*. (Eds. S. Mackwell and E. Stansbery), pp.1127.

Head, J.W., G. Neukum, R. Jaumann, H. Hiesinger, E. Hauber, M. Carr, P. Masson, B. Foing, H. Hoffmann, M. Kreslavsky, S. Werner, S. Milkovich, S. van Gasselt & the HRSC Co-Investigator Team (2005a). Tropical to Mid-latitude Snow and Ice Accumulation, Flow and Glaciation on Mars, *Nature* **434**, 346–351.

Head, J.W., G. Neukum, R. Jaumann, H. Hiesinger, E. Hauber, M. Carr, P. Masson, B. Foing, H. Hoffmann, M. Kreslavsky, S. Werner, S. Milkovich, S. van Gasselt & the HRSC Co-Investigator Team (2005b). Planetary Science: Are There Active Glaciers on Mars? (Reply), *Nature* **438**.

Head, J.W., D.R. Marchant, M.C. Agnew, C.I. Fassett & M.A. Kreslavsky (2006a). Extensive Valley Glacier Deposits in the Northern Mid-latitudes of Mars: Evidence for Late Amazonian Obliquity-driven Climate Change, *Earth Planet. Sci. Lett*. **241**, 663–671.

Head, J.W., A.L. Nahm, D.R. Marchant & G. Neukum (2006b). Modification of the Dichotomy Boundary on Mars by Amazonian Mid-latitude Regional Glaciation, *Geophys. Res. Lett*. **33**, L08S03.

Heipke, C., R. Schmidt, R. Brand, J. Oberst, G. Neukum & the HRSC Co-Investigator Team (2004). Performance of Automatic Tie Point Extraction Using HRSC Imagery of the Mars Express Mission, *Int. Arch. Photogram. Rem. Sens. Spatial Inform. Sci.* **35**, 846–851.

Heipke, C., J. Oberst, J. Albertz, M. Attwenger, P. Dorninger, E. Dorrer, M. Ewe, S. Gehrke, K. Gwinner, H. Hirschmller, J. R. Kim, R. L. Kirk, H. Mayer, R. Muller, J.-P.and Rengarajan, M. Rentsch, R. Schmidt, F. Scholten, J. Shan, M. Spiegel, M. Wählisch, G. Neukum & the HRSC Co-Investigator Team (2006). The HRSC DTM Test, *Int. Arch. Photogram. Rem. Sens. Spatial Inform. Sci.* **36**, 311–325.

Hiesinger, H., J.W. Head, III, G. Neukum & the HRSC Co-Investigator Team (2005). Rheological Properties of Late-Stage Lava Flows on Ascraeus Mons: New Evidence from HRSC, in *36th Annual Lun. Planet. Sci. Conf.* (Eds. S. Mackwell & E. Stansbery), pp. 1727.

Hoekzema, N.M., W.J. Markiewicz, B. Grieger, K. Gwinner, S. Hviid, H.U. Keller, H. Hoffmann, G. Neukum (2009a). Atmospheric Optical Depths from HRSC Stereo Images of Mars, *Earth Planet. Sci. Lett.* submitted.

Hoekzema, N.M., W.J. Markiewicz, B. Grieger, K. Gwinner, S. Hviid, H. U. Keller, H. Hoffmann, G. Neukum & the MER Co-Investigator Team (2009b). The Dust-scale Height of the Martian Atmosphere around Valles Marineris from HRSC Stereo Images, *Earth Planet. Sci. Lett.* submitted.

Ivanov, B.A. (2001). Mars/Moon Cratering Rate Ratio Estimates, *Space Sci. Rev.* **96(1/4)**, 87–104.

Jaumann, R., D. Reiss, S. Frei, G. Neukum, F. Scholten, K. Gwinner, T. Roatsch, K.-D. Matz, V. Mertens, E. Hauber, H. Hoffmann, U. Köhler, J. W. Head, H. Hiesinger & M. H. Carr (2005a). Interior Channels in Martian Valleys: Constraints on Fluvial Erosion by Measurements of the Mars Express High Resolution Stereo Camera, *Geophys. Res. Lett*. **32**, 16, 203.

Jaumann, R., D. Reiss, S. Frei, F. Scholten, K. Gwinner, T. Roatsch, K.-D. Matz, E. Hauber, V. Mertens, H. Hoffmann, J.W. Head, III, H. Hiesinger, M.H. Carr, G. Neukum & the HRSC Co-Investigator Team (2005b). Martian Valley Networks and Associated Fluvial Features as Seen by the Mars Express High Resolution Stereo Camera (HRSC), in *36th Ann. Lun. Planet. Sci. Conf.* (Eds. S. Mackwell & E. Stansbery), pp.1765.

Jaumann, R., G. Neukum, T. Behnke, T.C. Duxbury, J. Flohrer, S. van Gasselt, B. Giese, K. Gwinner, E. Hauber, H. Hoffmann, U. Köhler, K.-D. Matz, T.B. McCord, V. Mertens, J. Oberst, R. Pischel, D. Reiss, T. Roatsch, P. Saiger, F. Scholten, G. Schwarz, K. Stephan & M. Wählisch (2007). The High Resolution Stereo Camera (HRSC) Experiment on Mars Express: Instrument Aspects and Experiment Conduct from Interplanetary Cruise through the Nominal Mission, *Planet. Space Sci.* **55**, 928–952.

Kerr, R. (2006). In Search of the Red Planet's Sweet Spot, *Science* **312**, 1588–1590.

Kim, J.R., J.-P. Muller, S. van Gasselt, J.G. Morley, G. Neukum & the HRSC Co-Investigator Team (2005). Automated Crater Detection, A New Tool for Mars Cartography and Chronology, *Photogram. Eng. Rem. Sens.* **71(10)**, 1205–1217.

Kirk, R., K. Thompson & E.M. Lee (2001). Photometry of the Martian Atmosphere: An Improved Practical Model for Cartography and Photoclinometry, in *Lun. Planet. Sci. Conf. Abstracts,* **XXXII**, abstract 1874 (CD–ROM).

Kirk, R., J. Barrett & L. Soderblom (2003). Photoclinometry Made Simple? in ISPRS-ET Working Group IV/9 Workshop 'Advances in Planetary Mapping'.

Kirk, R.L., S.W. Squyres, G. Neukum & the MER Athena and MEX HRSC Science Teams (2004). Topographic Mapping of Mars: From Hectometer to Micrometer Scales, *Int. Arch. Photogram. Rem. Sens. Spatial Inform. Sci.* **35**, 834–839.

Kirk, R., E. Howington-Kraus, D. Galuszka, B. Redding & T. Hare (2006). Topomapping of Mars with HRSC images, ISIS, and a Commercial Stereo Workstation, *Int. Arch. Photogram. Rem. Sens. Spatial Inform. Sci.* **36**.

Kneissl, T. (2006). Verbreitung und Azimutabhängigkeiten von Erosionsrinnen in der nördlichen Hemisphäre des Mars, Master's thesis, Martin–Luther–Universitaet, Halle Wittenberg.

Kronberg, P., E. Hauber, S. Werner, T. Schäfer, K. Gwinner, B. Giese, P. Masson & G. Neukum (2006). Acheron Fossae, Mars: Tectonic Rifting, Volcanism, and Implications for Lithospheric Thickness, *J. Geophys. Res,* **112**, E04005.

Lainey, V., V. Dehant, J. Oberst & M. Pätzold (2005). New Ephemerides of the Martian Moons, *Eos Trans. AGU* **86**, Fall Meeting, Suppl., Abstract G51A–0802.

Laskar, J., A.C.M. Correia, M. Gastineau, F. Joutel, B. Levrard & P. Robutel (2004). Long-term Evolution and Chaotic Diffusion of the Insolation Quantities of Mars, *Icarus* **170**, 343–364.

Lyra, von G. (1940). Über den Einfluß von Bodenerhebungen auf die Strömung einer stabil geschichteten Atmosphäre, *Beiträge zur Physik der freien Atmosphäre* **26**, 197–206.

McCord, T.B., R.B. Singer, B.R. Hawke, J.B. Adams, D.L. Evans, J.W. Head, P.J. Mouginis-Mark, C.M. Pieters, R.L. Huguenin & S.H. Zisk (1982). Mars: Definition and Characterization of Global Surface Units with Emphasis on Composition, *J. Geophys. Res*. **87**, 10 129–10 148.

McCord, T.B., J.B. Adams, G. Bellucci, J.-P. Combe, A.R. Gillespie, G. Hansen, H. Hoffmann, R. Jaumann, G. Neukum, P. Pinet, F. Poulet, K. Stephan, the HRSC Spectrophotometric Working Group & the HRSC Co-Investigator Team (2006). The Mars Express High Resolution Stereo Camera Spectrophotometric Data: Characteristics and Science Analysis, *J. Geophys. Res*. **112**, E06004.

McEwen, A.S. (2003). Secondary Cratering on Mars: Implications for Age Dating and Surface Properties, in: *6th Int. Conf. Mars,* Lun. Planet. Inst., Pasadena, California, 20–25 July.

McEwen, A.S. (2006). Cratering Age Considerations for Young Terranes in the Inner Solar System, in: *Lun. Planet. Sci. Conf.*, Lun. Planet. Inst., #6030 (CD-ROM), League City, Houston, Texas, USA.

McEwen, A.S., B.S. Preblich, E.P. Turtle, N.A. Artemieva, M.P. Golombek, M. Hurst, R.L. Kirk, D.M. Burr & P.R. Christensen (2005). The Rayed Crater Zunil and Interpretations of Small Impact Craters on Mars, *Icarus* **176(2)**, 351-381.

McEwen, A.S., E.M. Eliason, J.W. Bergstrom, N.T. Bridges, C.J. Hansen, W.A. Delamere, J.A. Grant, V.C. Gulick, K.E. Herkenhoff, L. Keszthelyi, R.L. Kirk, M.T. Mellon, S.W. Squyres, N. Thomas & C.M. Weitz (2007). MRO's High Resolution Imaging Science Experiment (HiRISE), J. Geophys. Res, 112, E05S02.

McSween, H.Y., R.E. Arvidson, J.F. Bell, D. Blaney, N.A. Cabrol, P.R. Christensen, B.C. Clark, J.A. Crisp, L.S. Crumpler, D.J. Des Marais, J.D. Farmer, R. Gellert, A. Ghosh, S. Gorevan, T. Graff, J. Grant, L.A. Haskin, K.E. Herkenhoff, J.R. Johnson, B.L. Jolliff, G. Klingelhoefer, A.T. Knudson, S. McLennan, K.A. Milam, J.E. Moersch, R.V. Morris, R. Rieder, S.W. Ruff, P.A. de Souza, S.W. Squyres, H. Wänke, A. Wang, M.B. Wyatt, A. Yen & J. Zipfel (2004). Basaltic Rocks Analyzed by the *Spirit* Rover in Gusev Crater, *Science* **305**, 842–845.

Malin, M.C. & K.S. Edgett (2000). Evidence for Recent Groundwater Seepage and Surface Runoff on Mars, *Science*, **288**, 2330–2335.

Malin, M.C. & K.S. Edgett (2001). Mars Global Surveyor Mars Orbiter Camera: Interplanetary Cruise through Primary Mission, *J. Geophys. Res*. **106**, 23 429–23 570.

Malin, M.C., G.E. Danielson, A.P. Ingersoll, H. Masursky, J. Veverka, M.A. Ravine & T.A. Soulanille (1992). Mars Observer Camera, *J. Geophys. Res*. **97**, 7699–7718.

Malin, M.C., K.S. Edgett, L.V. Posiolova, S.M. McColley & E.Z.N. Dobrea (2006). Present-Day Impact Cratering Rate and Contemporary Gully Activity on Mars, *Science*, **314(5805)**, 1573–1577.

Marov, M.Y., V.S. Avduevsky, E.L. Akim, T.M. Eneev, R.S. Kremnev, S.D. Kulikov, K.M. Pichkhadze, G.A. Popov & G.N. Rogovsky (2004). Phobos-Grunt: Russian Sample Return Mission, *Adv. Space Res*. **33**, 2276–2280.

Metzger, S.M., J.R. Carr, J.R. Johnson, T.J. Parker & M.T. Lemmon (1999). Dust Devil Vortices Seen by the Mars Pathfinder Camera, *Geophys. Res. Lett*. **26**, 2781–2784.

Meyer, M., F. Palluconi & J. Rummel (2004). Mars Science Laboratory Goals and Challenges, in *35th COSPAR Scientific Assembly,* abstract 3837, Paris.

Michael G., van Gasselt S., Walter S., Neukum G. & Jaumann R. (2006). HRSC View-Web: A Web-Based Exploration System for Mars Express HRSC images, in: *1st Europ. Planet. Sci. Conf*., Berlin.

Michael, G. & G. Neukum (2007). Refinement of Cratering Model Age for the Case if Partial Resurfacing, in *38th Lun. Planet. Sci. Conf.,* Lun. Planet. Inst., League City, Houston, Texas, USA.

Milkovich, S.M., J.W. Head & D.R. Marchant (2006). Debris-covered Piedmont Glaciers along the Northwest Flank of the Olympus Mons Scarp: Evidence for Low-latitude Ice Accumulation during the Late Amazonian of Mars, *Icarus* **181**, 388–407.

Miller, S.B. & A. Walker (1993). Further Developments of Leica Digital Photogrammetric Systems by Helava, in A*CSM/ASPRS Ann. Convention and Exposition Technical Papers*, **3**, 256–263.

Montgomery, D.R. & A. Gillespie (2005). Formation of Valles Marineris and Associated Outflow Channels by Catastrophic Dewatering of Evaporite Deposits, *Geology* **33**, 625–628.

Mouginis-Mark, P.J., J.W. Head, III & L. Wilson (1982). Explosive Volcanism on Hecates Tholus, Mars – Investigation of Eruption Conditions, *J. Geophys. Res*. **87**, 9890–9904.

Mueller, K. & M. Golombek (2004). Compressional Structures on Mars, *Ann. Rev. Earth Planet. Sci.* **32**.

Murray, J.B., J.-P. Muller, G. Neukum, S.C. Werner, S. van Gasselt, E. Hauber, W.J. Markiewicz, J.W. Head, B.H. Foing, D. Page, K.L. Mitchell, G. Portyankina & the HRSC Co-Investigator Team (205). Evidence from the Mars Express High Resolution Stereo Camera for a Frozen Sea Close to Mars' Equator, *Nature* **434**, 352–356.

Neukum, G. (1983). Meteoritenbombardement und Datierung planetarer Oberflächen, Habilitation thesis, Ludwig-Maximilians-Universität München, München.

Neukum, G. (1999). The Airborne HRSC-A: Performance Results and Application Potential, in *Photogrammetric Week,* D. Fritsch & R. Spiller, Eds., Wichmann, Stuttgart, Germany, pp.83–88.

Neukum, G. & K. Hiller (1981). Martian Ages, *J. Geophys. Res*. **86**, 3097–3121.

Neukum, G. &H. Hoffmann (2000). Imaging Mars, in *Towards Mars* (Eds. R. Pellinen & P. Raudsepp), Oy Raud Publishing Ltd, Helsinki.

Neukum, G. & B.A. Ivanov (1994). Crater Size Distributions and Impact Probabilities on Earth from Lunar, Terrestrial-planet, and Asteroid Cratering Data, in *Hazards Due to Comets and Asteroids* (Eds. T. Gehrels, M.S. Matthews & A. Schumann), University Arizona Press, Tucson, AZ, p.359.

Neukum, G. & D.U. Wise (1976). Mars – A Standard Crater Curve and Possible New Time Scale, *Science* **194**(4272), 1381–1387.

Neukum, G., B. A. Ivanov & W. K. Hartmann (2001). Cratering Records in the Inner Solar System in Relation to the Lunar Reference System, in: *ISSI Workshop 'Chronology and Evolution of Mars'*, Space Sciences Series of ISSI, Bern, Switzerland, 10–14 April 2000, Kluwer Academic Publishers, pp.55–86.

Neukum, G., R. Jaumann, H. Hoffmann, E. Hauber, J.W. Head, A.T. Basilevsky, B.A. Ivanov, S.C. Werner, S. van Gasselt, J.B. Murray, T. McCord & the HRSC Co-Investigator Team (2004a). Recent and Episodic Volcanic and Glacial Activity on Mars Revealed by the High Resolution Stereo Camera, *Nature* **432**, 971–979.

Neukum, G., R. Jaumann & the HRSC Team (2004b). HRSC: The High Resolution Stereo Camera of Mars Express, in *Mars Express: The Scientific Payload,* ESA SP-1240, ESA Publications Division, European Space Agency, Noordwijk, the Netherlands, pp.17–35.

Neukum, G., A.T. Basilevsky, S. van Gasselt, R. Greeley, E. Hauber, J.W. Head, H. Hoffmann, B.A. Ivanov, R. Jaumann, T.B. McCord, S. Preuschmann, S. Werner, D. A. Williams, U. Wolf & the HRSC Co-Investigator Team (2006). New Insights into the Geological Evolution of Mars through the Mars Express High Resolution Stereo Camera (HRSC), in: *37th Lun. Planet. Sci. Conf.,* Lun. Planet. Inst., #2379 (CD-ROM), League City, Houston, Texas, 13–17 March.

Neukum, G., A.T. Basilevsky, M.G. Chapman, S.C. Werner, S. van Gasselt, R. Jaumann, E. Hauber, H. Hoffmann, U. Wolf, J.W. Head, R. Greeley, T.B. McCord & the HRSC Co-Investigator Team (2007). The Geologic Evolution of Mars: Episodicity of Resurfacing Events and Ages from Cratering Analysis of Image Data and Correlation with Radiometric Ages of Martian Meteorites, in: *38th Lun. Planet. Sci. Conf.,* Lun. Planet. Inst., #2271 (CD-ROM), League City, Houston, Texas, 12–16 March.

L.E. Nyquist, D.D. Bogard, C.-Y. Shih, A. Greshake, D. Stöffler & O. Eugster (2001). Ages and Geologic Histories of Martian Meteorites. In: *Chronology and Evolution of Mars* (Eds. R. Kallenbach, J. Geiss & W.K. Hartmann), Kluwer, Dordrecht, pp.105–164.

Neumann, G., F. Lemoine, D. Smith & M. Zuber (2003). The Mars Obiter Laser Altimeter Archive: Final Precision Experiment Data Record Release and Status of Radiometry, *Lun. Planet. Sci. Conf. Abstracts* **XXXIV**, CD–ROM abstract #1978.

Oberst, J., K.-D. Matz., T. Roatsch, B. Giese, H. Hoffmann, T. Duxbury & G. Neukum (2006). Astrometric Observations of Phobos and Deimos with the SRC on Mars Express, *Astron. Astrophys.* **447**, 1145–1151.

Olsen, K.H. & P. Morgan (1995). Introduction: Progress in Understanding Continental Rifts, in *Continental Rifts: Evolution, Structure, Tectonics* (Ed. K.H. Olsen), Elsevier: New York, pp.3–26.

Ori, G.G. & C. Mosangini (1998). Complex Depositional Systems in Hydraotes Chaos, Mars: An Example of Sedimentary Process Interactions in the Martian Hydrological Cycle, *J. Geophys. Res.* **103**, 22713–22724.

Ori, G.G., L. Marinangeli & A. Baliva (2000a). Terraces and Gilbert-type Deltas in Crater Lakes in Ismenius Lacus and Memnonia (Mars), *J. Geophys. Res*. **105**, 17629–17642.

Ori, G.G., L. Marinangeli & G. Komatsu (2000b). Martian Paleolacustrine Environments and their Geological Constraints on Drilling Operations for Exobiological Research, *Planet. Space Sci.* **48**, 1027–1034.

Pinet, P.C., V.V. Shevchenko, D.D. Chevrel, Y.H. Daydou & C. Rosemberg (2000). Local and Regional Lunar Regolith Characteristics at Reiner Gamma Formation: Optical and Spectroscopic Properties from Clementine and Earth-based Data, *J. Geophys. Res*. **105**, 9457–9475.

Pondrelli, M., A.P. Rossi, L. Marinangeli, G.G. Ori, S. di Lorenzo, A. Baliva, E. Hauber, G. Neukum & the HRSC Team (2006). Morphofacies Analysis of the Eberswalde Crater (Mars), in *37th Ann. Lun. Planet. Sci. Conf.* (Eds. S. Mackwell & E. Stansbery), pp.1555.

Quantin, C., P. Allemand, N. Mangold, G. Dromart & C. Delacourt (2005). Fluvial and Lacustrine Activity on Layered Deposits in Melas Chasma, Valles Marineris, Mars, *J. Geophys. Res.* **110**, 12.

Quantin, C., C. Weitz, R. Williams, G. Dromart & N. Mangold (2006). Paleo-lake in Melas Chasma (Valles Marineris) as a Potential Landing Site for MSL, in *First MSL Landing Site Workshop,* Pasadena.

Renn, N.O., A.A. Nash, J. Lunine & J. Murphy (2000). Martian and Terrestrial Dust Devils: Test of a Scaling Theory Using Pathfinder data, *J. Geophys. Res*. **105**, 1859–1865.

Roatsch, T. (2005). *MEX-HRSC to Planetary Science Archive Interface Control Document for Level-3 Data (EAICD),* Tech. Rep. HRSC-DLR-TN-4200-008, German Aerospace Center (DLR).

Ryan, J.A. & R.D. Lucich (1999). Possible Dust Devils, Vortices on Mars, *J. Geophys. Res.* **88**, 11 005–11 011.

Schmidt, R., C. Heipke, G. Neukum & the HRSC Co-Investigator Team (2006). Improving Tie Point Extraction by Anisotropic Diffusion, *Int. Arch. Photogram. Rem. Sens. Spatial Inform. Sci.* **36**, 352–357.

Scholten, F., K. Gwinner, T. Roatsch, K.-D. Matz, M. Wählisch, B. Giese, J. Oberst, R. Jaumann, G. Neukum & the HRSC Co-Investigator Team (2005). Mars Express HRSC Data Processing Methods and Operational Aspects, *Photogram. Eng. Rem. Sens.* **71**, 1143–1152.

Scott, D.H. & K. L. Tanaka (1986), Geologic Map of the Western Equatorial Region of Mars, *US Geol. Surv. Misc. Invest. Series*, Map I-1802A.

Seelos, K D., R.E. Arvidson, M. Golombek, T. Parker, L. Tamppari & P. Smith (2006). Geomorphology and Terrain Characterization of the 2007 Phoenix Mission Landing Sites in the Northern Plains of Mars, in *37th Lun. Planet. Sci. Conf. Abs*. (CD-ROM), #2166, League City, Houston, Texas, USA.

Shean, D.E., J.W. Head & D.R. Marchant (2005). Origin and Evolution of a Cold-based Tropical Mountain Glacier on Mars: The Pavonis Mons Fan-shaped Deposit, *J. Geophys. Res*. 110, 5001.

Shean, D.E., J.W. Head, M. Kreslavsky, G. Neukum & the HRSC Co-Investigator Team (2006). When Were Glaciers Present in Tharsis? Constraining Age Estimates for the Tharsis Montes Fan-shaped Deposits, in *37th Lun. Planet. Sci. Conf*. (Ed. S. Mackwell and E. Stansbery), p.2092.

Simonelli, D., P. Thomas, B. Carcich & J. Veverka (1993). The Generation and use of Numerical Shape Models for Irregular Solar System Objects, *Icarus* **103**, 49–61.

Sinclair, P.C. (1969). General Characteristics of Dust Devils, *J. Appl. Meteorol.* **8**, 32-45.

Smith, D., G. Neumann, R.E. Arvidson, E.A. Guinness & S. Slavney (2003). *Mars Global Surveyor Laser Altimeter Mission Experiment Gridded Data Record,* Tech. Rep. MGS-MMOLA-5-MEGDR-L3-V1.0, NASA Planetary Data System.

Snow, J.T. & T.M. McClelland (1990). Dust Devils at White Sands Missile Range, New Mexico 1. Temporal and Spatial Distributions, *J. Geophys. Res.* **95**.

Squyres, S.W., A.H. Knoll, R.E. Arvidson, B.C. Clark, J.P. Grotzinger, B.L. Jolliff, S.M. McLennan, N. Tosca, J.F. Bell, W.M. Calvin, W.H. Farrand, T.D. Glotch, M.P. Golombek, K.E. Herkenhoff, J.R. Johnson, G. Klingelhöfer, H.Y. McSween & A.S. Yen (2006). Two Years at Meridiani Planum: Results from the *Opportunity* Rover, *Science* **313**, 1403–1407.

Stanzel, C., M. Pätzold, R. Greeley, E. Hauber & G. Neukum (2006). Dust Devils on Mars Observed by the High Resolution Stereo Camera, *Geophys. Res. Lett*. **33**, 11 202.

Thomas, P. (1993). Gravity, Tides, and Topography on Small Satellites and Asteroids: Application to Surface Features of the Martian Satellites, *Icarus* **105**, 326–344.

Toigo, A.D., M.I. Richardson, S.P. Ewald & P.J. Gierasch (2003). Numerical Simulation of Martian Dust Devils, *J. Geophys. Res.* **108**.

Torson, J. & K. Becker (1997). Isis – A Software Architecture for Processing Planetary Images, in *Lun. Planet. Sci. Conf. Abs.* **XXVIII**, pp.1443–1444.

Vago, J., B. Gardini, G. Kminek, P. Baglioni, G. Gianfiglio, A. Santovincenzo, S. Bayon & M. Van Winnendael (2006). ExoMars: Searching for Life on the Red Planet, in *ESA Bull.* **126,** 16–23.

Vasavada, A.R. & the MSL Science Team (2006). NASA's 2009 Mars Science Laboratory: An Update, in *37th Lun. Planet. Sci. Conf. Abs*., #1940 (CD-ROM), League City, Houston, Texas.

Werner, S.C. (2005). *Major Aspects of the Chronostratigraphy and Geologic Evolutionary History of Mars,* PhD thesis, Institute for Geosciences, Freie Universität Berlin.

Wewel, F., F. Scholten & K. Gwinner (2000). High Resolution Stereo Camera (HRSC) Multispectral 3D-Data Acquisition and Photogrammetric Data Processing, *Can. J. Rem. Sens.* **26**, 466–474.

Williams, D.A., R. Greeley, E. Hauber, K. Gwinner & G. Neukum (2005). Erosion by Flowing Martian Lava: New Insights for Hecates Tholus from Mars Express and MER data, *J. Geophys. Res. (Planets)* **110**, 5006.

Witbeck, N.E., K.L. Tanaka & D.H. Scott (1991). Geologic Map of the Valles Marineris Region of Mars, Map i-2010, Miscellaneous Investigation Series.

Wyatt, M.B. & H.Y. McSween (2002). Spectral Evidence for Weathered Basalt as an Alternative to Andesite in the Northern Lowlands of Mars, *Nature* **417**, 263–266.

Zegers, T., B. Foing, M. van Kan, R. Pischel, P. Martin, R. Jaumann, P. Pinet, A. Jehl, S. Werner, G. Neukum & the HRSC Co-Investigator Team (2005). Geological Mapping and Structural Analysis of Gusev Area: A Record of 4 Ga of Martian History, in *1st Mars Express Sci. Conf.*, ESTEC, the Netherlands.

Table 7. HRSC Co-investigators.

J. Albertz**, Technische Universität Berlin, Photogrammetry and Cartography, EB 9, Berlin, Germany
A.T. Basilevsky, Vernadsky Institute of Geochemistry and Analytical Chemistry, Russian Academy of Science, Moscow, Russia
G. Bellucci, Inst. di Fisica dello Spazio Interplanetario (CNR/IFSI), Rome, Italy
J.-P. Bibring, Centre National de la Recherche Scientifique (CNRS), Institut d'Astrophysique Spatiale (IAS), Orsay, France
M. Buchroithner**, Technische Universität Dresden, Institute of Cartography, Dresden, Germany
M.H. Carr, U.S. Geological Survey, Menlo Park, CA, USA
M.G. Chapman*, U.S. Geological Survey, Astrogeology, Flagstaff, USA
E. Dorrer**, Universität der Bundeswehr München, Institut für Photogrammetrie und Kartographie (IPK), Munich, Germany
T.C. Duxbury, Jet Propulsion Laboratory (JPL), California Institute of Technology, Pasadena, CA, USA
H. Ebner**, Technische Universität München (TUM), Photogrammetrie und Fernerkundung, München, Germany
B.H. Foing, Research and Scientific Support Department, ESTEC/SCI-SR, Noordwijk, the Netherlands
S. van Gasselt*, Freie Universität Berlin (FUB), Institute of Geosciences, Planetology and Remote Sensing, Berlin, Germany
R. Greeley, Arizona State University (ASU), School of Earth and Space Exploration (SESE), Tempe, AZ, USA
W.K. Hartmann*, Planetary Science Institute, Tucson, AZ, USA
E. Hauber, German Aerospace Center (DLR) Berlin, Institute of Planetary Research, Berlin, Germany
J.W. Head, III, Brown University, Department of Geological Sciences, Providence, RI, USA
C. Heipke, Universität Hannover, Institut für Photogrammetrie und GeoInformation (IPI), Hannover, Germany
H. Hiesinger, Universität Münster, Institut für Planetologie, Münster, Germany
H. Hoffmann, German Aerospace Center (DLR) Berlin, Institute of Planetary Research, Berlin, Germany
A. Inada, California Institute of Technology, Pasadena, CA, USA
W.-H. Ip, Institute of Astronomy, National Central University (NCU), Taiwan
B.A. Ivanov, Institute of Dynamics of Geospheres (IDG), Russian Academy of Science, Moscow, Russia
J. Jansa, Technische Universität Wien (TUW), Institut für Photogrammetrie und Fernerkundung (IPF), Vienna, Austria
R. Jaumann, German Aerospace Center (DLR) Berlin, Institute of Planetary Research, Berlin, Germany
H.U. Keller, Max Planck Institute for Solar System Research (MPS), Katlenburg-Lindau, Germany
R. Kirk, US Geological Survey (USGS), Astrogeology Program, Flagstaff, AZ, USA
P. Kronberg, Technische Universität Clausthal (TUC), Clausthal-Zellerfeld, Germany
R. Kuzmin, Vernadsky Institute of Geochemistry and Analytical Chemistry, Russian Academy of Science, Moscow, Russia
Y. Langevin, Centre National de la Recherche Scientifique (CNRS), Institut d'Astrophysique Spatiale (IAS), Orsay, France
K. Lumme**, University of Helsinki, Observatory and Astrophysics Laboratory, Helsinki, Finland
W. Markiewicz, Max Planck Institute for Solar System Research (MPS), Katlenburg-Lindau, Germany
P. Masson, Laboratoire Orsay Terre (FRE CNRS 2566), Université Paris-Sud Bâtiment 509, Orsay, France
H. Mayer**, Universität der Bundeswehr München, Institut für Photogrammetrie und Kartographie, Neubiberg, Germany
T.B. McCord, Bear Fight Center, Space Science Institute, Winthrop, WA, USA
J.-P. Muller, UCL Mullard Space Science Laboratory, MSSL, Space and Climate Physics, Dorking, Surrey, UK
J.B. Murray, The Open University, Department of Earth Sciences, Milton Keynes, UK
F.M. Neubauer**, Universität Köln, Institut für Geophysik und Meteorologie, Cologne, Germany
J. Oberst, Technical University of Berlin, Geodesy and Geoinformation Science, Planetary Geodesy, Berlin, Germany
G.G. Ori, International Research School of Planetary Sciences (IRSPS), Universita' d'Annunzio, Pescara, Italy
M. Pätzold, Universität Köln, Institut für Geophysik und Meteorologie, Cologne, Germany
P. Pinet, Laboratoire dynamique terrestre et planetaire de l'Observatoire de Midi-Pyrenees, Toulouse, France
R. Pischel, ESA Moscow, Moscow, Russia
F. Poulet, Centre National de la Recherche Scientifique (CNRS), Institut d'Astrophysique Spatiale (IAS), Orsay, France
J. Raitala, University of Oulu, Astronomy Space Institute, Oulu, Finland
G. Schwarz, German Aerospace Center (DLR) Oberpfaffenhofen, Institute of Remote Sensing Methods, Wessling, Germany
T. Spohn, German Aerospace Center (DLR) Berlin, Institute of Planetary Research, Berlin, Germany
S.W. Squyres, Cornell University, Department of Astronomy, Ithaca, NY, USA
U. Stilla**, Technische Universität München (TUM), Photogrammetrie und Fernerkundung, Munich, Germany

* Will have joined the team by 2009.

** Will leave the team by 2009.